CATALYTIC TUBULAR MICRO-JET

ENGINES

von der Fakultät für Naturwissenschaften der
Technischen Universität Chemnitz
genehmigte Dissertation zur Erlangung des akademischen Grades
doctor rerum naturalium
(Dr. rer. nat.)

vorgelegt von: Alexander A. Solovev, M.Sc.
geboren am 08.10.1981 in Maili-Sai, Kyrgyzstan

eingereicht am 29.03.2012

Gutachter:
Prof. Dr. Oliver G. Schmidt
Prof. Dr. H. Lang

Tag der Verteidigung: 26.06.2012

Bibliographic Record

Solovev, Alexander Alexandrovich

Catalytic Tubular Microjet Engines

Dissertation, Chemnitz University of Technology, Faculty of Natural Sciences (2012)

Abstract

This dissertation offers demonstrations of autonomous catalytic microtubes (microjet engines) with tunable diameters ranging from micro- to nanoscale and lengths from 50 μm to 1 mm. These results open the door to effective microengines and represent the entry in the Guinness Book of World Records for "the smallest man-made jet engine."

Several attractive methodologies of machine-based functions at the micro- and nanoscale are shown. For instance, catalytic Ti/Cr/Pt microjets, which are integrated on a planar substrate, can operate as "on chip" chemical micropumps by decomposition of hydrogen peroxide fuel into oxygen bubbles and water. When released from a substrate, microjets self-propel autonomously in solution. The incorporation of ferromagnetic layer (Fe) into the rolled-up geometry enables their remote control using external magnetic field. Such microjets were used to load, transport, deliver and assemble multiple cargo particles, including biological cells in bulk solutions and microfluidic channels. Furthermore, it is demonstrated that for microjets that are fixed to or self-propelled above a platinum-patterned surface, the microengine power/speed can be controlled using a white light-source. A change in intensity of the white light leads to a controllable switching "off" and "on" of the microengine power on demand. Light degrades a local concentration of the hydrogen peroxide fuel and surface tension and subsequently suppresses the generation of oxygen microbubbles.

In the next step, the diameter of the microjets was rigorously reduced to 250 nm by using hybrid heteroepitaxial/catalytic InGaAs/GaAs/Cr/Pt nanotubes. Due to asymmetry of the rolled-up layers, these nanojets move in corkscrew-like motions and act as "self-propelled nanotools," which were used in the next step to transport *yeast* cells and drill into fixed cancer *Hela* cells. Although it is well-known that hydrogen peroxide cannot be used to sustain viable cellular function, it is however conceivable that alternative fuels, such as glucose, might enable operation of such nanotools under biologically compatible conditions. As a first step to achieve this goal, demonstrations were made using metal-enzyme biocatalytic Ti/Au/SAM/Catalase microengines.

Synthetic components with competing interactions are well-suited to study the emergence of their collective behavior, such as swarms of large numbers of individuals. Microengines' self-organization in bistable swarms is shown at the air-liquid interface of the mixture of propylene carbonate and hydrogen peroxide. Microengines act as "water striders." Buoyed by oxygen bubbles, they self-propel via the microbubble recoiling mechanism and, depending on the bubbles' sizes, self-organize into swarms due to the meniscus-climbing effect. These reversible swarms depend on the microengine power, which competes against attracting surface tension force.

The demonstrated microjet engines show great promise for emerging applications, including biomedical, on-chip, environmental, and robotic micromachines. Furthermore, a key method discovered, entitled "rolled-up nanotechnology on polymers," allowed for the fabrication of highly parallel arrays of microtubes with multiple functionalities and aimed for different purposes.

Keywords: microjet engine, micromachine, catalyst, autonomous, remote control, microbubble, hydrogen peroxide, nanotechnology, self-organization.

Table of Contents

Introduction

The development of man-made synthetic micro- and nanomachines was foreseen by Richard Feynman in his 1959 talk entitled "There is Plenty of Room at the Bottom."[1] Currently, macroscopic man-made machines are well-developed – they can be fabricated using state-of-the-art materials science and engineering methods. Since the beginning of the 20th century, platinum metal has been used as a perfect catalyst for the catalytic decomposition of hydrogen peroxide into oxygen and water. It found many applications where high-powered engines were required, e.g. in first rockets, submarines, cars, and other powerful machines.[2] A jet engine is a reaction engine that discharges a fast-moving jet of fluid or gas to generate a thrust force via the jet-propulsion principle, consistent with Newton's laws of motion. Since the start of the era of machine miniaturization, it was found that for smaller engines, a viscous force causes the performance of microengines to drop off rapidly at engine diameters below a millimeter.[3] This situation is even more extreme if an engine is placed in a fluid and scaled down to microscale. In such a case, the Reynolds number, i.e. the non-dimensional number that measures the ratio of inertial to viscous forces, decreases several orders of magnitude. Thus, for a micromachine with a size of several micrometers, the viscous force dramatically increases and in most cases, inertia can be neglected.[4] On the other hand, notably biological micromotors solved the problem of high viscosity at very low Reynolds number. Interestingly, nanojet engines are used by some biological cells. For instance, bacteria *m.xanthus* sculptured biological nanonojet-like pores, where a hydration of extruded polyelectrolyte or "slime gel" drives cells over surfaces.[5, 6] However, the lifetime of bio-nanomotors is rigorously limited to biocompatible environments and they are difficult to adopt for technological applications *in vitro*.[7, 8]

Recent progress in the field of nanoengineering and the construction of artificial micro- and nanomachines led to demonstrations of synthetic catalytic nanomotors capable to self-propel in fuel solutions.[9] Particularly, recent attention has been concentrated on state-of-the-art bimetalic nanorod-based nanomotors driven by self-electrophoresis.[10] These nanomotors are capable of self-propelling up to 100 body length per second,[11, 12, 13] and can compete with the fastest bacteria driven by *flagellum*.[14] Although such impressive progress has been made, the power/efficiency of the latter system was found too low for desirable practical applications.[15, 16] In contrast, biological nanomotors not only convert chemical energy into motion, but they also perform useful work in supporting viable cellular functions,[17, 18] i.e. *kinesin* transport cargo within cells.[19] Up to now, it has remained a challenge to construct effective synthetic micro- or nanomachines that can accomplish tasks.

In this dissertation, demonstrations of effective tubular micro- and nanojet engines are given. Microjets operate using the catalytic decomposition of hydrogen peroxide fuel into oxygen microbubbles and water and overcome effectively high viscos-

ity levels of fluids at very low Reynolds numbers.[20] First, demonstrations of chemical micropumps based on microjet engines with diameter from 5 to 10 μm and tunable lengths in the range 20 – 1000 μm are given.[21] Previously magnetic remote control was used by nanorod based electrophoretic nanomotors,[22] however a low power limited their functions. After microtubes were release into the solution, magnetic remote control over microjets, which contained ferromagnetic (Fe) layer, was used for the transportation and direct assembly of cargo micro-objects,[23] as well as the capture and delivery of biological cells.[24] Additionally, a novel method to control the propulsion power of catalytic microjets was used by employing an external white light-source.[25] The rigorous reduction of the diameter of microjets to 250 nm was achieved by using hybrid catalytic/heteroepitaxial nanotubes. It allowed for finding new corkscrew-like motions, which were applied to a mechanized drilling of fixed cancer cells.[26] Swarming behavior of catalytic microjets, which was found to be similar to biological water striders, was reported at the air-liquid interface of the hydrogen peroxide fuel in organic solvent.[27] These demonstrations represent a solid platform to explore effective and collective micro- and nanojet engines for a variety of applications. Later Wang's group exploited other advantages of microjets, for instance, the group showed that microjets can detect DNA hybridization,[28] capture and remove cancer cells in complex media,[29] and isolate bacteria using lectin-modified microjets.[30]

A novel method of angular electron-beam deposition of inorganic thin films on patterned polymers, i.e. "rolled up nanotechnology on polymers", is introduced in this dissertation. The method helped to integrate highly parallel arrays of strained-engineered microtubes with multiple functionalities on planar substrates.[31, 32] In contrast, the fabrication of previously used hetero-epitaxial micro- and nanotubes often required chemically harsh solutions, e.g. hydrofluoric acid,[33] which rigorously limited a choice of functional materials. The described method (Chapter 2) helped to construct several prototypical devices, like magnetic micro-oscillators,[34] swiss-roll supercapacitors,[35] optical micro-resonators and metamaterials,[36] matrices for biological cells,[37] metallic waveguides to enhance atom-light interactions [38] – all of which were demonstrated in our group and collaborators.

Outline of the Dissertation

Chapter 1. Basic Principles

Basic principles of motion at the microscale are discussed. Examples of biological micro- and nanomotors are described and compared to the demonstrated microjet engine. An overview of the main principles of catalysis, materials, fuels, and different propulsion mechanisms of micro- and nanomotors and engines – powered by the decomposition of hydrogen peroxide or glucose – are given, with a particular emphasis

on the bubble-driven microjet. The chapter concludes with a discussion about the meniscus-climbing effect at the air-liquid interface, which is used to realize self-organized system of microjet engines.[27]

Chapter 2. Materials and Methods

A novel method of rolled-up nanotechnology on polymers is introduced to produce catalytic microtubes from stacked nanomembranes and integrate them on a planar substrate.[31] It is described how photolithography and the method of angular electron/thermal deposition of materials can be used to prepare catalytic microjet engines. Furthermore, in this chapter are described the protocols of materials choice, biochemical preparation methods, setup for the remote control of microengines using a magnetic field and light-sources, the fabrication of Poly-Di-Methyl-Siloxane (PDMS) microfluidics, and the effect of surfactants on the generation of microbubbles for several projects (shown in chapters 3–9).

Chapter 3. Chemical Pumps Based on the Micro-Jet Engines

A chemical pump has an advantage that it does not require any external source of power – it operates using the conversion of chemical energy into autonomous pumping of fluids.[39, 40] This chapter demonstrates how integrated Ti/Cr/Pt catalytic microengines with diameters ranging from 5 to 10 µm and tunable lengths from 20 to 1000 µm function as "on chip" catalytic micropumps.[21] Optimal parameters required for an efficient and unidirectional pumping of fluids are found for different lengths of micropumps and different concentrations of the hydrogen peroxide fuel. By using longer micropumps, a threshold concentration of the peroxide fuel can be reduced by 100 – 1000 times, i.e. as low as 0.009 % v/v H_2O_2 is sufficient to generate microbubbles and hence, start the pumping of fluids. This threshold concentration was found to be two orders of magnitude lower in comparison to the conventional micropumps driven by the decomposition of hydrogen peroxide.

Chapter 4. Autonomous Motion of Catalytic Micro-Jet Engines

Autonomous motion of catalytic microjet engines is demonstrated in the solution of hydrogen peroxide.[20] Here, the length of all self-propelled microjets was fixed to 50 µm. It allowed operating of microjet engines by unidirectional bubble-recoil in a wider range of hydrogen peroxide concentrations (discussed in chapter 3). The stepwise propulsion of microjets is caused by the recoil of bubbles from a larger tubular opening of microjets. It is shown that the velocity of a microjet can be approximated by the multiplication of the average bubble radius and the frequency of bubbles. Such deterministic speeds indicate the regime of a low Reynolds number, whereby the drift of a microengine due to inertia can be neglected. Trajectories in straight, circular and

three-dimensional helical motions are well-visualized via long microbubble tails generated by microjets.

Chapter 5. Autonomous Motion of Biocatalytic Micro-Jet Engines

Micromachines powered by biocompatible fuels, like glucose, are attractive for possible applications in medicine. As the first step to achieve this goal, a novel hybrid biocatalytic Ti/Au/SAM/Catalase microjet engine is shown. These microjets are based on a catalytic enzyme catalase, which is specifically bounded to SAM (Self Assembled Monolayer), i.e. immobilized in the inside wall of microtubes. This approach leads to more powerful microjets, which require a lower concentration of the peroxide fuel in comparison to Pt-based microengines.[41] Although it is well-known that the lifetime of an enzyme is limited in non-biological environments, these results show that it is possible to reduce the threshold concentration, and thus the toxicity of hydrogen peroxide fuel if hybrid biocatalytic microjets are used.

Chapter 6. Magnetic Control of Micro-Jet Engines and the Delivery of Cargo

Remotely controlled microengines are of interest when trying to conduct specific tasks using microjets. Particularly, such tasks consist of the transportation, delivery, and direct assembly of microcargo objects.[15, 23, 24, 29] State-of-the-art electrophoretic nanomotors either suffered from low power or an extra functionality (chemical, magnetic) of the cargo-motor system was required.[15] This chapter shows that by incorporating a ferromagnetic layer (Fe) into the catalytic microtubes, the directionality of Ti/Fe/Cr/Pt microengines can be controlled by an external magnetic field.[20, 23] Using the pumping mechanism, a facile method was demonstrated to load, transport, and deliver up to 65 polysterol microparticles. It is in contrast to the transport of one microparticle previously shown using electrophoretic nanomotors. Next, a high propulsion power of microjets was used for the direct assembly of thin metallic films, i.e. nanoplates, located at the air-liquid interface. Furthermore, it was shown that microjets can transport microparticles in microfluidic channels.[42]

Chapter 7. Light-Controlled Power of Micro-Jet Engines

Full control over the power of micromachines is crucial for real applications. In this chapter, a novel method for controlling the power of Ti/Cr/Pt microjet engines by means of a white light-source is described. A white light-source was used to control the generation of microbubbles and, hence, the propulsion of microjet engines.[25] The control was achieved through the degradation of hydrogen peroxide fuel, i.e., by locating a platinum-patterned silicon surface underneath self-propelled microengines. Influences of light-wavelength, light-intensity, degradation of surfactant, change of surface tension, and peroxide fuel concentrations are determined to control – and subsequently switch "off" and "on" – the propulsion of microengines.

Chapter 8. Self-Propelled Nanotools Based on the Nano-Jet Engine

Molecular Beam Epitaxy (MBE) was used to prepare hybrid catalytic/heteroepitaxial InGaAs/GaAs/(Cr)/Pt nanojet engines with diameters as small as 250 nm. This result represents the entry in the Guinness Book of World Records for the smallest man-made jet engine ever demonstrated. Nanojets have a tendency to form sharp tips due to asymmetrically rolled-up layers. A new corkscrew-like motion was found for nano-jets. Conceptual realization of "self-propelled nanotools," based on the nanojets that were able to move and drill into fixed cancer cells, was exploited.[26]

Chapter 9. Self-Organization of Micro-Jet Engines at the Air-Liquid Interface

The development of synthetic micromachines, which can act collectively based on principles of self-organization, pose a challenge.[43] Biological water striders adopt during the evolution of the meniscus-climbing effect at the liquid-air interface, they climb onto solid edges or self-organize into colonies. This chapter shows how Ti/Cr/Pt catalytic microjet engines with diameters from 5 to 10 μm – powered by the catalytic decomposition of hydrogen peroxide and buoyed by oxygen microbubbles – mimic the behavior of biological water striders.[27] Microengines self-propel and "sense" a liquid meniscus due to attracting lateral capillary force, change the directionality of their motion, and land on immersed objects at the air-liquid interface or on islands. Furthermore, when several microjets approach each other more closely than the capillary length, the menisci overlap and interact, and the micromachines attract each other. The balance between the microengines' attractive capillary and repulsion thrust forces determines their self-organization state, which is either swarming behavior or independent propulsion. The attracting force is determined by the liquid surface tension and the repulsion force is set by the driving power of microengines. A controllable and reversible self-organization of catalytic microengines was achieved.

Chapter 10. Outlook

What can be done next with catalytic microjets is considered in this chapter. One approach consists of the miniaturization and integration of other functional units with microjets. Several visionary ultimate goals where microengines can be potentially applied are described. For instance, can microjets be more effective and powerful? Can technology lead to smaller microjets? Can more complex "intelligent" micromachines be made from microjets?[32] Can microjets sense chemical gradients? Can microjets self-propel without microbubbles? Can microjets self-propel in environments other than fluid ones? Can microjets be useful in medicine?

1 Basic Principles

The motion of objects in a fluid are described to provide an understanding of the design of effective microjet (Chapters 2 – 7) and nanojet engines (Chapter 8). An overview of the importance of the Reynolds number, Brownian diffusion, the application of catalysis, and forces originating from catalytic reactions on surfaces of micromotors and engines are given. It is considered how the meniscus-climbing effect of microbubbles at the air-liquid interface can be used to explore self-organization of microjet engines (Chapter 9).

1.1 Challenges of Micro- and Nanoscale Machines

Biological micro- and nanomotors show high levels of sophistication and efficiency, while operating in highly viscous environments at a very low Reynolds number. Although bio-nanomotors are too complex to fabricate using current chemical or technological methods, they represent the working examples of functional nanomachines. Recently developed synthetic micro- and nanomotors and engines consist of homogeneous solid particles with no moving parts and have a simple spatial geometry, like micro-spheres, -rods, or -tubes containing catalytic layers or segments. It is discussed how different dimensions from micro- to nanoscale and shapes of micromotors, materials, fuel compositions and concentrations lead to different propulsion mechanisms of catalytic micromachines. Recent efforts have been concentrated on the understanding of these mechanisms divided mainly into self-electrophoresis, self-diffusiophoresis, recoil of microbubbles, and dynamic surface tension.

1.1.1. Motion at a Very Low Reynolds Number

The achievement of motion is crucial for survival of biological organisms on different scales. Different swimming objects in nature have different body sizes and thus they operate within a wide range of Reynolds numbers. Figure 1.1 shows maximum speeds of different swimming objects in nature in comparison to the maximum speed achieved by the microjet engine at room temperature. For instance, the blue whale, with its body length ~ 33.6 m, can achieve speeds up to 13 $m \cdot s^{-1}$ (0.4 $bl \cdot s^{-1}$); the fastest man can swim up to 2.4 $m \cdot s^{-1}$ (1.3 $bl \cdot s^{-1}$); 2 mm length copepod – 25 $mm \cdot s^{-1}$ (12.5 $bl \cdot s^{-1}$); 5 μm length *vibrio comma* – 400 $\mu m \cdot s^{-1}$ (200 $bl \cdot s^{-1}$).[44] If some object is stopped propelling forward in a fluid, the distance it coasts during deceleration is determined by the fluid Reynolds number. For instance, a blue whale uses the advantage of inertia, and even after it stops moving it continues drifting, i.e., "coasting," for a substantial period of time and distance. In contrast bacteria, due to the

small size and the regime of a very low Reynolds number, are almost immediately stopped by their environment.
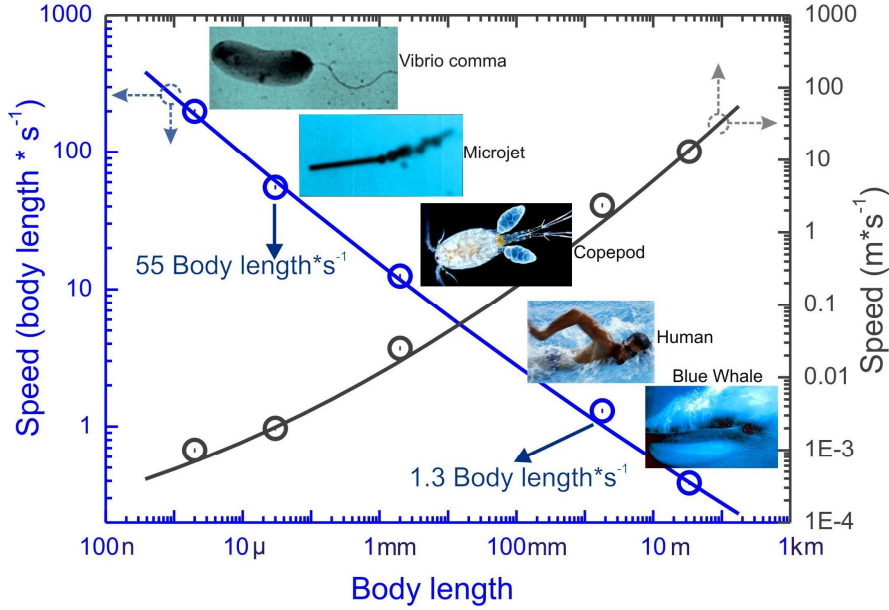
Figure 1.1: Relative and absolute speeds of natural swimming objects with different body lengths in comparison to the catalytic microjet engine developed throughout this dissertation. At room temperature, microjets move at speeds as high as 2100 μm s^{-1}.[20] The Reynolds number for a swimming man is on the order 10^{4}; for animals and objects in the micrometer scale, the Reynolds number is on the order of 10^{-1} to 10^{-5}.

The Reynolds number determines the ratio of inertial and viscous forces acting upon the body [4]

$$\mathrm{Re} = \frac{vL\rho}{\eta} \tag{1.1}$$

where v is the velocity of the body, L the characteristic size of the body, η the dynamic fluid viscosity, ρ the fluid density.[4] The regime of Reynolds numbers (*Re*) below 2100 is known as the regime of low Reynolds numbers.[45, 46, 47] According to Purcell [4] the coasting distance of an object can be well approximated by the following relation $d = L \cdot \mathrm{Re}$. For instance, if bacterium with a size of 50 μm moves at speed 200 μm s^{-1} in water, *Re* is on the order of 10^{-3}. Thus, the coasting distance is around 50 nm. Consequently, for the non-stoppable movement of an object, a motive force must be continuously generated.

Microjet engines with a body length of 50 μm and diameters ranging from 5 to 10 μm can reach speeds above 2 mm·s^{-1} (55 bl·s^{-1}) at room temperature.[20] Recently, in our group there was report of a dramatic acceleration of microjets up to 10 mm·s^{-1} (200 bl·s^{-1}) at physiological temperature.[48] Wang's group reported acceler-

ations of microjets above 375 bl·s^{-1}.[49] These kinematic characteristics make micro-jet engines the fastest in absolute speed of any bacteria known and the fastest autonomous microengines of all synthetic micromotors known to date.

1.1.2. Biological Micro- Nanomotors and Engines

Biological motors operate both within cells and self-propelling cells by converting chemical-free energy, such as energy released by the hydrolysis of Adenosine-5'-TriPhosphate (ATP).[50] Several examples of biological micromotors are exhibited in Fig. 1.2 and compared to the demonstrated microjet engine.
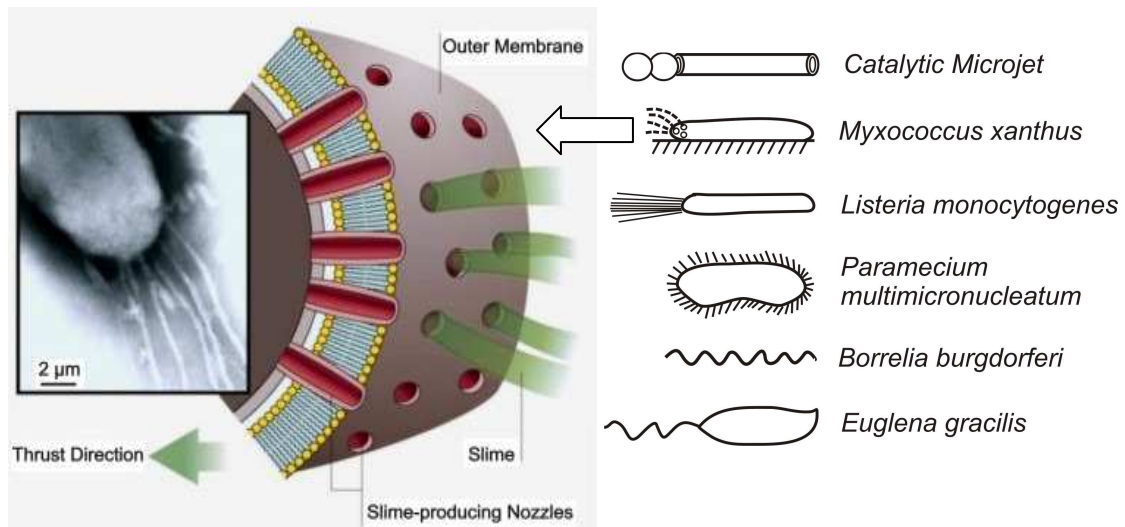
Figure 1.2: Right-hand sketch shows schematic of different mobile biological cells and the microjet engine. Left-hand sketch shows schematic and SEM image (inset) of biological nanojet-propelled bacteria *m.xanthus*. Left-hand sketch was copied from Wolgemuth and Oster.[51]

Figure 1.2 shows that some mobile cells use the analogy of a "nanorocket" engine driven by an assembly and elongation of actin filaments, e.g. *listeria monocytogenes*. Some cells use the analogy of a "nanojet" engine driven by a hydration of polyelectrolyte, e.g. *myxococcus xanthus*. Other cells use the analogy of an "electric nanomotor" driven by a transfer of protons/ions to induce rotation of *flagellum,* e.g. *euglena gracilis*; "multiple micromotors" driven by oscillations of multiple cilia, e.g. *paramecium multimicronucleatum*; stepwise translation of helical body, e.g. *borrelia burgdorferi*.

Biological micro- nanomotors and engines

"Nanorocket": *actin* is a protein unit of cells with multiple functions. Particularly, it is used for the cellular motility. *Actin* self-assembles into filaments, leading to cell

protrusion via "comet tails."[52] Some intracellular pathogens, such as *listeria monocytogenes, shigella flexnery, rickettsia rickettsii,* and *vaccinia* viruses, move through the polymerization of cell host *actin*.[53 , 54] *Listeria* move at a relatively low speed of 0.072 μm·s^{-1}. However, the power of nanomotors is sufficient to overcome a distance of a single biological cell and subsequently to infect neighboring cells.[55] Besides, pathogens self-propel "at no cost" because they use the cells host *actin* as a fuel.

"Nanojet": *polyelectrolyte hydration* is a secretion of slime that provides a sufficient force to push some bacteria, like *m.xanthus*. This bacteria uses an advantage of the Junction Pore Complex (JPC), known as "nanojet engines," to glide over surfaces.[51, 56] The secretion of cationic polyelectrolyte in around 200 pores with 20 nm the diameter of an individual pore creates a thrust force that drives bacteria at speeds of up to 3 μm·s^{-1}. Similarly, nanojets use *cyanobacteria, flexibacteria,* and *myxobacteria*. The demonstrated synthetic nanojet, developed throughout this dissertation, consists of only one nanotube. The diameter of the tube is 12 times larger in comparison to one individual pore of *m.xanthus*. However, the maximum speed of the demonstrated nanojet is 40 times higher than that of the *m.xanthus*.

"Nanomotor": *flagellum* is a tail-like filament that protrudes from the cell body of certain prokaryotic and eukaryotic cells and one of the most powerful biological nanomotors.[57] The bacterial flagellum is driven by a rotary engine made up of proteins, located at the flagellum's anchor point on the inner membrane.[58] This nanomotor is powered by the proton (some nanomotors use sodium) motive force, i.e. through the flow of protons across the cellular membrane due to a concentration gradient.[59] The rotor transports protons across the membrane and during an operation it increases up to 17,000 rpm, but a nanomotor with the flagella filament can reach up to 1000 rpm. Cells with a flagella motor can reach a speed of several hundred micrometers per second. Some cells transform their bodies into a helical shape and move through the linear translation of their helixes, e.g. *b.burgdorferi* moving at a speed of up to 5 μm·s^{-1}.[60]

"Multiple nanomotors": *Cilium* is a motile multi-motor organelle in eukaryotic cells that is used by some microorganisms for motion.[61] Several thousand dynamic cilia filaments are located on the cellular wall and usually beat in a coordinated fashion. Ciliates, like *paramecium,* self-propel faster than flagellates because of multiple *cilia* motors located on each cell. The maximum speed reached by *paramecium* is 2 mm·s^{-1}.[62]

"Molecular motors and nanomachines": Motor proteins are related to a class of molecular motors that move along surfaces to accomplish different tasks. For instance, motor proteins can transport vesicles in the cytoplasm.[63, 64, 65] Muscle protein *myosin* is responsible for decreasing the size of muscles. *Kinesins* and *dyneins* are a group of motor proteins that play major roles in intracellular transport.[66] *Dyneins* are microtubule motors capable of sliding, helping in the

movement of cilia and flagella.[19] Nucleic acids nanomotors include RNA *polymerase,* which transcribes RNA from a DNA template. DNA *polymerase* turns single-stranded DNA into double-stranded DNA.[67, 68] *Helicases* separate double strands of nucleic acids. *Topoisomerases* regulate winding of DNA. Viral DNA packaging motors inject viral genomic DNA into capsids as part of their replication cycle, packing it tightly.[69]

1.1.3. Micro-objects and Brownian Diffusion

Micro- and nano-objects immersed in a fluid move erratically due to their collisions with molecules in fluid. Nature in many cases utilizes Brownian diffusion for microsystems rather than competing against it. For instance, reaction-diffusion processes are involved in the sculpture of protein assemblies.[70] On the other hand, biological molecular motors, considered in previous paragraph, solved the diffusion problem by operating at the interfaces. It is challenging to construct synthetic micro- or nanomachines that can overcome Brownian diffusion.

The theory of Brownian diffusion was developed by Langevin, Smoluchowski, and Einstein, who showed that Brownian motion is a consequence of scale and not the nature of an environment.[71, 72] Hence, if the diffusion is known, it is possible to determine the squared value of the displacement of an object $\left\langle x^2 \right\rangle = 2Dt$, where t is the time and D is the diffusion coefficient. In essence, an object undergoes Brownian motion with the kinetic energy that corresponds to the surrounding temperature. Einstein described the theoretical analysis, relating the molecular motion to the macroscopic measurement of diffusion, defined by the diffusion coefficient. It relates the diffusion of the particle to the friction coefficient using

$$D = \frac{kT}{f} = \frac{kT}{6\pi\eta r} \tag{1.2}$$

where k is the Boltzmann constant, T is temperature, η is fluid viscosity. Here f is Stokes's friction for a spherical particle. A spherical particle with a radius of 1 μm suspended in water has a diffusion coefficient 0.24 $\mu m^2 \cdot s^{-1}$.[45] Hence, colloidal particles can utilize Brownian motion to move with a mean kinetic energy proportional to the surrounding temperature $3kT/2$. However, this non-direct movement is effective only in small volumes; at larger volumes or longer distances, transport by diffusion takes a substantial period of time. A condition of bacteria to overcome diffusion was considered by Purcell.[4] A typical hydrodynamic transport time, i.e. the time to transport anything by distance l through advection, is about distance divided by an object speed [45]

$$\tau_a \sim \frac{l}{v} \sim l^0 \qquad\qquad (1.3)$$

where l is the characteristic length scale and v is a typical speed. Whereas, the time to transport via diffusion is represented by

$$\tau_d \sim \frac{l^2}{D} \sim l^2 \qquad\qquad (1.4)$$

The ratio between τ_a and τ_d measures the Peclet number

$$Pe = \frac{v\,l}{D} \qquad\qquad (1.5)$$

This equation shows the effectiveness of advection versus diffusion for any given distance and diffusion constant. The Peclet number measures the relative importance of advection with respect to diffusion.[77] The transport for the situation when the Peclet number is below one is primarily controlled by the diffusion. Subsequently, Purcell estimated that to overcome Brownian motion and achieve the direct motion, bacteria such as *e-coli*, must overcome a certain distance.[4] It can be found from the following relation $l \geq D/v$. Similarly, to achieve straight motion, a micromachine that has the size of a bacterium and moving at the speed $v = 30\ \mu m \cdot s^{-1}$ must overcome a minimum distance of $l \geq 30\ \mu m$.

1.2 Synthetic Micro- Nanomotors and Engines

In recent years a large amount of catalytic particles have been engineered for application as micromotors and engines.[15, 17, 28, 29, 31, 32, 43, 73, 74] These particles contain heterogeneous catalysts, and once immersed in a fuel solution they start self-propelling due to the catalytic conversion of fuels. Principles of heterogeneous catalysis are considered. Different propulsion mechanisms of catalytic micromachines are described.

1.2.1. Heterogeneous Catalysis for Microengines

Heterogeneous catalysis is of great importance in many industries and it represents a strategy exploited in recent years for the design of synthetic micro- and nanomachines. Catalysis is the process in which the rate of a chemical reaction is either increased or decreased by means of a chemical substance known as a catalyst.[75] Catalysts are not consumed during the reaction itself, and thus such materials are suited very well for the design of synthetic nanomachines. In heterogeneous catalysis, a catalyst phase is different from the reactant, particularly this phase is a solid

state.[75] Although many reactions can be potentially applied to power microm-achines, recent research has been concentrated on the catalytic decomposition of hy-drogen peroxide in the presence of platinum catalysts into oxygen and water, i.e., 2 $H_2O_2 \rightarrow 2\ H_2O + O_2$.[9, 20, 76, 77, 78]. One reason for this materials choice – plati-num catalyst can work without degrading for substantial periods of time. The other reason consists of the environmentally clean fuel products of microengines, which are oxygen and water.
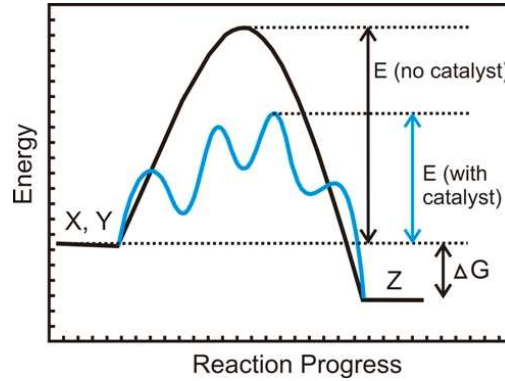
Figure 1.3: Potential energy diagram, reproduced from ref.[75], showing the effect of a catalyst in an exothermic chemical reaction *X* + *Y* to give *Z*. The presence of the catalyst opens a different reaction pathway with lower activation energy.[79] Here, *E* is activation energy with and without catalyst; Δ*G* is enthalpy change.

Many reactions can be blocked or slowed due to the existence of kinetic energy barriers and catalysts enable such reactions to occur.[75] Catalysts form a transition state of lower free energy and even small decreases in the potential energy barrier can increase the reaction rate significantly. The process of hydrogen peroxide de-composition is spontaneous and exothermic and depends mainly on temperature, concentration of molecules, pH, and impurities. The decomposition of hydrogen per-oxide results in an overall process of energy release for H_2O_2. Details of energy dia-gram of hydrogen peroxide and its application as an energy source are discussed in ref. [79].

1.2.2. Propulsion Mechanisms

Different mechanisms of propulsion are observed for synthetic catalytic micro- na-nomotors and engines powered by the decomposition of hydrogen peroxide or glu-cose fuels. By better understanding different forces acting on the micromachines, a powerful and energy-efficient mechanisms of motion can be designed. Different pro-pulsion mechanisms originated mainly from microbubbles, self-electrophoresis, self-diffusiophoresis, and interfacial tension are described.

1.2.3. Micro-Jet driven by Bubbles

Whitesides' group pioneered with the movement of millimeter-scale boats powered by oxygen bubbles. These boats contained catalytic Pt segments and were powered by the catalytic decomposition of hydrogen peroxide, Table 1.1(a).[80] The advantage of bubble-propelled micromachines consists in their high power and ability to operate in salt-rich environments, in which state-of-the-art catalytic electrophoretic nanomotors fail to work.[81] Groups of Ozin, Sen, and Mallouk discovered independently the propulsion of bimetallic catalytic nanorod-based nanomotors, which self-propelled in solutions of hydrogen peroxide. Ozin's group added surfactant to the solution of Ni/Au nanomotors and observed the movement of nanomotors by bubbles.[12] Sen's and Mallouk's groups did not use surfactant and found that mainly electrophoretic mechanisms were responsible for the movement of similar Pt/Au nanomotors, self-propelled with the Pt end forward (where the generation of O_2 bubbles was not reported), Table 1.1(i). Other examples of propulsion by microbubbles include Pt/SiO$_2$, Table 1.1 (j) [82] and a surface-bound Mn catalyst on SiO_2 particles, Table 1.1 (g).[83] Since insulator/catalyst materials were used for these micromotors, the electrophoretic mechanism of motion can be excluded. To date, maximum reported speed of bubble-driven autonomous micro- and nanomachines was in two orders of magnitude lower than that of the microjet engines.

Figure 1.4 shows a model of the microjet engine driven by the thrust of bubbles. Experimentally, it was determined that microbubbles migrate mainly towards a larger tubular opening. It is important to not that the conical shape is a result of asymmetric rolling of layers and it was not designed by fabrication. Although, in some cases one cannot distinguish a clear conical shape we believe that the difference in diameters of openings is at the micro- to nanoscale.

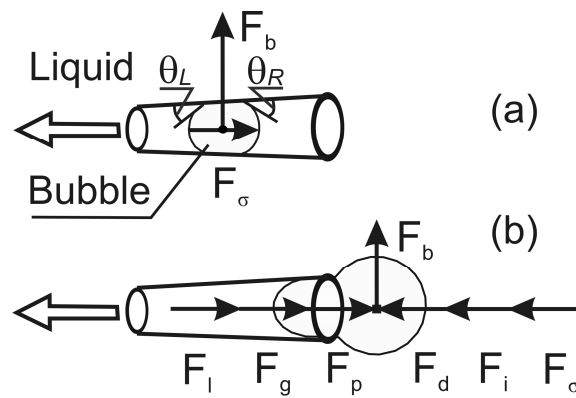Figure 1.4: Forces acting on a microbubble-driven microjet engine. Empty arrows indicate the direction of microjet motion due to the bubble-induced pumping of fluid and the bubble recoil. (a) Microbubble migrates towards larger tubular opening. (b) Forces acting on the microbubble at the moment when it leaves the microjet. The weight of the microjet located in a fluid and the skin-drag forces experienced by microjets are neglected.

Motion of microjets can be divided into two steps. Firstly, the microjet moves during the migration of bubbles in the tube, shown in Fig. 1.4 (a). Secondly, the microjet moves during the recoil of bubbles, Fig. 1.4 (b). Bubble migration, Fig. 1.4 (a) can be understood in the following way. The bubble has different boundary contact angles between the liquid and the solid wall (Θ_L, Θ_R) due to the conical shape of the microjet. It causes differential pressure, which can be described by the following formula

$$\Delta P_c = P_R - P_L = 2\left[\left(\frac{\sigma \cos\Theta}{d_t}\right)_R - \left(\frac{\sigma \cos\Theta}{d_t}\right)_L\right] \tag{1.6}$$

where d_t is the microtube diameter, σ is the surface tension. The surface tension differential force can be written as $\Delta F_\sigma = \pi\sigma(d_{tR}\cos\Theta_R - d_{tL}\cos\Theta_L)$. In the case of $\Theta_R > \Theta_L$ the bubble migrates from left to right. The bubble reaches the end of the tube and recoils.

According to Snabre and Magnifotcham,[84] one can write down forces acting on the bubble, which leaves the capillary immersed in a fluid in the following way $F_l + F_g + F_p = F_d + F_i + F_\sigma$, where inertial force ($F_i$), gas momentum force ($F_g$), liquid momentum force (F_l), pressure force (F_p), drag force (F_d), surface tension force (F_σ), buoyancy force (F_b). It is described [84] that the gas momentum force equals $F_g = \pi r_j^2 \rho_g \upsilon_g^2$, liquid momentum force $F_l = \pi r_j^2 \rho_l \upsilon_l^2$, pressure force $F_p = \pi r^2 (P_g - P)$, buoyancy force $F_b = (\rho - \rho_g)gV$, inertial force $F_i = (\alpha + \rho_g/\rho_l)\rho V\gamma$, and Stokes drag force

$$F_d = 6\pi\eta r \upsilon_b \tag{1.7}$$

in these relations, r_j is the bubble radius, ρ_g the gas density, υ_g the gas velocity (velocity of gas flow rate, not the migration speed of the bubble), ρ_l the liquid density, υ_l the liquid velocity in the microjet, P_g the gas pressure, P the surrounding pressure in the liquid, g the gravity acceleration, V the bubble volume, and γ the average bubble acceleration. Inertial term (F_i) can be neglected for the regime of very low Reynolds number (Re << 1). Buoyancy is acting in a vertical direction and in some cases the weight of micromachines can be neglected. Microjets, buoyed by bubbles, can self-propel at the air-liquid interface (see Chapter 9).

Gibbs and Zhao developed a model of a bubble-drivel micromotor and discussed the results of self-propelled Pt/SiO₂ microparticles. They showed that at the moment of microbubble detachment, a momentum change creates a net driving force.[82] Interestingly, the microjets developed throughout this dissertation, can reach speeds of 350 times higher than the bubble-driven spherical micromotor of Gibbs and Zhao. It is of interest to estimate whether the momentum force in case of microjets is significant. From the experimental data, microbubble migration speed in

microjets is estimated roughly 2 mm·s^{-1}. One can calculate that for a microjet with a radius of 5 μm, the liquid momentum force is on the order of 10^{-13} N. Note that the speed of microbubble recoil (accepted by Gibbs) can be higher than the speed of the migrating microbubble through the microtube. The Stokes drag force experienced by bubbles is on the order of 10^{-10} N. Subsequently, the liquid momentum force is 10^3 times lower than that of the drag force. Because bubbles have contact with the microjet opening during their recoil, the speed of the microjet can be well estimated from the Stokes drag force experienced by bubbles, i.e., the speed is a product of bubbles size and frequency (see also Chapter 4). Interestingly, since the bubble migrates it pumps fluid in and out of the tube. If microjet would be driven only via liquid momentum force this could lead to stationary or oscillatory motions of microjets. The volume of a fluid that comes out of the tube is equal to the volume of fluid that comes in the tube (personal discussion with Prof. V. Fomin, IFW Dresden). One can think of an analogy to a macroscale "bottle water rockets" which can fly by the momentum transfer of the expelling liquid from the bottle. Such macro-rockets could not fly in case if the same amount of water (which comes out) would come into the mouth of the rocket, because this would balance the momentum force. The situation with microjets is different, here the value of the momentum force is in two orders of magnitude lower (at the bubble speed of 2 mm s^{-1}) than the drag force which experiences by microbubbles. This drag force acts only in one direction, that is opposite to the direction of moving bubble. Subsequently, this force drives the microjet. It can explain a high propulsion power of microjet engines. A detail model describing speeds of microjets is the subject of current research in our group.

1.2.4. Other Propulsion Mechanisms

Self-electrophoresis, self-diffusiophoresis and dynamic interfacial tension are accepted mechanisms of motion, which can be used to self-propel catalytic micro- nanomotors and engines. Table 1.1 (b, e, f, i, j) shows several non-bubbling propulsion mechanisms.[98]

Self-electrophoresis

Self-electrophoresis is the movement based on the electro-osmotic flow on the surface of a particle with a self-induced electric field. Self-electrophoretic nanomotors were described by Sen's and Mallouk's group.[85, 86, 87, 88] Bimetallic nanomotors with diameters of 370 nm and optimized length of 2 μm were self-propelled in a solution of hydrogen peroxide. A self-induced electric field occurs as a result of an oxidation-reduction reaction. Table 1.1 (i) illustrates examples of electrophoretic nanomotors consisting of Au/Pt mobile nanorods. In details, hydrogen peroxide is oxidized to oxygen and on the Pt segment, electrons are withdrawn from the hydrogen

peroxide to the nanomotor.[89] On the Au segment, the hydrogen peroxide is reduced to water. Subsequently, during the transfer of electrons in a bimetallic junction, the hydrated protons and H_3O^+ ions move along the surface of nanomotor.[89] These ions create an electro-osmotic flow, which drives electrophoretic nanomotors. Nanomotors are self-propelled with the platinum end forward. This mechanism was well-described by Paxton [85, 90] and Pumera.[89] Wang's group designed faster nanomotors by changing the conductivity of nanorods (or increasing the nanorods' surface areas), such as modification of Pt segment with carbon nanotubes (CNT)-Pt/Au as a dopant. It led to speeds as high as 200 $\mu m \cdot s^{-1}$ upon an addition of hydrazine to the fuel solution,[91] and up to 150 $\mu m \cdot s^{-1}$ for catalytic alloy Ag-Pt/Au nanomotors.[92] These speeds are comparable to nanojet engines being moved by bubbles, demonstrated in Chapter 8.

Dynamic Surface Tension

Some motors can move by the dynamic surface or interfacial tension force. One classic example is millimeter-scale object filled with camphor molecules, i.e., a "solid fuel", which decreases a surface tension of water. Camphor dissolves, and as a result such motors can reach speeds as high as tens of $cm \cdot s^{-1}$. Previously, it was considered that surface tension can play a role in the motion of electrophoretic nanomotors.[93, 94, 95] Table 1.1 (f) shows one example of autonomous microgear driven by interfacial tension force. However, since the microgear consisted of bimetallic parts, it is likely that an electrophoretic mechanism contributed significantly to the motion. A direct motion of catalytic motors which have micro- or nanoscale dimensions and are driven only through surface tension force has not been reported. In our group we tried to demonstrate the non-catalytic camphor based microjets engines. However, the difficulty consists in the immidiate consumption of the "solid fuel" contained in the tubular microjets.

Self-Diffusiophoresis

Gradients of soluble or non-gaseous reaction products are known to create motion of colloidal particles in solutions. Golestanian's group reported about self-diffusiophoresis of non-conducting colloidal polysterol particles coated with platinum.[96, 97] During the process of diffusiophoresis, the speed and the direction of motion depend on the interaction between the particle surface and the solute, as well as on the magnitude of the solute gradient. This effect would occur when a particle with a catalyst on one side creates an asymmetric distribution of reaction products around the particle. It generates a motive force for the motor particle. One example of micromotors moving by self-diffusiophoresis is shown in Table 1.1 (j: case b), at speeds up to 6 $\mu m \cdot s^{-1}$. Although this mechanism is interesting to consider, the power of self-diffusiophoretic micromotors was found too low for practical application.
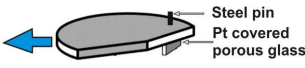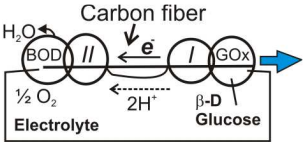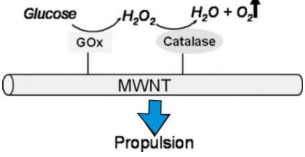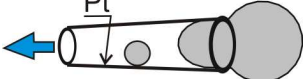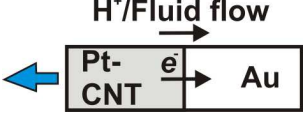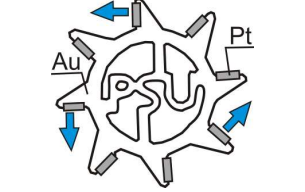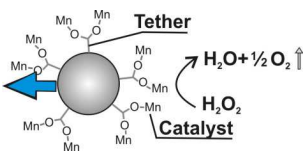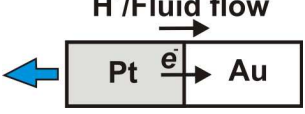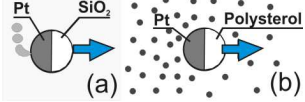
Schematic	Speed	Size	Fuel	Mechanism	Catalyst
Steel pin / Pt covered porous glass	2 cm/s (a)	L = 1 cm	H_2O_2	Bubble recoil	Pt
Carbon fiber (BOD, GOx, H_2O, $\frac{1}{2}O_2$, $2H^+$, β-D Glucose, Electrolyte)	1 cm/s (b)	D = 7 μm L= 0.5–1 cm	Glucose	Self electro-phoresis	Glucose oxidase and Bilirubin oxidase
Glucose, H_2O_2, $H_2O + O_2$, GOx, Catalase, MWNT, Propulsion	2-8 mm/s (c)	L=0.5– 5 μm D=20–80 nm	Glucose	Bubble recoil	Glucose oxidase and catalase
Pt	2.1 mm/s (d)	L=20–100 μm; D=0.3–5 μm	H_2O_2	Bubble recoil, Fluid pumping	Pt /Catalase
H^+/Fluid flow, Pt-CNT, e^-, Au	200 μm/s (e)	L = 2 μm D=220 nm	H_2O_2/ N_2H_4	Self electro-phoresis	Pt-CNT(cathodic reaction at Au)
Au, Pt	18.8 rad/s (f)	D = 300 μm	H_2O_2	Interfacial tension, electrophoresis	Pt
Mn Tether, $H_2O+\frac{1}{2}O_2$, H_2O_2, Catalyst	35 μm/s (g)	D=40-80 μm	H_2O_2	Dynamic interfacial tension	Synthetic catalase
H^+/Fluid flow, Pt, e^-, Au	6.6 μm/s (i)	L = 2 μm D=370 nm	H_2O_2	Self-electro-phoresis	Pt(cathodic reaction at Au)
Pt, SiO_2, Pt, Polysterol (a) (b)	3 μm/s 6 μm/s (j)	a) D= 2 μm b) D=1.6μm	a) H_2O_2 b) H_2O_2	a) Bubble recoil b) Self-diffusiophoresis	a) Pt b) Pt

Table 1.1: Several illustrative examples of state-of-the-art catalytic micro- nanomotors and engines. Table is modified according to ref. [98], here the microjet engine is included. These chemical micro- and nanomachines are powered by the catalytic decomposition of hydrogen peroxide or glucose fuels. Although similar fuels and materials are used, the propulsion mechanism can be different due to different shapes of particles, concentration and composition of fuel molecules leading to the interplay between the reaction and diffusion processes. In some cases, microbubbles can be generated and supply a motive force for the micromachine.

1.3 Self-Organization through the Meniscus-Climbing Effect

Exploring Self-Organization (SO) of autonomous objects can help to better understand biosystems and to design materials and devices with emerging properties.[80, 99, 100, 101, 102] For instance, recently one approach has been reported towards the development of more complex micromachines by taking multiconstituent nanomotors.[43] In a contrast to static self-assembly, which represents a kind of "crystallized" particles, SO systems form time-reversible structures and depend on the supply of energy.[103, 104] One interesting observation in nature is the meniscus-climbing effect, which was adopted by biological water striders to reach solid edges and self-organize into colonies.[105] Similarly, the meniscus-climbing effect induces static self-assembly of bubbles located at the air-liquid interface. However, bubbles form static structures due to existence of lateral capillary force. To date, it was not known how to induce SO of synthetic micromachines through bubbles. Experimental results of this finding are discussed in chapter 9.[27] In this case, microjets not only attract each other by bubbles, but they repel using motive forces. This interplay has a characteristic length at the micrometer to millimeter scale,[106] and it is used to demonstrate SO of microjet engines.

Qualitatively, the meniscus-climbing effect can be understood by considering surface tension and the environment of molecules in a fluid. It is well-described by Pelesko [107] that, for a situation where a molecule is located in the interior of a fluid, forces are equal from its neighboring molecules in all directions. However, if a molecule is located at the surface of a liquid, it experiences less force from the air than it does from the fluid. Consequently, molecules near the surface experience a net force that pulls them back into the bulk. As a result, when liquid meniscus form, it causes lateral capillary forces to appear. Similar, when the liquid wets a physical object, it distorts the planar liquid surface and attracting meniscus is formed. It is known as the meniscus-climbing effect. On the other hand, if meniscus is negative, it can cause repulsion.

Biological water striders are able to walk on the surface of water and use meniscus climbing effect to climb on islands or edges. Fig. 1.5 A shows a water strider that is attracted to the solid edge through the meniscus-climbing effect (note: strider put front leg in a static mode to create positive liquid meniscus). Fig. 1.5 B shows schematic of bubbles attracted to edge and to each other B (i-ii). Bubbles rise to the surface of fluid because they are buoyant due to their lower density. Even when bubbles are constrained at the liquid surface, the upward buoyancy force is still acting and bubbles can move only along the meniscus, Fig. 1.5 B. As a consequence, if two or more bubbles are close to each other, they clump together. Notably, for the bubble-bubble system, meniscus between the bubbles is usually curved upwards. When the bubbles move toward one another, they move down the menisci overall and reduce the gravitational energy in such a system.[107]
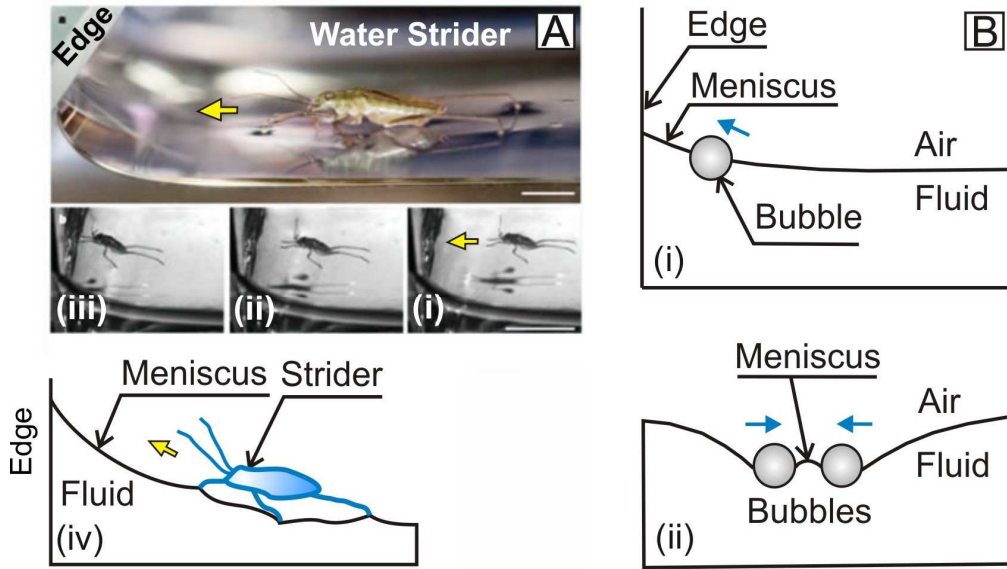
Figure 1.5: Meniscus-climbing effect observed in animate biological and inanimate synthetic systems. (A) Water-walking strider (i-iii), which approaches edge (copied from ref. [105]), and its schematic (iv). It is accepted that water wets solid walls. (B) Schematic of a bubble located at the air-liquid interface (i) and bubbles located nearby and attracted each other (ii). Blue arrows show the direction of moving bubbles caused by the meniscus-climbing effect, according to Pelesko.[107]

Fig. 1.6 A–C shows schematic of moving microjets with competing attracting and repulsing interactions at the air-liquid interface. Microjets are indicated schematically by empty arrows. It follows that interplay between the size of the bubble and the microjet power/speed is crucial for SO to occur (this discussion provides understanding of results concerning meniscus-climbing microjets and their self-organization, reported in Chapter 9). The capillary length can be defined as $\lambda_c = \sqrt{\gamma / \rho g}$, where g is the acceleration due to gravity, ρ is the density of the fluid, and γ is the surface tension of the fluid-fluid interface.[105] For hydrogen peroxide one can estimate $\lambda_c \approx 2.7\ mm$.
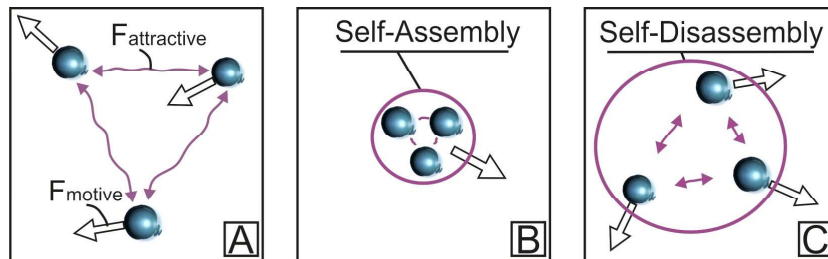
Figure 1.6: Principles of self-organization require time-reversible assembly of objects to occur. SO system can be engineered by considering competing interactions between objects (suppose here that a motive force is defined by the power of bubble-driven microjets). (A) Independent motion of objects, (B) self-organization of objects, (C) objects return to their independent motion.

Grzybowski described that in the case of the radii of the objects at the air-liquid interface, R, and the distance between objects, L, are smaller than the capillary length; the capillary force can be simplified to the following relation $F_{attractive} \propto \gamma R^2 / L$.[99] The capillary force competes against the motive force and SO occurs if these forces are balanced. Thus, the condition $F_{attractive} \approx F_{motive}$ sets the desired length scale at which the SO system must operate. Accepting that the speed v_j and the motive force F_{motive} of microjets can be approximated by the Stokes drag force experienced by spheres/bubbles $F_{motive} = 6\pi \mu R v_j$. It follows from the above condition that the radii of the spheres and the characteristic distance, L, between them should obey the relation $6\pi \mu R v_j \propto \gamma R^2 / L$. From here it is possible to determine the characteristic length scale $L = \gamma R / 6\pi \mu v_j$. Taking values for hydrogen peroxide ($\gamma = 74\ mN/m$, $\mu = 1.245\ cP$), accepting object radius for calculation 20 µm and its speed 100 µm·s^{-1}, the characteristic length is around 650 µm. More powerful micromachines require shorter distances for their interactions to overlap and thus for SO. On the other hand, once a size of generated bubbles decreases, the capillary force drops down and colonies of micromachines decay.

2 Materials and Methods

In the following pages, a novel, versatile method of multifunctional microtube fabrication on sacrificial polymer layers, which helped to integrate microtubes on a planar substrate, is described. This key method allowed a highly parallel and large production of catalytic microjet engines on planar surfaces. The setup for the control of microengines using a magnetic field and light-sources and the fabrication of microfluidic channels for microengines is described. Theory and experimental data of microbubble nucleation in a solution of hydrogen peroxide and the effect of the surfactant on microbubble size are considered to optimize working conditions for the catalytic microjets.

2.1 New Method – Rolled-up Microtubes on Polymers

Scheme 2.1 shows a new method entitled "rolled-up nanotechnology on polymers". Thin metallic films rolled-up into compact multimetallic microtubes by under-etching the sacrificial polymer (photoresist) layer. Depending on materials composition microtubes with diameters from one to ten micrometers can be obtained by this method. Tailoring of polymer patterns using photolithography enabled the fabrication of microtubes with tunable lengths and a desired number of rotations.
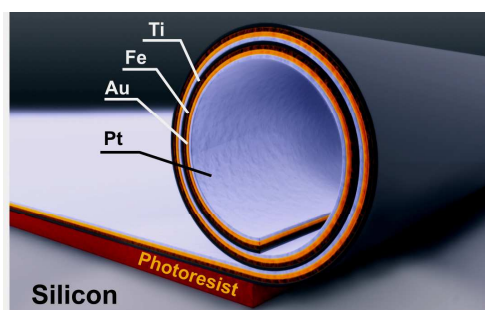
Scheme 2.1: Scheme of a novel method to roll-up microtubes by under-etching of sacrificial polymer layer. As example, a nanomembrane consists of Ti/Fe/Au/Pt layers. In this case, Ti stabilizes tubes, Fe is used for the magnetic control, Au is used for a better adhesion between layers, and Pt has a function of a catalyst to power the microjet engine.

2.1.1. Angular Deposition of Materials

Angular deposition of materials is used to create shadow window for underetching of sacrificial layer and integrate microtubes on a substrate. Photoresist patterns are prepared on silicon or glass substrates. During the fabrication of microtubes, the sam-

ples are tilted to a certain angle (60–75°) with respect to the direction of materials electron beam or thermal deposition, i.e., the technique named "angular deposition" is used. Figure 2.1 (A–C) shows a schematic of this process, here for the fabrication of catalytic microjets square photoresist patterns are used. However, depending on applications, other geometries of patterns can be used as well.
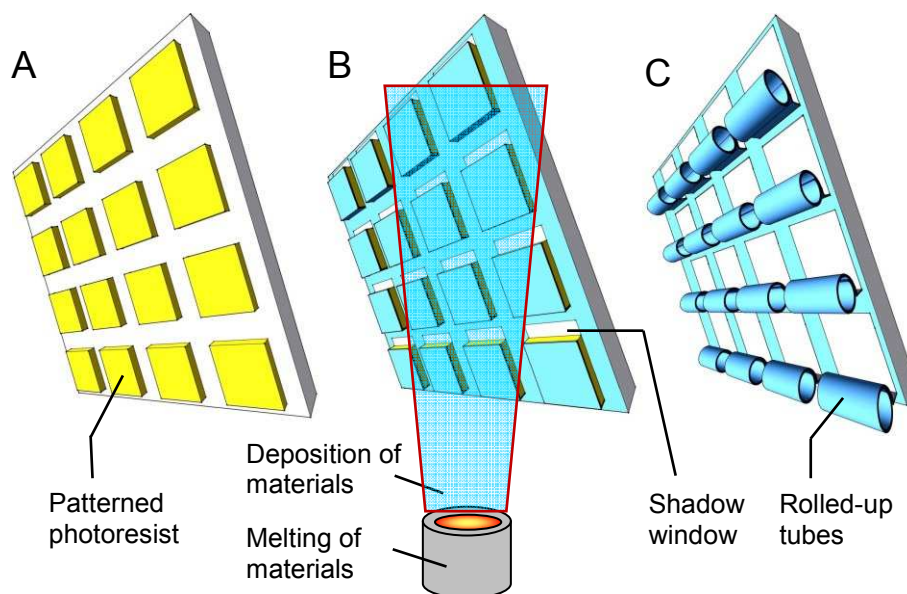
Figure 2.1: Schematic of a novel method "rolled-up nanotechnology on polymers". The fabrication process consists of the (A) preparation of polymer patterns using photolithography, (B) materials deposition (thermal, electron-beam), which fix nanomembranes to the surface, and (C) underetching of sacrificial polymer layer. Due to the created shadow window, the solvent underetches sacrificial layer starting from this side (note: solvent also underetches two sides that are perpendicular to the shadow window side. However, the layers do not roll-up from these directions because they are fixed to surface on the perpendicular side). Subsequently, microtubes are rolled-up and self-integrated on a planar substrate.

Figure 2.2 shows several illustrative examples of rolled-up microtubes with tunable lengths of 20, 100 and 1000 µm, which are used as catalytic micropumps (see Chapter 3). It is noteworthy to mention that many microtubes with the same thickness of layers can have slightly conical shapes (due to asymmetry of rolled-up layers). Although the conical shape can help to achieve the unidirectional recoil of microbubbles and propulsion of microjet engines, however, the controlled fabrication of microtubes with conical shapes was not the aim in this dissertation. Here, other parameters responsibe for the unidirectinal recoil of microbubbles were investigated. For instance, how tubular length (20–1000 µm) influence an activation of microbubbles, uni- and bidirectional recoils (Chapter 3). The length of self-propelled microjets was fixed to 50 µm (Chapters 4-7, 9) due to their ability to operate in a broader range of hydrogen peroxide concentrations.
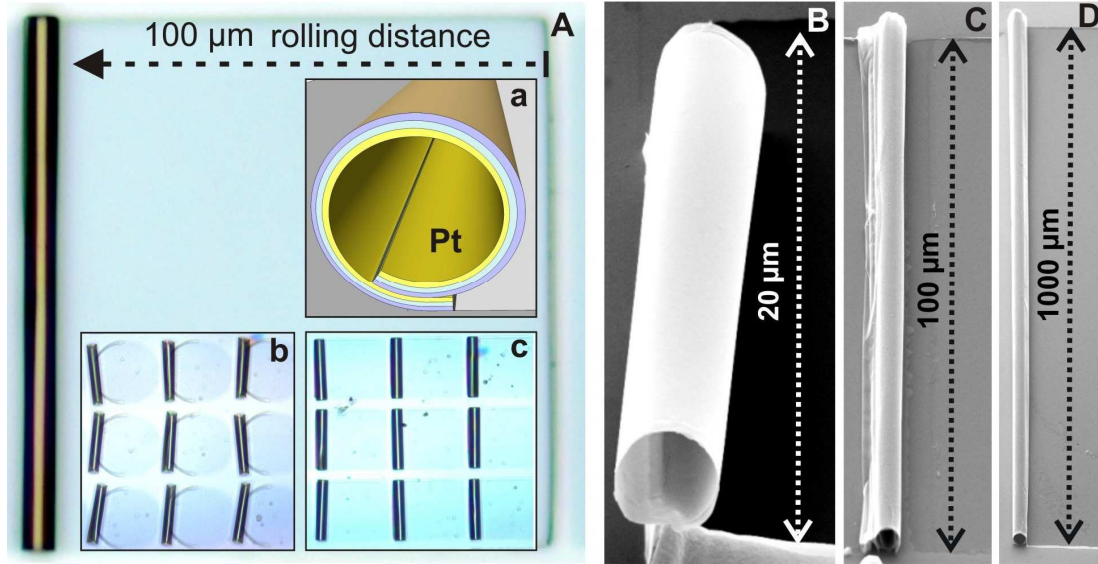
Figure 2.2: Examples of the fabricated microtubes. (A) Optical microscopy image of 100 μm long Ti/Cr/Pt microtube. Inset (a) shows schematic of the rolled-up layers with internal Pt layer. Arrays of microtubes are shown for circular (b) and square patterns (c). (B-D) SEM images which show microtubes with tunable lengths of 20, 100, and 1000 μm prepared for the application as "on chip" chemical micropumps (Chapter 3).

Determination of the thermal strain that affects the diameter of non-epitaxial microtubes is not a trivial task. However the diameter of microtubes from one to tens of micrometers can be controlled simply by changing the thickness of deposited layers. These thicknesses are typically several nanometers and they have to be calibrated for every e-beam machine. Dr. Mei determined that there are three major parameters influencing the strain state and thus the diameter of the rolled-up nanomembranes;[31] they include (i) difference in the thermal expansion between sacrificial layers and deposited films, controlled by substrate temperature, (ii) deposition rate, and (iii) stress evolution during the deposition. These parameters are not fully decoupled from each other, and advanced strain engineering is required for different materials combination in non-epitaxial films.[31] After the fabrication of microtubes, a supercritical point-drying machine was used to avoid the collapse of thin tubular walls during the drying process. Alternatively, microtubes were stored in liquid (for details see Appendix). For the reduction of jet engine diameter to nanoscale hybrid heteroepitaxial/catalytic InGaAs/GaAs/(Cr)/Pt layers were used (Chapter 8 and Appendix).

2.2 Measurements Setup and Data Analysis

In all experiments, microengines were investigated using optical microscopy with an integrated high-speed video camera. It allowed the *in situ* investigation of microjets

motion. The setup to control the motions of microjet engines (directionality and power) is described in this paragraph.

2.2.1. Setup for the Control of Microjets Motion using Magnetic Field

Microengine images were taken using a *Zeiss Axiocam MRc* camera and live videos were recorded using the high-speed *Photonic Science Limited* camera generating 50–900 fps. Video analysis was done using the free software *Image J, Virtual Dub.*
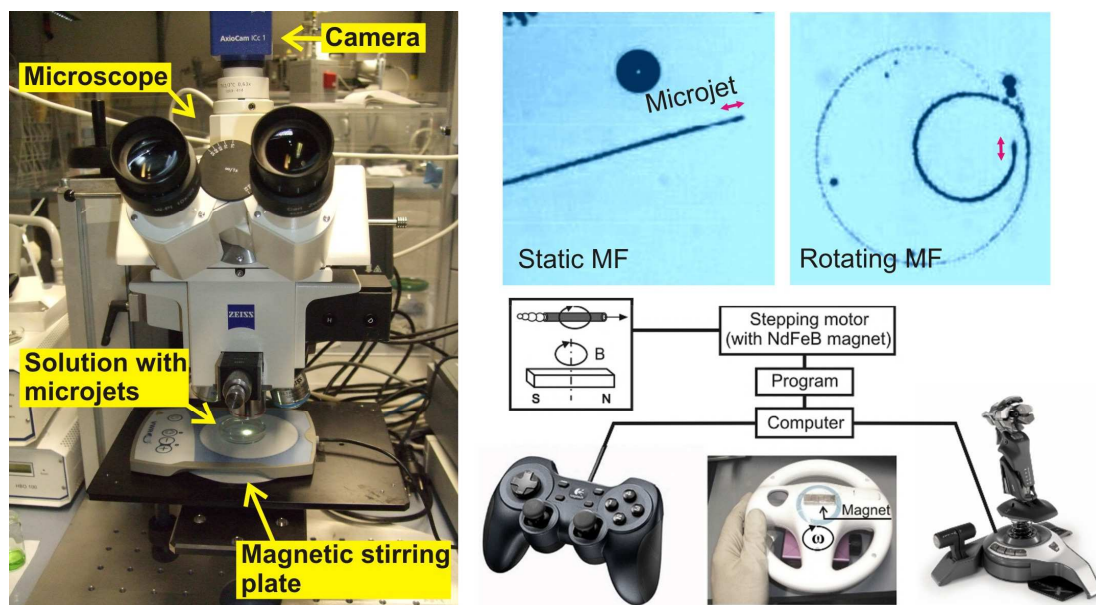
Figure 2.3: Setup for the observation and the remote magnetic control of microjets. Left image shows *Zeiss* microscope with integrated high-speed camera, where a magnetic stirring plate was used to confine the motions of microjets into circular trajectories. Right image shows examples of magnetic control of microjets. Optical microscopy images show individual microjets moving in straight (static magnetic field) and circular (rotating magnetic field) motions. It was found that the majority of microjets are aligned along the magnetic *B*-field. Microjets are synchronized with an angular velocity of a rotational magnetic field. An optional manual control was available using a steering-wheel with a magnet bar (if a strong magnet is used, the distance of the remote control can be as high as several tens of centimeters); joystick/gamepad interfaces with computer by *Labview* software (for details see Appendix).

Figure 2.3 shows optical microscope with integrated video camera and magnetic control method of catalytic microjet engines (Chapter 6). Microengines with integrated ferromagnetic (Fe) layers were controlled remotely using external magnetic field. Such control was achieved through a direct positioning of the mechanical actuator containing a permanent magnet ($10{\times}7{\times}5$ mm, which produces a field of around 50 Gauss around microengines), located underneath the sample. Alternative-

ly, a program was written to control a mechanical stepping motor, that was connected to a gamepad or joystick. Sen's group described previously the remote magnetic control of catalytic Au/Ni/Au/Ni/Pt nanorod-based nanomotors, which were aligned perpendicular to magnetic field lines.[22] Due to a high aspect ratio of microjets (ratio of the length to diameter) and a homogeneous magnetic layer in the rolled-up microtubes, it was observed that the majority of microjets are aligned parallel along magnetic field lines. Notably, no magnetization of layers was performed before the tubes were rolled-up. Magnetization of self-propelled microjets was realized directly in working solutions. A detailed investigation of magnetization was recently reported for tubular microhelix-like structures.[108] Such understanding can allow, in the near future, for the design of microjets with well-controlled magnetization for specific applications.

2.2.3. Setup for the Control of Microjets Power using Light

For the controllable power of microjet engines a white light source was used (Chapter 7). First of all i) a white light-source consisting of a halogen bulb 12 V, 100 W *Phillips*, which was the light-source of an optical microscope. Subsequently, microscope oculars with magnification of 5x-20x times were used for the simultaneous observation of microjets and their remote control by decreasing (dimming) and increasing intensity of light.
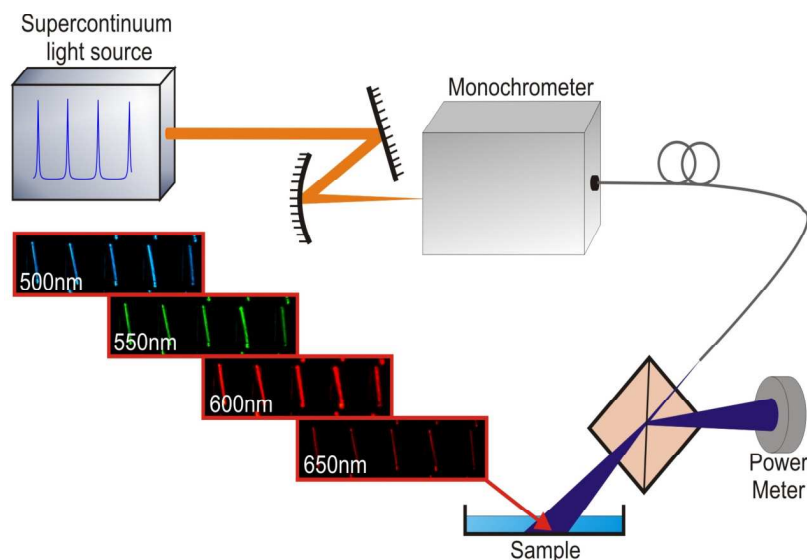
Figure 2.4. Laser setup for the control of microbubble frequency (microjet power) using laser source. Microjets were immersed into the solution of hydrogen peroxide [this setup was developed by Dr. E. J. Smith]. Intensity and spectral dependency investigations were performed using a supercontinuum light-source and monochrometer. A 50:50 beam-splitter was used to monitor the intensity with a power meter. Insets show optical images of microengines integrated on Si substrate and immersed in a solution of hydrogen peroxide illuminated at different light-wavelengths from 500 to 650 nm.

Secondly, a detailed investigation of bubble generation and the influence of light-power and wavelength was done using ii) a supercontinuum light-source generated by laser. For this purpose, a supercontinuum laser source in conjunction with a monochrometer was used to determine the spectral and intensity influence of visible light on the frequency of microbubbles (shown in Fig. 2.4). For this purpose, a defocused laser spot, emitted from a fiber running from the monochrometer, was directed onto the sample surface. Figure 2.4 shows the experimental setup consisting of the laser, the monochrometer, and a 50:50 beam splitter, which was used to monitor the intensity of the beam illuminating the sample with a power meter (optical resolution $\approx$ 2 nm full width at half maximum). Additionally, a flow of nitrogen gas was used in this experiment to remove accumulating microbubbles, which could block the laser beam. To eliminate a rapid consumption of the hydrogen peroxide with the catalytic reaction, a larger volume of solution was used, i.e., a Petri dish with a diameter d ~ 50 mm.

2.3 Fabrication of Poly-Di-Methyl-Siloxane Microfluidics

PolyDiMethylSiloxane (PDMS) is an important material utilized mainly in fabrication of microfluidics for lab-on-a-chip devices and rapid parallel testing and analysis in biotechnology.[109] The PDMS formula is $CH_3[Si(CH_3)_2O]nSi(CH_3)_3$, where n is the number of repeating monomer [$SiO(CH_3)_2$] units. PDMS has additional advantages of easy preparation, optical transparency, high elasticity, thermal stability up to 150° C, and resistance to many chemicals. PDMS contains molecules with flexible polymer chains due to their siloxane linkages.[110] The fabrication steps of microfluidic channels are shown in Fig. 2.5 (details are provided in the Appendix). Microfluidic channels were used for the investigation of microengine motion in microfluidic channels (Chapter 6). For easy injection of microjets, a reservoir was cut-off for addition of a solution with microjets. Pumping of fluid into the inlets transports microjets into the working area of chip, which contains several channels. Cargo consisting of microparticles were usually added into the same reservoir together with microjets and the hydrogen peroxide fuel. It was determined that a high concentration of surfactant (more than 10 % v/v) must be used to stabilize microbubbles in microchannels. Once microengines were injected into the microfluidic channels, a slow flow was introduced that delivered the fuel into the working area and removed accumulated microbubbles. At the same time, microengines motion along and against the flowing fluidic streams was studied. Since ferromagnetic catalytic Ti/Fe/Cr/Pt microjets were used, they were controlled to pick up and transport cargo polysterol microparticles.
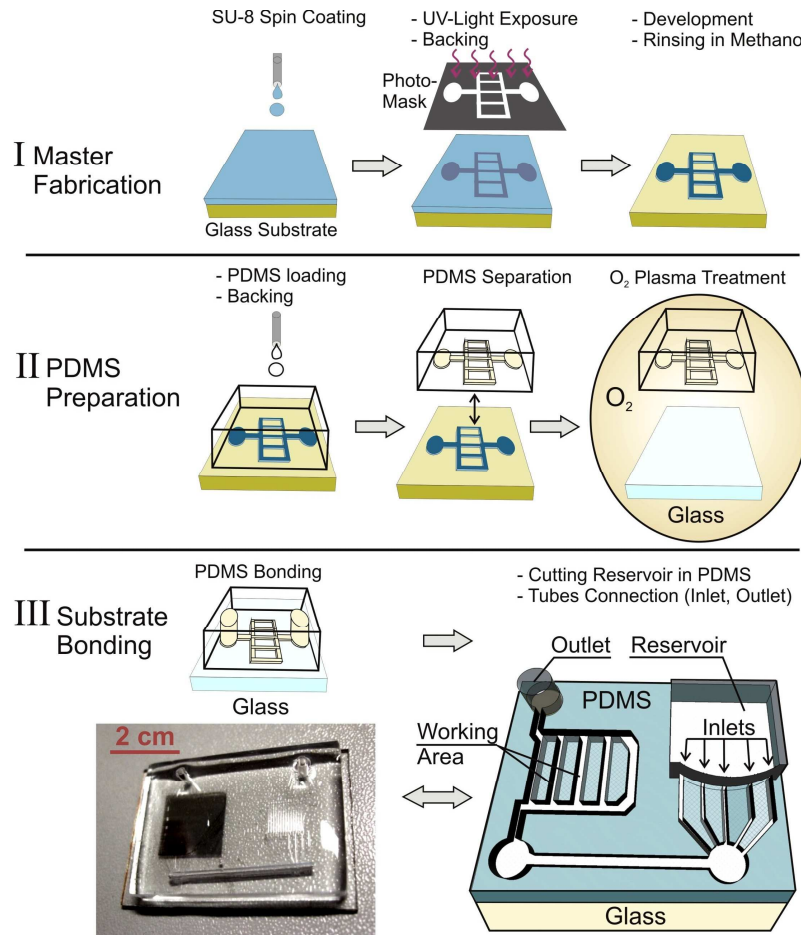
Figure 2.5: Procedure for the fabrication of PDMS microfluidics. (I) Fabrication of *SU-8* master stamp using spin-coating, layer exposure to UV light, development and baking; (II) pouring of PDMS in a casting mold with the *SU-8* structure at the bottom, baking, peeling off, and surface activation through treatment of PDMS and glass substrate in oxygen plasma; subsequently (III) the bonding of PDMS to the surface of glass is done. Finally, the reservoir is cut off for easy injection of microengines into microfluidic channels [the procedure was developed in collaboration with S. Harazim].

2.4 Optimization of the Fuel Solution

Nucleation of Bubbles in Gas-Collecting Cavities

Microengines represent tubular gas-collecting cavities. Understanding the mechanisms of bubble nucleation, growth, and recoil at the microscale helps to define working conditions for microjet engines driven by the catalytic reaction of hydrogen peroxide decomposition into oxygen bubbles and water. Fig. 2.6 A shows a growth of bubbles from the rolled-up catalytic microtubes in aqueous solution of hydrogen peroxide (solution without surfactants). According to Jones, Evans, and Galvin [111], nucleation of bubbles usually occurs at *nucleation sites* on surface cavities or defects. In the absence of solid cavities, a nucleation of bubbles requires high levels

of gas saturation. In case of surface cavities, the nucleation energy barrier is reduced, i.e., less interfacial free energy is needed for the bubble to grow to a nucleus of critical size. At low levels of gas saturation, bubbles can only nucleate in solid cavities. In general, for a complete understanding of nucleation, a broad range of parameters must be met, including molecular diffusion of gas molecules, which leads to "embryo" growth, indicated schematically in Fig. 2.6 B. In a gas cavity, the pressure elevation is described by the Laplace equation, which can be used to estimate the critical radius of bubble curvature.[111]
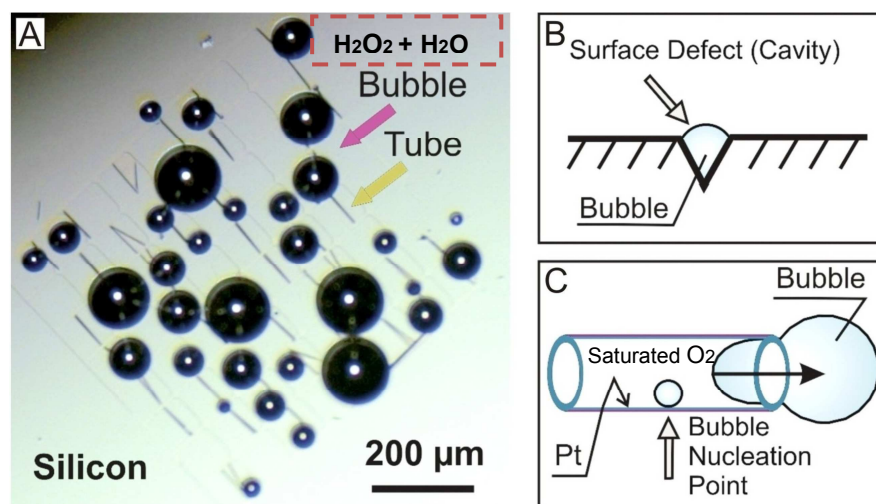
Figure 2.6: Catalytic microtubes in aqueous solution of hydrogen peroxide (without surfactants). (A) Bubbles, indicated by red arrow, grow in the solution of hydrogen peroxide and water from Pt microtubes, indicated by yellow arrow. Such bubbles reach diameters of over 100 micrometers and do not detach; (B) schematic of surface defect with nucleated bubble "embryo" on this defect; (C) schematic of bubble nucleation in an individual catalytic platinum microtube, which plays the role of gas-collecting cavity.

The generation of bubbles starts at a high level of gas saturation. When considering catalytic microtubes, it was found that microbubbles nucleate from the same points within rolled-up microtubes, indicating that cavities/defects exist on the surface. The origin of surface defects in catalytic microtubes has not yet been determined. It is hypothesized that these defects can originate from the rolled-up layers or they may be present due to the materials' preparation methods. In general, catalytic tubular cavities limit diffusion of gas molecules due to solid boundaries and thus, the concentration of gas molecules is higher within the microtubes. This effect leads to an activation of bubble growth from catalytic microtubes at lower concentrations of hydrogen peroxide in comparison to bubble generation on a planar surface. The length of catalytic microtubes has a critical influence on the generation of microbubbles, i.e., much lower concentrations of peroxide fuel is required to generate mi-

crobubbles in longer microtubes (see Chapter 3). Figure 2.6 A shows catalytic micro-tubes in hydrogen peroxide without surfactants. In this case bubbles grow without recoil and reach millimeter-scale size. Such big bubbles cannot be used to propel microjet engines. Furthermore, it was found that most catalytic microtubes unroll when released from a surface due to a high surface tension of water and hydrophobic effect of thin rolled-up nanomembranes.

Effect of Surfactants on the Generation of Bubbles

It is well-known that surfactants play an important role in solutions for stabilization of bubbles.[112] Generally, a surfactant is a molecule made of two parts, each part having a different affinity. The hydrophilic part shows affinity to water, and the hydrophobic part repels water. Three types of surfactants are exemplified in Fig. 2.7. The surfactant molecule can be divided into non-ionic, anionic, and cationic, classified by the presence of charged groups in its head. A non-ionic surfactant has no charge groups in its head and the head of an ionic surfactant carries a net charge. An addition of surfactant, which can be a common soap or specific agents, reduces significantly surface tension and the size of microbubbles. Surfactants reduce high surface tension of water (71.97 mN/m) by several factors. Benzalkonium Chloride (BC) cationic surfactant [113] or a common soap (*Fit Gmbh*) were used throughout this dissertation to prepare the fuel solution for microjet engines. The structure of BC is shown in Fig. 2.7 (A). In some cases, a common soap was used containing 5–15 % of anionic tenside, amphoteric tenside (< 5%), bronopol, benzisothiazolinone, and methylisothiazolinone. Application of common soaps showed that no degradation of thin Pt catalytic films occurred during several hours of microjets operation. In the case of biocatalytic catalase-based microjet engines, Sodeum Dodecyl Sulphate (SDS) surfactant was used. Influence of BC concentration on the generation of bubbles and the propulsion of microjet engines is shown in Chapters 3 and 4. However, in some cases, it is possible to avoid the addition of surfactant and reduce surface tension using organic solvents (described in Chapter 9). When a concentration of surfactant is increased, the micelles can form, as shown schematically in Fig. 2.7 (B). Micelles, which appear above a critical concentration of amphiphilic molecules, are called the Critial Micelle Concentration (CMC). For concentrations below the CMC (for SDS CMC is around 0.045 w/v % [114]), molecules are present in the bulk separately; for concentrations above the CMC, surfactants self-assemble into micelles. At higher concentration of surfactants, the interfacial tension decreases and the interface coverage is increased using surfactant molecules, causing the decrease of interfacial energy. Fig. 2.7 (C) shows this effect – the decrease in surface tension continues until the interface is saturated, i.e., at the indicated CMC point. After this, the interfacial tension continues to decrease but more slowly. Fig. 2.7 (D) shows a dramatic effect of surfactants: the generated microbubbles have much smaller size than in Fig. 2.6.
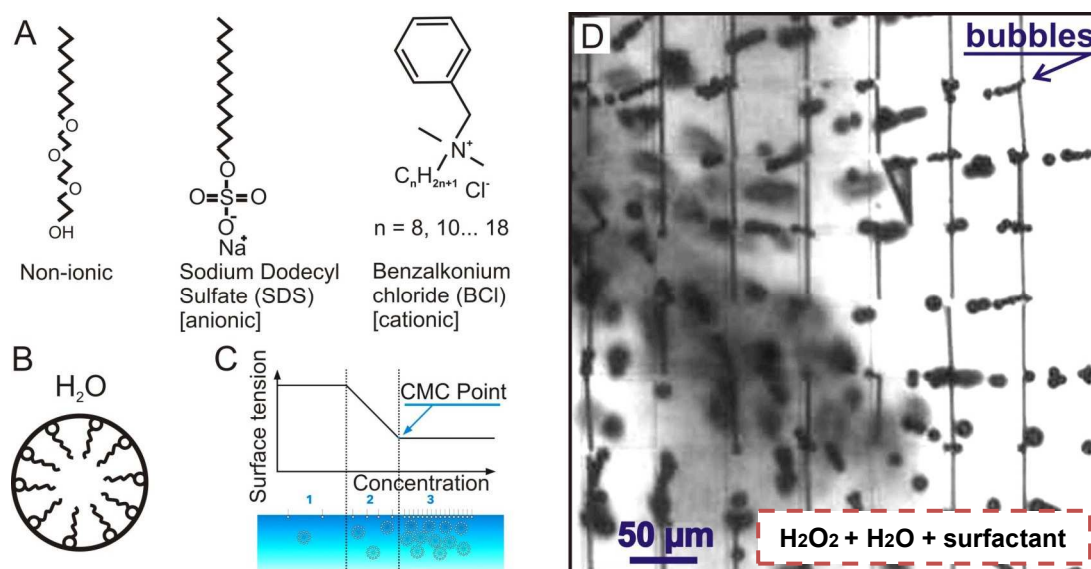
Figure 2.7: Effect of surfacants on the generation of microbubbles. (A) Examples of different surfactant types (non-ionic, anionic, and cationic). (B) Schematic diagram of a steric micelle, where the hydrophobic tails are in the center and hydrophilic heads are located outside. (C) Graph showing typical dependence of surfactant concentration and micelles on the liquid surface tension. (D) Effect of surfactant addition (here a common soap "Fit-waschmittel" is used) indicating a dramatic reduction of the bubbles size.

2.5 Materials for the Biocatalytic Microjets

Biocatalysts, like catalase enzymes, are well-known to have one of the highest intrinsic turnover rates. This property makes them excellent candidates for the design of biocatalytic microengines. Biocatalysts can help in finding more efficient mechanisms to convert chemical energy from hydrogen peroxide or allow glucose as a fuel source. Mano and Heller reported on biocatalytic nanomotors, which move via glucose–oxygen reaction.[115] A functionalized carbon fiber (1 cm long) was fabricated with bilirubin oxidase (oxygen-reducing enzyme) and Glucose Oxidase (GOx), which catalyzes the oxidation of glucose to δ-glucono-1.5-lactone. Enzymes were immobilized on carbon using redox polymer bridges to achieve efficient electron transfer between the enzymes and the fiber. When such fibers were placed on the surface of glucose solution, they started to move with the GOx end forward. It was hypothesized that the main mechanism of propulsion is gradient of protons, which can change a surface tension. Feringa's group showed glucose-powered nanomotor by coupling GOx and catalase on the same carbon nanotube.[116] The GOx converts glucose and oxygen to gluconolactone and hydrogen peroxide. In the next step, the hydrogen peroxide is decomposed by catalase to oxygen and water. Biocatalytic Ti/Au/SAM/Catalase microjet engines, shown in Chapter 5, represent an effective alternative to achieve direct motion. Ti/Au microjets were modified with thiol groups

to enhance catalase linkage (biofunctionalization experiments were done by Dr. S. Sanchez, for details see Appendix). This step allowed an operation of enzymes for decomposition of hydrogen peroxide. Next step requires an application of glucose as a fuel and it is currently under development in our group.

3 Chemical Pumps based on the Micro-Jet Engine

This chapter reports about catalytic Ti/Cr/Pt tubular micropumps.[21] Micropumps are integrated on a planar silicon substrate. Micropumps have diameters from 5 to 10 μm and tunable lengths in the range 20–1000 μm. When immersed into a solution of hydrogen peroxide with surfactant, the micropumps are activated by the catalytic decomposition of peroxide into oxygen microbubbles and water. Fluid pumping is revealed by the movement of polystyrene particles through the catalytic micropumps, shown in Scheme 3.1. A concentration of 0.06 v/v % H_2O_2 was determined to be sufficient to generate microbubbles and, thus actuate the micropumps. Different lengths of micropumps and concentrations of peroxide fuel are investigated (parts of this Chapter were adapted from ref.[21]).
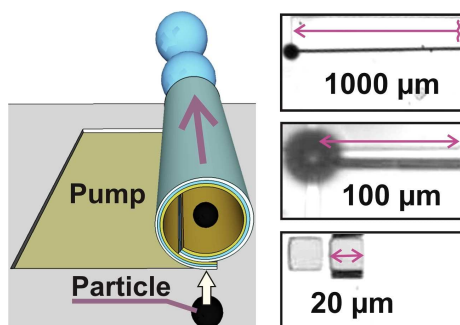
Scheme 3.1: Catalytic tubular micropumps integrated on a planar substrate. Left side sketch shows schematic of individual micropump. Right side sketch represent optical microscopy images of micropumps with different lengths.

3.1 Introduction

Efficient pumping, mixing and moving of fluids at the microscale are essential for miniaturization of dynamic devices and machines. For instance, micropumps have numerous applications and are widely used in ink-jet printing,[117] drug delivery,[118] fluid transportation on a chip [119] and in remotely powered self-propelled diodes.[120, 121] Fluid pumping at the microscale is challenging due to the high viscosity of fluids dominating at low Reynolds numbers.[4] It has been demonstrated previously that it is possible to induce fluid motion by external sources based on electrical,[122] electrochemical [123] and thermal [124] principles, for instance. An elegant way of pumping fluid without external pumps or sources relies on the catalytic reactions that can take place on the surfaces of the microfluidic pumps. In particular, electrokinetic pumping based on the catalytic decomposition of hydrogen perox-

ide into oxygen and water was recently realized on planar bimetallic surfaces.[125, 126, 127, 128] In comparison to previously reported catalytic pumping above planar surfaces, tubular catalytic micropumps offer compact fluid pumping as well as easy integration into Lab-on-a-Chip devices and self-propelled micromachines. The integration of non-catalytic rolled-up microtubes into microfluidic devices was previously demonstrated in our group.[129] Previously, Schmidt and Eberl have suggested to generate bubbles in fluids ejected from rolled-up micro- and nanotubes.[130] In the present approach microjet engines are fixed on the substrate and by making use of the catalytic reaction inside, the pumping of fluid through the hollow structure is achieved. The directed motion of polystyrene microparticles is demonstrated through the tubular micropumps, and the optimum concentration range suitable for unidirectional fluid motion is studied.

3.2 Results and Discussions

Arrays of compact Ti/Cr/Pt micropumps were integrated on planar silicon substrate. Upon addition of hydrogen peroxide fuel micropumps generate bubbles which pump fluids. Figure 3.1 (A) shows schematic of individual array of fabricated micropumps prepared on a planar substrate by rolled up nanotechnology on polymers. Figure 3.1 (B) illustrates the pumping principle consisting of a bubble nucleation, growth and recoil. According to the model of microjet (Chapter 1) the migrated bubbles must trigger the pumping of fluids.
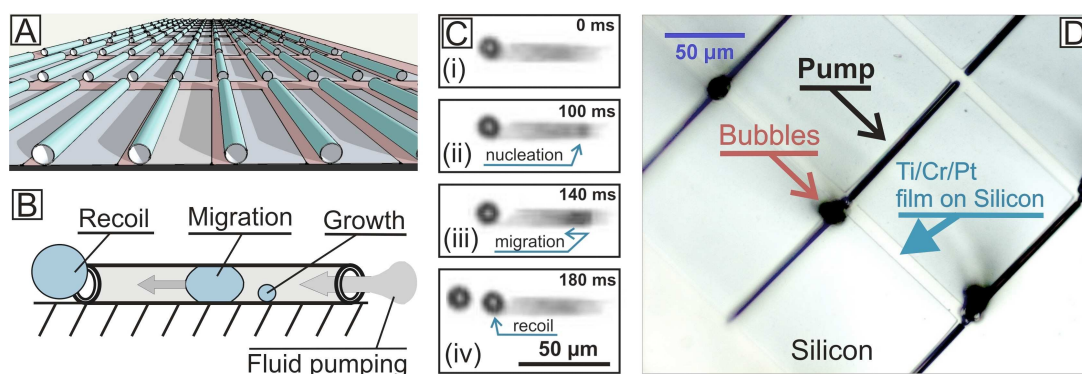
Figure 3.1: Catalytic tubular micropumps on a planar substrate. (A) Schematic of the fabricated micropumps. (B) Schematic of the pumping princple by bubbles. (C) Optical microscopy images (i-iv) of bubble migration and recoil during 180 ms (fuel used: H_2O_2 v/v 2.5 % aqueous solution, BC v/v 0.5 %). (D) Optical microscopy image of integrated and working Ti/Cr/Pt micropumps. Black arrow shows individual micropump. Red arrow shows bubbles recoil and blue arrow indicates stripes of deposited thin film (from which micropumps rolled-up), where generation of microbubbles from a planar catalytic film is not observed.

Figure 3.1 (C) shows optical microscopy sequences of operating micropump during period of time $0 - 180$ ms (i-iv). An estimated migration of microbubble in microtubes has an average speed of 2 mm·s^{-1}. It corresponds to Reynolds numbers in the range between 10^{-3} and 10^{-2} which is the regime of low Reynolds number. Subsequently, the flow in a microtube is laminar and such fluids are challenging to pump. Fig. 3.1 (D) shows several micropumps with 100 μm length. Arrow shows Ti/Cr/Pt thin film deposited on Si (from which micropumps rolled-up). Since no bubbles recoil was observed from such thin catalytic films on surface, it is clear evidence that molecular oxygen diffuses out of surface without the nucleation of bubbles. It proves that catalytic microtubes represent gas collecting cavities. For instance, planar deposited Ti/Cr/Pt (Pt top layer) films, i.e., the same layers from which the micropumps were shaped, microbubbles are not generated, Fig. 3.1 D. Detail analysis of micropumps activation, lengths, bubble recoil and fuel conditions are considered in the following pages.

3.2.1. Pumping and Sorting of Particles

For demonstration of micropumps catalytic microtubes were fabricated on silicon substrate. As a representative example, Figure 3.2 A (left) shows an optical microscopy image of a 100 μm long Ti/Cr/Pt micropump immersed in an aqueous solution of hydrogen peroxide (1 % v/v H_2O_2, 0.5 % v/v BC).
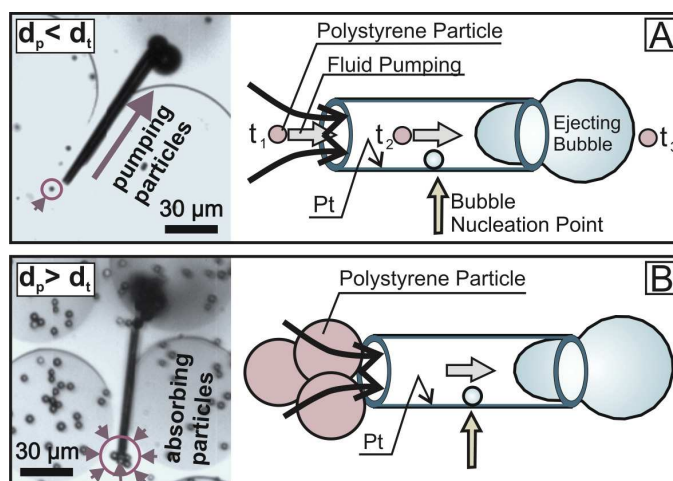
Figure 3.2: Catalytic pumping of polystyrene particles by Ti/Cr/Pt microtubes. (A) Left: optical microscopy image showing a rolled-up micropump on a silicon substrate sucking in a small microparticle. Right: sketch showing the nucleation and release of microbubbles out of the micropump. (B) Left: optical microscopy image showing large microparticles absorbed at the mouth of the micropump. Right: sketch of the process taking place. Grey arrows indicate the direction of the fluid flow.

The platinum surface at the inside of the micropump initiates the catalytic decomposition of H_2O_2 solutions inducing the motion of fluid. The direction of the fluid is governed, in principle, by the slight asymmetry of the tube geometry, causing the fluid to move towards the larger opening which is visualized in Fig. 3.2 A by the transport of polystyrene microparticles. As a result, particles with a diameter smaller than the microtube, i.e. $d_p < d_t$, are sucked into the micropump, Fig. 3.2, A. A slow oscillation of the microparticles near the mouth of micropump. It is attributed to the growth and recoil of microbubbles within the micropump. At time t_1, the particle follows the fluid streamlines, then comes into the micropump body (t_2) and finally is pumped out (t_3).

The motion of the particles is synchronized with the growth and migration of microbubbles which displaces fluids within the micropump. Fig. 3.2 B left shows an optical microscopy image of the polystyrene microparticles with 7 μm diameter, which are larger than the mouth of the micropump, $d_p > d_t$. In this scenario, particles are absorbed at the entrance of the micropump while the micropump is still active. Fig. 3.2 B, right, shows a schematic diagram of the absorbed particles at the micropump mouth. These large microparticles do not block completely the entrance of the tube as can be confirmed by the continuous generation of microbubbles coming out from the opposite opening. The micropumps are capable to move particles into and through their body. Since the diameter of the microtubes can be tailored, the tubular micropumps could be used for sorting of particles with different sizes.
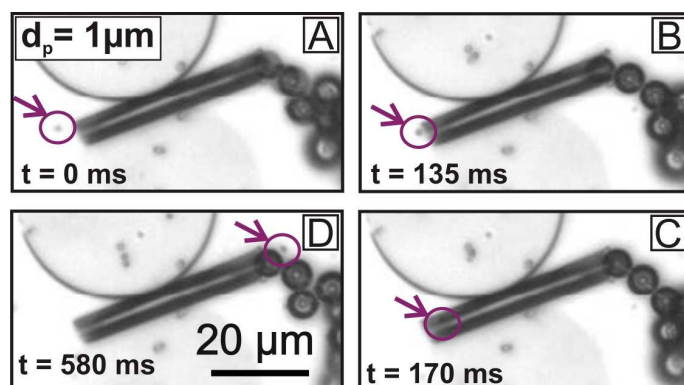
Figure 3.3: Sequence of optical images of a tubular micropump which moves microparticles through its hollow body. Arrows show a tracked individual polystyrene microparticle with a diameter of 1 μm. At the time t = 0 (A), the particle comes into close proximity of the micropump mouth, at 135 ms it approaches entrance (B), at t = 170 ms it is sucked inside (C) and after 580 ms it is pumped out (D). Large black spheres exiting the micropump are oxygen microbubbles.

A more detailed study regarding the pumping of particles is shown in Fig. 3.3 where a microparticle can be visualized and tracked through the micropump. For this purpose, a micropump with length 40 μm and diameter 5.6 μm was selected, i.e.,

with an aspect ratio of 7. Figure 3.3 (A–D) shows the pumping of an individual polystyrene microparticle with a diameter of 1 μm accomplished over 580 ms. This micropump operates at an average frequency of 7 bubbles sec^{-1} (fuel: 1.0 % v/v H_2O_2, 0.5 % v/v BC) measured over 15 seconds. At the time t = 0 sec, the particle is located in close proximity to the mouth of the micropump.

When a bubble inside the micropump migrates and finally recoils at t = 135 ms, the tracked microparticle moves immediately closer to the mouth. Afterwards, the motion of the next microbubble through the tube sucks more fuel bringing along the particle into the micropump where it remains until t = 580 ms when it is released together with the next microbubble. Another micropump with the same length operates at an average frequency of 40 bubbles s[-1] (fuel: 4.0 % v/v H_2O_2, 0.5 % v/v BC). Therefore, an increase of the peroxide concentration leads to a higher pumping activity. It was previously hypothesized that mainly a change of the microtube diameter (conical shape) leads to an asymmetric release of bubbles only from the larger tubular opening. However, a clear conical shape is not always detectable by optical microscopy, as shown in Fig. 3.3 and additionally a generation of bubbles in both directions has been observed.

3.2.2. Optimization of the Fuel Concentration

It is of particular interest to pump fluid in unidirectional fashion. Indeed, for practical applications, the fluidic micropump remains a useful device only if it is not 'overloaded', i.e., when bubbles recoil and a fluid is pumped only in one direction. Hence, it is important to investigate and control the conditions in which the microtubes can generate microbubbles at one or both ends. Fig. 3.4 illustrates the change in directionality of the pumping depending on the concentration of H_2O_2 for 100 μm long Ti/Cr/Pt micropumps. Fig. 3.4 A-B shows optical microscopy images (bottom) and schematics (top) of the 'unidirectional' (Fig. 3.4 A) and the 'overloaded' (Fig. 3.4 B) pumping regimes. To obtain statistical data 20 different micropumps per silicon substrate were tested. The data showed reproducible results for different samples. For concentration of the peroxide below 3 v/v % H_2O_2, Fig. 3.4 C left y axis, not all catalytic micropumps are activated. However, by increasing the fuel concentration up to 3 v/v %, an activation of all micropumps was achieved. Interestingly, when the concentration of peroxide is above 0.5 % v/v, the unidirectionality of the bubbles recoil is broken, Fig. 3.4 C right y axis. The number of micropumps which remain pumping in one direction decreases dramatically from 100 % at 0.5 % H_2O_2 to 40 % at 1 % H_2O_2. However, when all the tubes are active (i.e. at 3 % H_2O_2), only 15.5 % of them are pumping unidirectionally. At 1 v/v % of H_2O_2 approximately 60 % of the micropumps experienced overloading, however not all of them were activated (76 % remained inactive). To explain this phenomenon, it is hypothesized that in the region

above 0.5 v/v % peroxide, the catalytic generation of microbubbles is so high that there is a limitation of physical space inside the tubular micropump. At lower concentrations, a steady-state of directional flow is created when bubbles moving within the tube draw new peroxide from one end (see Scheme in Fig. 3.2 A). Since the migration of bubbles within the tube is slower than the generation of new bubbles, they may collide inside the micropump causing the bubbles to eventually move towards the opposite direction thus exiting from both tubular openings. Similarly, the accumulation of bubbles in a microtube at higher peroxide concentration was also observed for self-propelled microjets, which was transferred to a saturation *plateau* of their speed upon an increase of the peroxide concentration.[23]
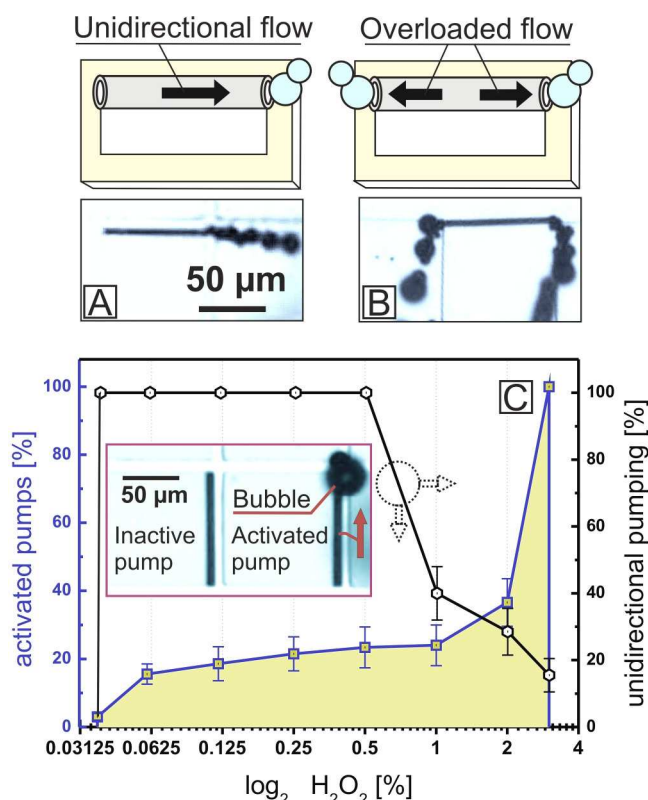
Figure 3.4: Characterization of the microbubbles recoil for the pumps with length of 100 μm. Optical microscopy image and schematic diagram of (A) the unidirectional and (B) the overloaded fluid flow. (C) Percentage of activated micropumps and unidirectional flow regime with different concentrations of the hydrogen peroxide. The inset shows inactive and activated micropumps. Red arrow indicates the direction of flow within the tubes.

The effect of hydrogen peroxide concentration on the bubble frequency and size for 100 μm long micropumps was studied (Fig. 3.5). The bubble frequency increases upon increasing the fuel concentration, i.e., from 2 to 25.8 Hz. Thus, at higher peroxide concentrations, the required time for bubble nucleation and release is shorter than at lower concentrations. It was observed that the bubbles which remain

connected to the tube longer times can acquire larger radii. For example, at 4 % H_2O_2 they are ejected after 0.052 sec while at 0.5 % H_2O_2 the bubbles are released every 0.35 sec. As a consequence, the bubble radius diminishes from 17.3 μm to 9.7 μm, correspondingly.
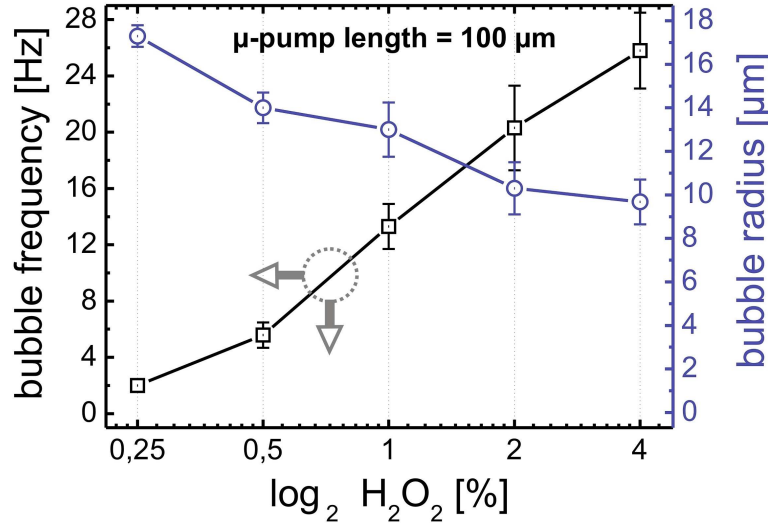
Figure 3.5: Bubble frequency and radius at different concentrations of hydrogen peroxide. Micropumps have a fixed length of 100 μm.

3.2.3. Optimization of the Micro- Pump Length

Because of the versatility of rolled up nanotechnology on polymers technique, it is possible to tailor the micropump sizes easily from 20 to 1000 μm length (Figure 3.6). The length tunability allows for a full identification of the effective pumping working area (micropumps activitity without overload) for each determined size. The region (i) in Figure 3.6 represents inactive pumps where no microbubbles are observed, (ii) indicates an area where micropumps are active with unidirectional pumping, and (iii) shows the overloaded area (here at least one pump generated bubbles from two openings). Micropumps of 1000 μm length require the lowest concentration of hydrogen peroxide to be active (0.009 v/v % H_2O_2) which is 750 times lower than the 20 μm long micropumps. However, their range of unidirectional pumping remains only up to 0.2 v/v % H_2O_2 limiting their applicability. Micropumps of 100 μm length require peroxide fuel (0.062 % 20 H_2O_2) 16 times lower than for 20 μm micropumps, but their unidirectional pumping can be only extended up to 0.5 % H_2O_2. A full working region of unidirectional pumping is shown in the inset table of Figure 3.6. Each point represents an average measurement from 20 to 50 different micropumps. It is clearly observed in Fig. 3.6 that shorter tubes, e.g., 20 – 40 μm long, maintain their directional fluid motion (unidirectional pumping) for larger concentration ranges than longer tubes with, e.g., 60 – 1000 μm length, 260 micropumps located in 2

different samples were studied. Figure 3.7 A depicts the population of activated micropumps with lengths ranging from 20 to 1000 μm soaked in three different concentrations of hydrogen peroxide of 0.5, 3 and 5 v/v %. At 0.5 v/v % H_2O_2, only 3 % of the 60 μm long pumps, 15 % of the 80 μm pumps, 29.1 % of the 100 μm pumps and 100 % of the 1 mm long are activated. While increasing the H_2O_2 concentration up to 3 v/v %, 8.3 % of the 40 μm pumps start to generate fluid motion by the generation of bubbles, 12.5 % of 60 μm long pumps, and 75 % of the 80 μm long pumps are active. Thus, shorter tubes need higher concentration of peroxide to be catalytically active. Finally, at 5 v/v % H_2O_2 all population of micropumps from 60 – 1000 μm long but only 27.7 % of 40 μm pumps are active.

Micropump length (μm)	Threshold H_2O_2 (%,v/v)	Unidirectional pumping H_2O_2 (%,v/v)
1000	0.009	0.009 - 0.2
100	0.062	0.062 - 0.5
80	0.125	0.125 - 1
60	0.5	0.5 - 1.5
40	1	1 - 3
30	3	3 - 11
20	7	7 - —
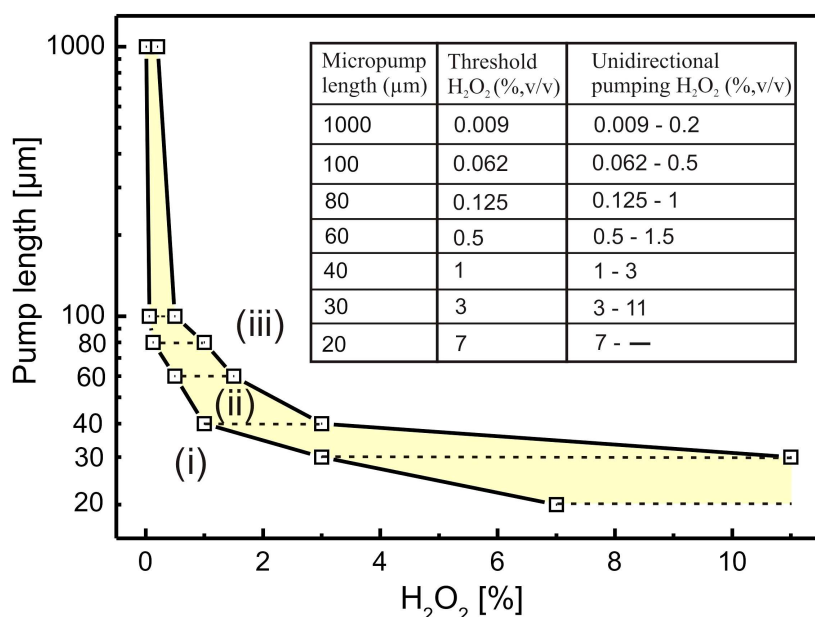
Figure 3.6: Activity regimes for variable Ti/Cr/Pt micropump lengths ranging from 20 to 1000 μm as a function of hydrogen peroxide concentration. Yellow region represents working area for the unidirectional microbubbles recoil. Inset table shows details for data points shown in the graph, indicating a threshold peroxide concentration and unidirectional pumping range. Dashed horizontal lines show ranges of the peroxide concentrations suitable for unidirectional pumping.

As discussed in Fig. 3.6, 20 μm long micropumps require substantially higher concentration of the hydrogen peroxide fuel for catalytic generation of microbubbles. However, they are not overloaded even at higher peroxide concentrations which are in agreement with our previous hypothesis regarding the limitation of physical space for microbubbles within the microtube. Figures 3.6 and 3.7 reveal that the length of the microtube contributes significantly to the catalytic generation of oxygen microbubbles and consequently to the fluid motion inside the micropumps. Longer micropumps contain inherently a larger Pt catalyst surface area than shorter ones. For

example, micropumps with length 1000 μm contain up to 125 times larger inner surface area of the catalyst than the 20 μm micropumps. Therefore, the inactivity of short micropumps, Fig. 3.7 A–B, at substantially high concentrations of the hydrogen peroxide shows that the rate of oxygen formation is limited by the surface area of the micropump. Furthermore, it has been shown before that microbubbles nucleate better if the catalytic surface contains defects or cavities which reduce significantly the bubble nucleation energy barrier.[111] It is thus expected that longer tubes with larger catalytic surface area may contain more defects than shorter microtubes.
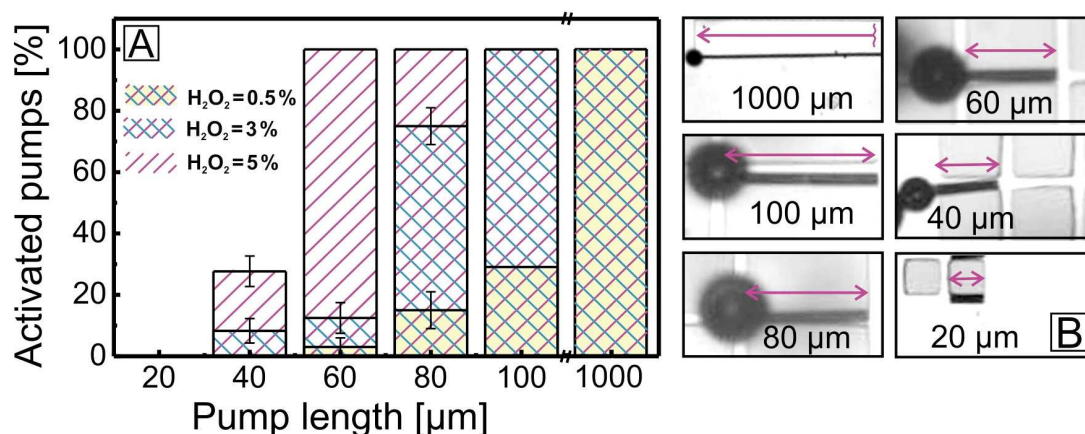
Figure 3.7: (A) Population of activated micropumps in different concentrations of the hydrogen peroxide fuel. (B) Optical images of the catalytic micropumps with different lengths. Black rounds are microbubbles and arrow bars show lengths of the micropumps.

3.3 Summary

The rolled-up tubular catalytic micropumps are demonstrated. Depending on applications different parameters for micropumping of fluids can be used. The micropumps require low concentrations of hydrogen peroxide, 0.05% v/v to be activated and start the generation of oxygen microbubbles. However, longer micropumps require even lower concentration of hydrogen peroxide to start pumping fluids in comparison to shorter micropumps. Longer micropumps can not generate bubbles in unidirectional manner over a wide range of hydrogen peroxide concentrations. They are easy "overloaded" and microbubbles start recoiling from both tubular openings, which does not lead to an efficient unidirectional pumping. A better understanding of key parameters such as the catalyst turnover rate, catalyst surface area, concentration of the fuel, and existence of surface defects will permit the construction of more efficient micropumps. In future studies it will be interesting to model the interplay between reaction and diffusion processes in microscale tubes, that leads to the formation of bubbles. This process must represent the major factor of micropumps activation. This may enable the design of more energy efficient microengines. For instance, it can be a

bottle-like microstructure, where tubular openings are smaller than the diameter of tubular body. The restriction of the diffusion of reaction products can lead to more efficient saturation of gas molecules, nucleation of microbubbles with air-liquid interface stabilized by surfactants. It is proposed that the pumping principle can be elaborated in not too distant future into lab-in-a-tube analytical systems [131] and self-propelled "roving micropumps", which can potentially convert toxic elements in rivers and lakes into environmentally friendly products.

4 Autonomous Motion of Catalytic Micro-Jet Engines

Microjet engines made of Ti/Cr/Pt and Ti/Fe/Au/Ag catalytic microtubes move autonomously in solutions of hydrogen peroxide. Concentrations of surfactant and hydrogen peroxide are optimized to achieve more efficient motion. Microjets' stepwise motion is reported and leads to deterministic propulsion, where microengines speed can be approximated as a product of bubbles radius and frequency. Different trajectories of motion are observed and can be divided manly into straight, circular and helical motion, represented in Scheme 4.1 (parts of this Chapter were adapted from refs.[20, 31, 32]).
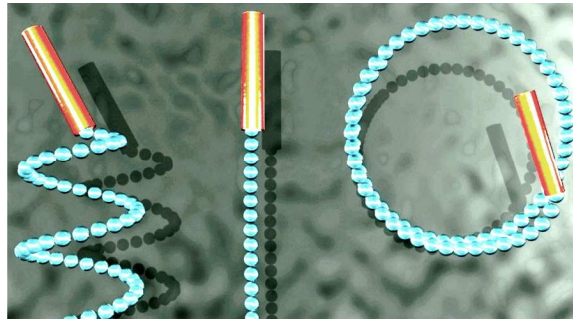
Scheme 4.1: Self-propelled microjet engines, located in the fuel solution of hydrogen peroxide.

4.1 Introduction

Autonomous man-made machines represent machines which are capable to accomplish tasks without human guidance. One example of such machines are autonomous robots,[132] which include abilities to cope with their environment, process information, operate for a substantial period of time and move. So far, autonomous machines at the micro- and nanoscale are challenging to achieve. One approach consists in the exploration and identification of emerging behaviour of self-powered objects.[80] For instance, the group of Sen reported non-biological chemotaxis and phototaxis of autonomous nanomotors.[78] To realize such goals, first of all, continues and effective motion of micromachines must be achieved. In recent years, substantial efforts has been dedicated to developing and understanding the autonomous motion of catalytic micro- and nanomotors,[17] involving compositions and shapes of catalysts,[91, 92, 94] the design of micromotors [41, 76, 81, 98] and fuels to power them.[115, 116] However, up to date there was no report about effective autonomous motion of microjet engines, which can be orders of magnitude faster than state

of the art systems. Here, autonomous microjet engines are shown, their conditions and kimenatics are characterized.

4.2 Results and Discussions

Arrays of Ti/Cr/Pt and Ti/Fe/Au/Ag microjet engines were prepared on silicon substrates. Microjets were immersed in water containing surfactants and located in located in Petri dish. Microjets were released from surfaces using addition of hydrogen peroxide (high concentration: 30 % v/v droplet of H_2O_2) on top of the samples. Figure 4.1 A–C shows optical microscopy images (top) demonstrating the method of microjets activation and release from the surface. Figure 4.1 A–C shows schematic of this process. Alternatively microjets can be mechanically scratched from the surface, e.g. by plastic tweezers.
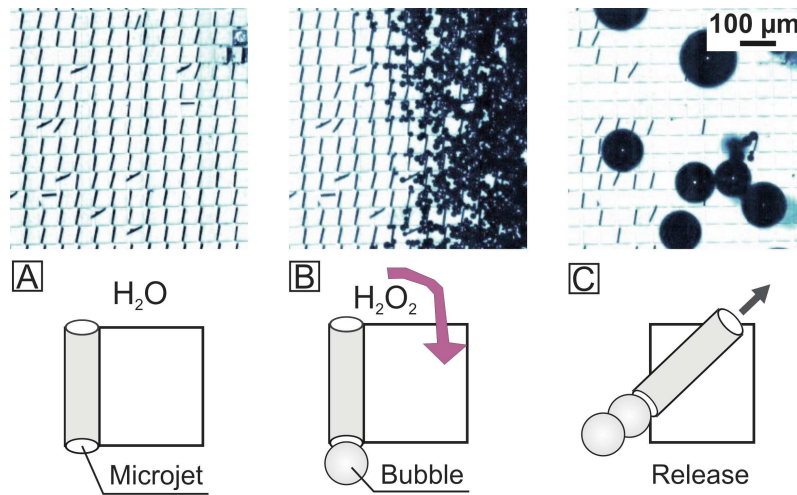
Figure 4.1: Microjet engines 'take off' from the silicon surface. (A) A static array of fabricated catalytic microengines, located in solution of water with surfactants, (B) a local addition of the 30 % v/v hydrogen peroxide fuel (gradient propagates from right to left) activates microengines, leading to their (C) release from the surface.
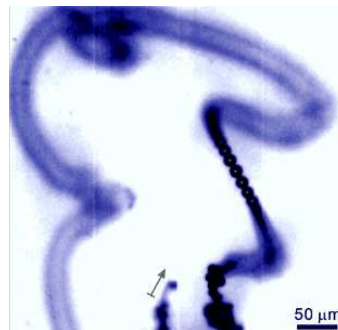
Figure 4.2: Optical image of individual moving microjet engine. Microengine location, length and the direction of movement is indicated by the arrow.

Figure 4.2 shows individual autonomous microjet, that self-propelled at the speed 85 $\mu m \cdot s^{-1}$ and left behind a long microbubble-tail. Figure 4.3 (i to iv) shows sequence of optical microscopy images of self-propelled microjet during 100 ms. The schematic insets of Figure 4.3 explains how the fuel pumps into the microjet (i), a bubble nucleates upon the decomposition of H_2O_2 in a contact with internal Pt catalyst (ii), the O_2 bubble starts to grow and moves to one tubular opening of the microjet (motion is indicated by the black arrow) (iii), and finally the bubble recoils from the microjet (iv). Both bubble migration (iii) and recoil (iv) induce microjet motion into the opposite direction with respect to moving/recoiling bubble.
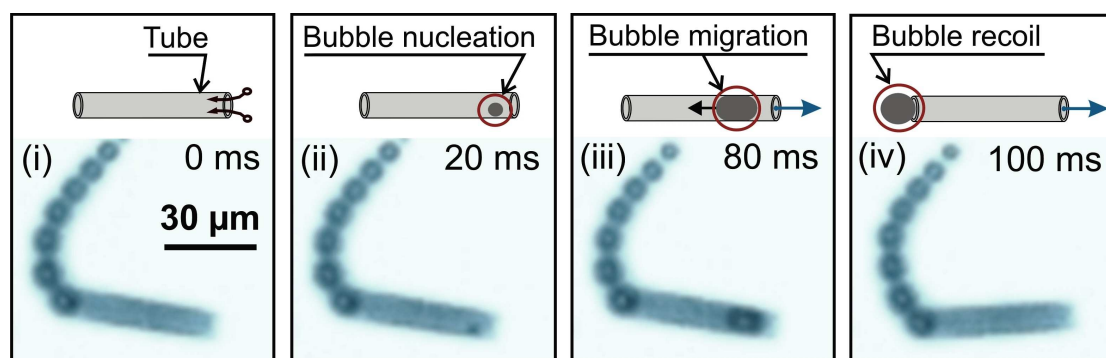
Figure 4.3: Propulsion mechanism of the microjet engine by the recoil of bubbles: i) at the beginning solution/fuel fills tubular microjet by capillary force, shown by arrows ii) H_2O_2 decomposition takes place in the microjet, followed by the nucleation of O_2 bubble, iii) growth and migration of the microbubble take place, it induces pumping of fluid and the motion of microjet, iv) the recoil of microbubble, that further propels the microjet.

4.2.1. Optimization of Surfactants for the Motion

An addition of surfactant is crucial for the motion of microengines, since it reduces surface tension of the fuel solution (for instance, 10 wt % aqueous solution of H_2O_2 equal 73 $mJ \cdot m^{-2}$). Influence of both concentrations of hydrogen peroxide and surfactant were studied and shown in Fig. 4.4. Although a common soap can be routinely used in experiments, here a study of Benzalkonium Chloride (BC) concentration is presented (adapted from ref. [21]). The inset in Figure 4.4 represents the average microjet speeds as a function of surfactant concentration using a constant concentration of 15 wt % of H_2O_2. Each data point was taken as an average speed of five self-propelled microjets. Figure 4.4 depicts the speed of the microjets at different fuel (hydrogen peroxide) concentrations using a constant concentration of 0.005 wt % of BC. The speed increased with hydrogen peroxide concentration up to 15 %, reaching a maximum speed of 275 $\mu m \cdot s^{-1}$ (5.5 body lengths per second), and it levelled-off at higher concentrations. The plot shows similar features to a traditional Langmuir ad-

sorption isotherm, which relates the adsorption of molecules on a solid surface to the concentration of the medium.[133]
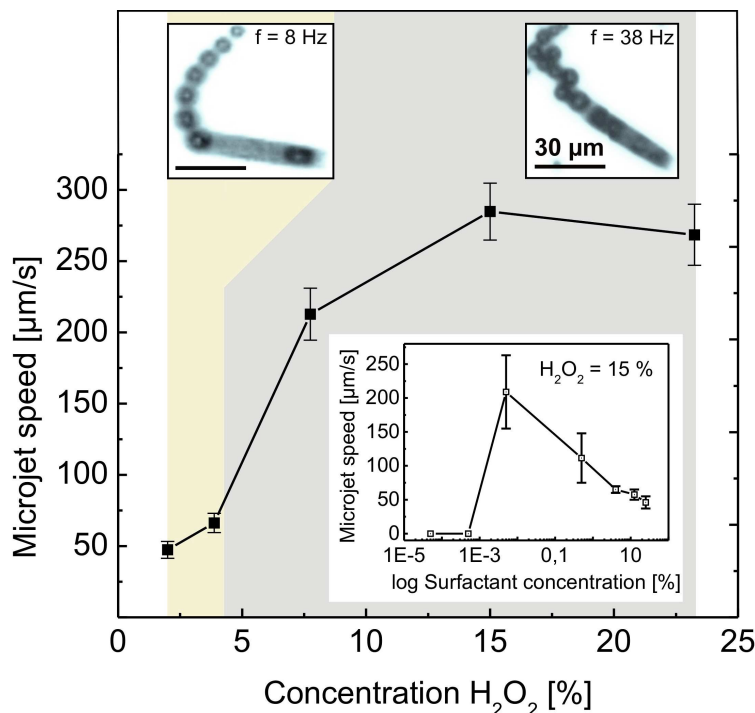
Figure 4.4: Speed of microtubes with different concentrations of hydrogen peroxide containing constant amount of surfactant (0.005 wt % BC) and 1 v/v % of isopropanol. The inset shows the speed of the microtubes with different concentrations of surfactant (5×10^{-5} to 20 %) at 15 wt % of H_2O_2.

It is hypothesized that the maximum speed is limited by i) the surface area of the Pt catalyst layer and ii) the intrinsic turnover rate of the catalyst at high analyte concentrations. The concentration in the range 0.005 - 0.5 wt % of BC was selected as the optimum for further experiments with microjets as it reduced the surface tension without inhibiting the catalytic reaction. For previously reported catalytic synthetic nanomotors their maximum speed was reached at different concentrations of H_2O_2: the bimetallic nanorods fabricated by Sen reached a maximum speed at 3.7 wt % of H_2O_2. Wang reported similar results using carbon nanotubes (CNTs)-modified nanomotors but their highest speed was reached at 15 wt % of H_2O_2.[91] Gibbs and Zhao observed maximum speeds of their microsphere-based motors at 2 wt % of H_2O_2.[82] In addition, we observed that there is a limited amount of space inside the microcavity at a high frequency of microbubbles generation (f = 38 Hz), that is at higher concentrations of hydrogen peroxide. At lower concentrations, the frequency of bubbles is lower (f = 8 Hz), resulting in a lower speed of the microjets. This observation supports microjets motion with respect to the fuel composition. These results reveal that a surfactant concentration beyond a certain threshold is required to

activate the motion of the microjets. However, the speed of the microjets is reduced by further increasing the surfactant concentration. Moreover, the surfactant can form micelles that occupy the chemically active sites of the Pt catalyst film and, therefore, the observed speed of microengines can be reduced at higher concentrations of surfactant.

4.2.2. Kinematics of Motion

Graph 4.5 A shows velocity of individual Ti/Fe/Au/Ag (here Ag catalyst is used instead of Pt, however application of Ag was found un-efficient due to rapid degradation) microjet engine with a length of 100 μm recorded during 2 seconds of motion. Black circles represent moments of time when microbubbles recoil. Between these intervals only Brownian motion (fluid diffusion) affects the displacement of the microjet (indicated as grey dots). One can see that due to relatively large size of the microjet (50 μm length) and high length/diameter ratio the Brownian diffusion is negligible in comparison to the direct propulsion of microjets.
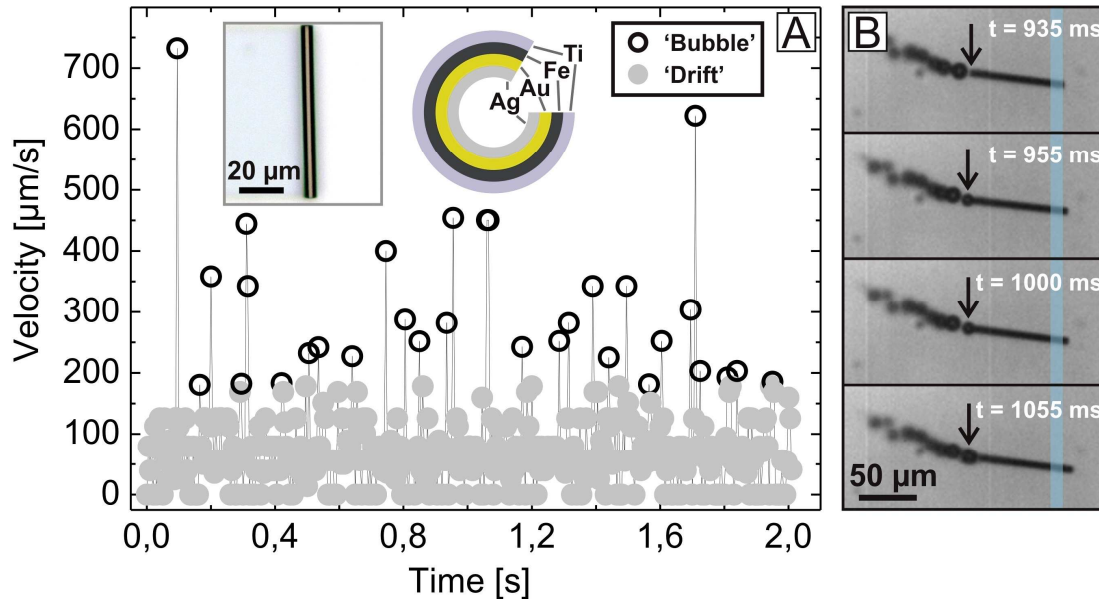
Figure 4.5: (A) Velocity of individual Ti/Fe/Au/Ag microjet engine during 2 seconds of motion. (B) Optical microscopy sequences of self-propelled microjet. Arrows show recoil of microbubbles.

Figure 4.5 A shows a clear stepwise motion of the microjet engine. Figure 4.5 B shows optical microscopy frames, indicating moments of time when microbubbles recoil. Additional (Fe) layer allowed an external remote control of the micromachine by magnetic field. It is not shown here (considered in Chapter 6). Fig. 4.6 illustrates how steps of microjets change with the bubble radius (error bars are calculated as

standard deviation of 20 microbubbles recoiled from individual microjets). It is clearly seen that the microjets do not drift, but immediately stopped by a high viscosity of fluids. The stepwise motion is deterministic and can be well approximated as a product of average size and frequency of bubbles.
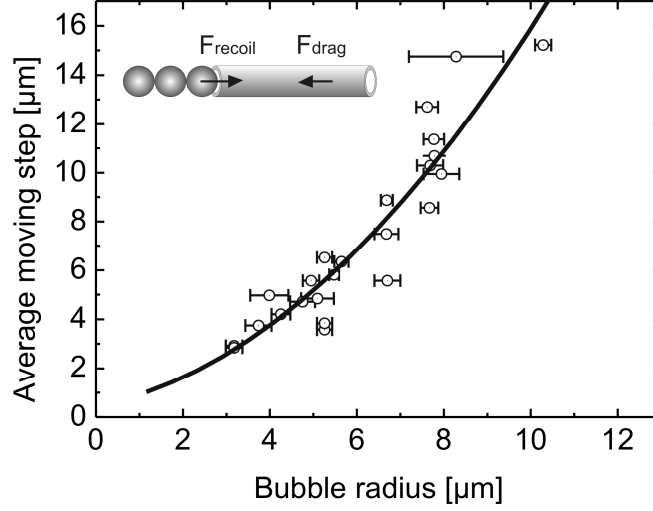
Figure 4.6: Experimental data of microjets' moving steps as a function of bubble radius. Inset sketch shows schematic of simplified forces acting on the microjet. Here, drag force of migrating/recoiled bubble is higher than the drag force of the tube. Acting forces were considered in details in Chapter 1.

For small radii of bubbles (less than 7 μm), the average moving step is almost equal to that of each bubble radius. However, when the bubble radius increases, the moving steps become larger than the bubble radius. It can be explained from the Stokes drag force F_{recoil} acting on the microbubble ($F_{drag–bubble}$), which becomes larger than the drag force F_{drag} acting on the microengine ($F_{drag–tube}$). When larger microbubbles are generated (larger than 7μm), longer moving steps were observed. It is important to note, in case of higher bubbles frequencies bubbles can form "bubble-tails" and collide with each other at the end of microjets. This collision of bubbles increases moving steps of microjets. By this, the stepwise motion of microengines mimics the stepwise motility of some pathogens, like *listeria*, which are self-propelled by actin polymerization. *Listeria* makes 4.5 nm long step, determined by the size of the actin.[134] Speeds of microjets can be determined by the multiplication of the bubbles average frequency and radius. Fig. 4.7 shows experimental data points of microjets' speed. Straight line represents a linear fit to experiment points. Deviations from the linear dependence are attributed to some propulsion cases of microjets when irregular recoil of bubbles is observed. In this case, the motion are ruled out by non- deterministic collisions of bubbles. Microjets which self-propelled in various trajectories and left different micro bubbles traces behind are well observed in Fig. 4.8.
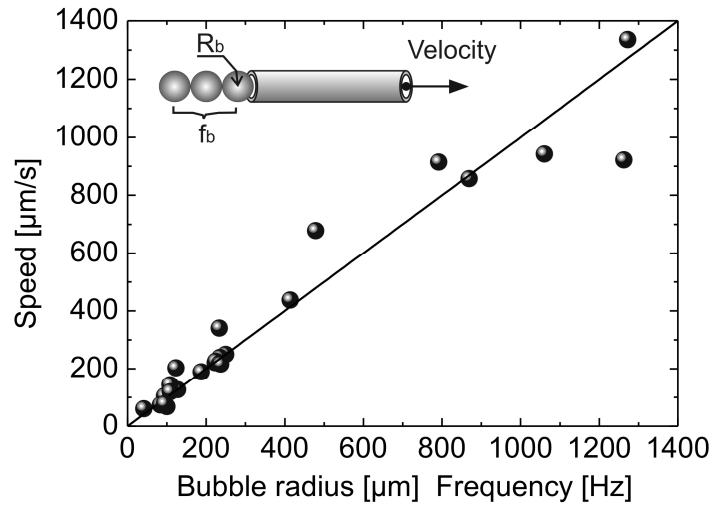
Figure 4.7: Microjets' speed as a function of microbubbles radius and frequency. Straight line represents a linear fit to experimental points.

Asymmetry of rolled-up tubes lead to straight, circular and helical trajectories of motion. Maximum recorded speed of microjets was 2 mm s^{-1} achieved at room temperature. It corresponds to 50 bl s^{-1}. Recently, our groups showed microjets acceleration up to 200 bl s^{-1} at physiological temperature.[48]

4.2.3. Trajectories of Motion

Figure 4.8 shows trajectories of autonomous motion of Ti/Cr/Pt microjets, indicating schematic (on the left side) and optical microscopy images (on the right side). Fig. 4.8 A demonstrates straight motion. The motive force of microjets is indicated by red arrow, that is parallel to the long axis of tubular symmetry. Observations show that microjets, which move in straight can have single or multiple "microbubble tails". Fig. 4.8 B indicates circular or orbital type of motion. This motion can be explained by considering torque. Magnitude of torque equals the multiplication of the magnitude of the driving force, the length of the level arm (distance between center of rotation and the force applied) and the angle between the force vector and the level arm. Particularly, one can see from Fig. 4.8 B that circles of motion can be smaller, it is due to the larger torque acting on microjets. Furthermore, it is postulated that such two-dimensional circular motion can be possible due to confinement of microjets at the air-liquid interface. Fig. 4.8 C shows clock-like motion of microjets, in this case microjets move clockwise or counter-clockwise and their level arms are equal to the lengths of microjets. Fig. 4.8 D shows 3-d helical motion. Here, in addition to the 2-d torque the other torque is added, which rotates microjets. It is proposed that these trajectories are due to unique combination of bubble recoil and fluid pumping into mouth of microjets. Investigation of trajectories is the subject of future studies.
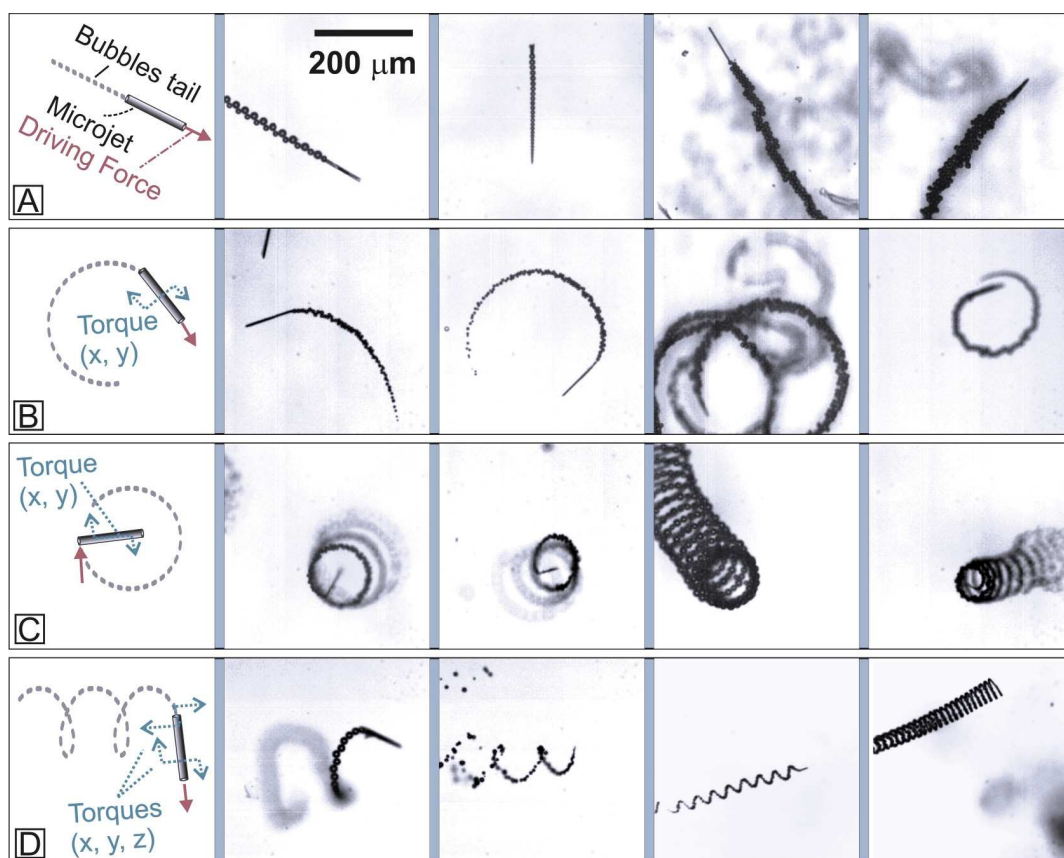
Figure 4.8:   Autonomous movements of microjets in different trajectories: (A) straight, (B) circular, (C) clock-like, D) three-dimensional helical. Schematics on the left indicate driving forces and torques acting on microjets.

4.3 Summary

A generic approach to release tubular microjets into solution was developed. Analysis of their motion showed that microbubbles nucleate, grow and recoil in catalytic microtubes. Concentrations of surfactant and hydrogen peroxide were optimized to achieve higher speeds. Bubble recoil leads to the determenistic stepwise motion where microjets speeds can be approximated by the multiplication of frequencies and average radiuses of bubbles. High speeds of self-propelled microjets as high as 2.1 mm·s^{-1} (50 body length per second) are reported at room temperature. It leads to more powerful micromachines in comparison to state-of-the-art catalytic micromotors. Microjets self-propel in different trajectories can be divided mainly into straight, circular and 3-d helical motions. Different trajectories observed experimentally might originate from assymetry in the rolled-up layers, that forms tubes with reach parameters. In future specific trajectories can be potentially "programmed" by the proper design of geometry of rolled-up microjets. For instance, when triangular nanomembranes are used, it is expected to have only circular type of motions. Once, the shape of parallelogram is used one may observe helical type of motion.

5 Autonomous Motion of Biocatalytic Micro-Jet Engines

Biocatalytic Ti/Au/(SAM)/Catalase microjet engines, which contain catalase enzymes as catalysts, self-propel in the solution of hydrogen peroxide.[41] Catalase enzyme was covalently bound to Au in the cavity of rolled-up Ti/Au microtubes, shown in Scheme 5.1. The high efficiency of these hybrid microengines allowed them to move at a lower concentration of the hydrogen peroxide fuel in comparison to platinum based microjets. Furthermore, the dynamics of hybrid microengines interacting with bubbles is considered (parts of this Chapter were adapted from ref. [41], scheme of biocatalyst immobilization and experiments were done in collaboration with Dr. S. Sanchez).
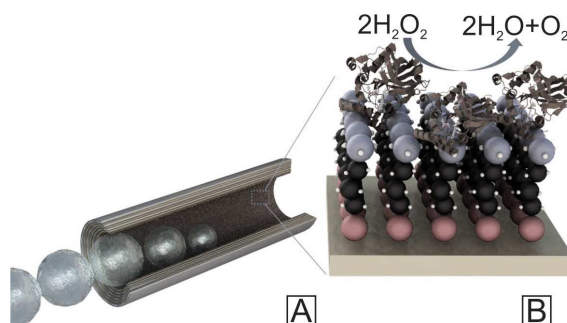
Scheme 5.1: Scheme showing the cross section of biocatalytic microjet. (A) Open view of the microengine, (B) surface modification of the inner Au layer with enzyme.

5.1 Introduction

Catalase is a common enzyme found in nearly all living organisms. Catalase has the function to decompose hydrogen peroxide into water and oxygen.[135] Hybrid micromachines, which couple catalytic biomolecules such as enzymes and artificial nano/microdevices, are a promising alternative to the first generation of catalytic microjets with Pt metal as a catalyst towards the finding of higher efficiency conversion, versatile configurations, more physiological conditions and biocompatible fuels. Only a few hybrid nanomotors were reported where mainly biosystems were employed to perform tasks [136, 137]. More recently, the use of enzymes for locomotion was used by Mano and Heller to propel a carbon fiber (cm scale) at the air-glucose interface.[115] Feringa reported the covalent attachment of enzymes to multiwalled carbon nanotubes (MWCNTs) propelled by a bubble generation,[116] but their trajectory was strongly affected by both the Brownian diffusion and the uncontrolled position of the enzymes on the MWCNTs. Sen and Mallouk [87] reported en-

zyme-Au/polypyrrole nanorods. However, only Brownian motion was observed for this nanomotors and no further investigations have been performed. Herein, the efficient locomotion of biocatalytic microjet engines is shown.

5.2 Results and Discussions

Scheme 5.1 A shows an open view of Ti/Au microtube where the inner Au layer was functionalized with a SAM of 3-MPA (Scheme 5.1 B). The carboxylic terminal groups of the SAMs were converted to amine-reactive esters by the coupling agents 1-Ethyl-3-[3-dimethylaminopropyl]carbodiimide hydrochloride (EDC) and N-hydroxylsulfo-succinimide (Sulfo-NHS) to covalently bind the protein (i.e. catalase) via carbodiimide reaction. The hybrid microtubes (Ti/Au-SAM-catalase) showed autonomous motion when immersed in peroxide solution, due to the highly active enzyme that decomposes peroxide into water and molecular oxygen; which, in turn, propels the microengine.

In a representative example, Figure 5.1 shows the tracking trajectories of physically adsorbed Ti/Au-catalase (Fig. 5.1 A) and covalently modified Ti/Au-SAM-catalase microengines (Fig. 5.1 B) during a period of 12 s in 1.5 wt % H_2O_2. A dramatic increase in the mobility of the hybrid microengines was observed for those functionalized with thiol groups (Fig. 5.1 B), where the continuous thrust of bubbles exerts a force which propels the microjet at an average speed of 226.1 ± 21.1 $\mu m \cdot s^{-1}$ for n = 7 data points.
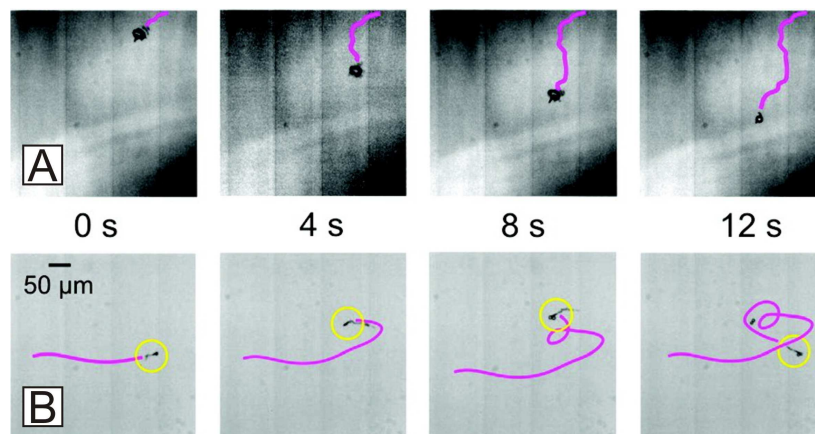
Figure 5.1: Tracking trajectories of a 25 μm long Ti/Au hybrid microengine with (A) physically adsorbed catalase (B) and Thiol-Catalase in 1.5 % H_2O_2.

In contrast, the catalase-adsorbed microengines move at speeds of 40 $\mu m \cdot s^{-1}$ halting shortly after their activation (approximately 1 minute). Additional control experiments, performed with Ti/Au microjets in the same fuel conditions resulted into static microjets. Thus, this evidence clearly indicates that the generation of oxygen

bubbles into the microjets arises from the biochemical decomposition of the peroxide by the enzyme catalyst. Contact angle measurements confirmed the gold-thiol bond given that the contact angles changed from 73.3 ± 3.2 to 53.2 ± 1.3 degrees when a volume of 0.75 μL of H_2O was dropped onto Ti/Au and Ti/Au-SAM surfaces respectively (several measurements were done for statistics, n = 6). The samples became even more hydrophilic after incubating the Ti/Au-Thiol sample with catalase, denoted by the decrease in the contact angle to 24.3 ± 2.4 degrees (n = 6). These results prove the successive functionalization and therefore the coupling of the enzyme to the Au surface.

5.2.1. Quantification of the Speed and Angle of Rotation

Bubbles forming at the mouth of the microengines, i.e. front-side bubbles, are observed for the enzyme-modified microengines. The dynamics of the biocatalytic microengines is influenced by the variable viscous drag force exerted by the front-side bubbles which creates a torque and leads to turns and circles.

Figure 5.2 shows dynamic steering and full rotation of a Ti/Au-Thiol-catalase microengine by the generation of front side bubbles. Similarly, the angle of rotation is reduced inducing a dramatic change of direction providing an autonomous steering mechanism. Figure 5.2 shows a full rotation of a 25 μm long microjet during a period of 3.5 seconds while creating and releasing two consecutive front-side bubbles. The bubbles emerged during the first 0.5 seconds and they moved to the left side of the microengine.
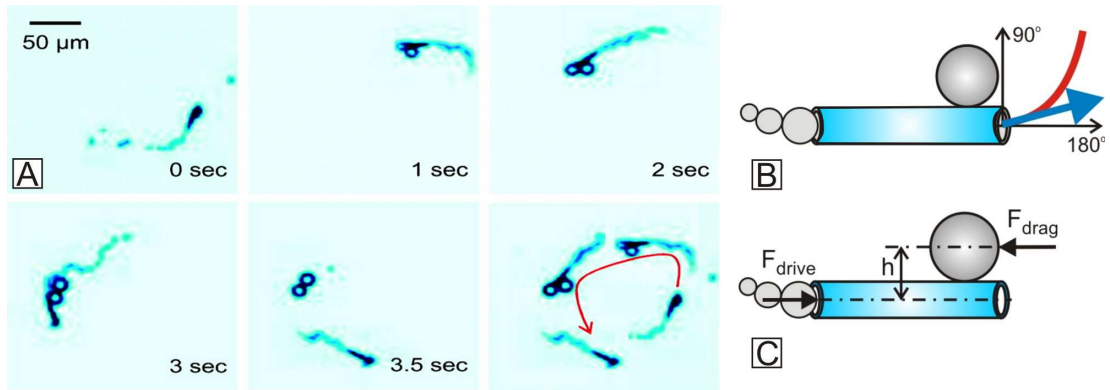
Figure 5.2: (A) Optical microscopy sequences, stochastic change of the motion due to interaction with microbubbles. (B) Schematic of variable friction control by the attached microbubble. Here blue arrow indicates the direction of motion and red line simulates the curve trajectory of the microengines. (C) Competition of forces involved in the motion and rotation of the hybrid microengines is illustrated. Here *h* is the distance between the long axis of symmetry of microtubes and the geometrical centre of the front-side-bubble (level arm). This distance is important for microjet rotation due to appearance of torque.

Immediately after, the microtube starts to change its direction and thus rotates counter-clockwise (CCW) as well as reducing its velocity. While rotating, the oxygen bubbles are continuously growing and thereafter 2.5 s they detach. After being freed from the extra drag force exerted by the bubbles, the microjet experiences a dramatic acceleration (Figs. 5.2 – 5.3). Therefore, the analysis of the motion regarding the size of the front-side bubbles is crucial for understanding the autonomous steering of hybrid microjets. Two different parameters were measured to show that the radius of the front-side bubble is a crucial parameter on the dynamics of the microengines. The first parameter is the angle of rotation, defined between the direction that a microengine was pointing just before and after releasing the front-side bubble. When the value is 180º means no change on the direction of motion, whereas 120º indicates an abrupt change in direction (Figure 5.2 B). The second parameter, speed, is calculated as the displacement of the microengine over a 0.2 s interval when pushing microbubbles from 3 to 15 µm of diameter.

In the present study, the speed diminished linearly with increasing bubble diameter. The microengine experiences an average speed of $226.1 \pm 21.1 \mu m \cdot s^{-1}$ (for n = 7) data points when it is free of front-side bubbles. The microengine pushing small bubbles, e.g. 3 µm of diameter, does not change significantly its direction and likewise its speed is only slightly reduced. Therefore, the generation of bubbles from the front side with diameter equal or smaller than the microtube diameter, does not alter the motility mode of the microengine. In contrast, when the bubble released from the front side is larger than the diameter of microtube, e.g. from 4 to 12 µm of diameter, the speed decreases linearly. The angle of rotation is also reduced inducing a striking change of direction.

Figure 5.2 C depicts the competition between the driving and the drag forces caused by the front-side-bubble. Torque depends on lever arm and on the forces involved in the motion. Large distance between the long axis of symmetry of the tube and the geometrical center of the bubble (large lever arm) produces a small radius of torque. However, bubbles with diameter larger than 10 µm, do not provoke a higher rotation angle so the radius of the torque is also limited by size itself of the front-side-bubble. The drag force depends linearly on velocity at low Reynolds numbers and is calculated using Stokes drag formula (considered in Chapter 1). The Stokes drag force calculated for bubbles from 4 to 15 µm diameter gives a force $16.44 \pm 0.75 pN$ (n = 7). Figure 5.3 shows the velocity of a 50 µm long hybrid microengine with the time while releasing a bubble of 10 µm diameter from the front edge of the tube. Each data point represents the speed in intervals of 0.5 s taken from sequences of 10 frames. The microengine reaches a minimum speed of $38.2 \ \mu m \cdot s^{-1}$ while pushing oxygen bubble and it acquires a maximum speed of $167.4 \ \mu m \cdot s^{-1}$ when free of bubble. The increase on the drag force exerted by the front-side bubble makes the microengine to reduce its velocity while the bubble is growing.
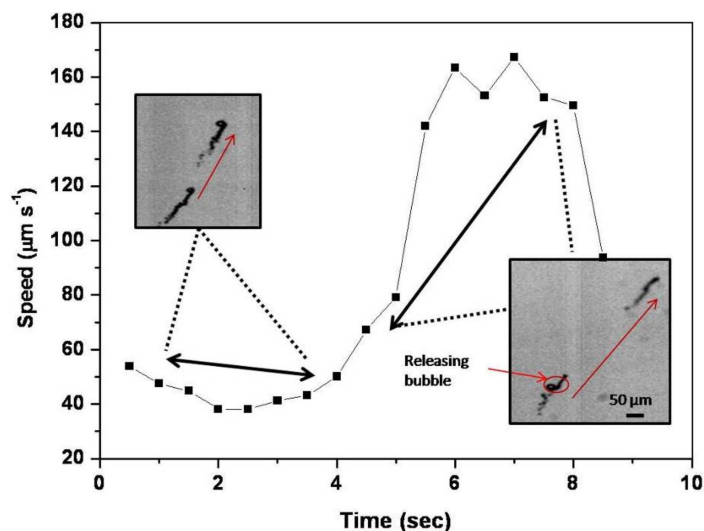
Figure 5.3: Variation of the speed of a 50 µm long Ti/Au-SAM-Catalase microengine during 10 seconds in the presence of 1.5 wt. % hydrogen peroxide fuel and 0.02 % SDS. Insets show superimposed optical images of Ti/Au-SAM-Catalase microengine for a period of 2.6 s in both cases.
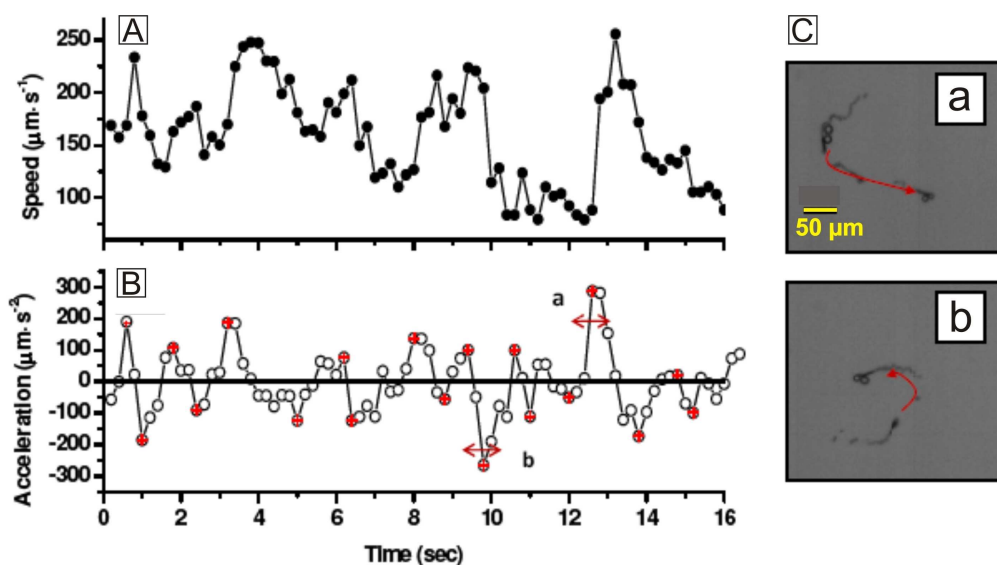
Figure 5.4: (A) Speed and (B) acceleration of a 25 µm long Ti/Au-SAM-Catalase microengine over 16 seconds. (C) Superimposed optical images of the same microengine in two different situations: a) releasing a bubble, accelerating upon new front-side bubble is growing and thus the speed decreases; b) growing of new bubble and decelerating at same time as the microengine rotates because front-side bubble moves to the side wall of the tube.

When the bubble migrates to the back edge through the wall of the tube, the microengine slightly increases its velocity. Finally, a dramatic acceleration is observed, changing its speed from 69 to 167 $\mu m \cdot s^{-1}$ when it is completely detached. These deceleration/acceleration cycles are continuously repeated and because of that,

the speed decreases again after 8 s. The change on the speed and the acceleration was studied for a 25 μm long hybrid microengine during 16 s of recorded video (Fig. 5.4 A-C). Fig 5.4 A plots the speed of microengine every 0.2 s interval. The speed decreases both when bubbles are growing from the front-side and when the microengine turns. It can be observed in Fig. 5.4 A peaks of maximum velocities corresponding to microengines free of front side bubble. Thereafter, a generation of new front-side-bubbles makes the speed to decrease upon a minimum speed, when the bubble is released. Immediately after releasing, the speed increases reaching also a maximum acceleration typically after ca. 0.6 s as shown in Fig. 5.4 B.

Two sequences are chosen as example of the variable dynamics of the microengines, specifically the rotation and acceleration. The superimposed optical images of periods about 0.6 s are shown in Fig. 5.4 C (a, b) corresponding to the regions *a* and *b* in Fig. 5.4 B. Whithin the interval *a,* the microengine releases two consecutive front-side bubbles and thereafter experiences a dramatic acceleration as plotted in Fig. 5.4 A and Fig. 5.4 B. Shortly after, a new bubble increases the drag force and thus, the speed starts to be reduced again. Moreover, a rotation of the microengine was observed and further quantification will be discussed in next section. In the interval *b*, the microengine was initially free of front-side-bubble and while generating a new one, it rotates counter clock-wise as well as diminishing its speed.
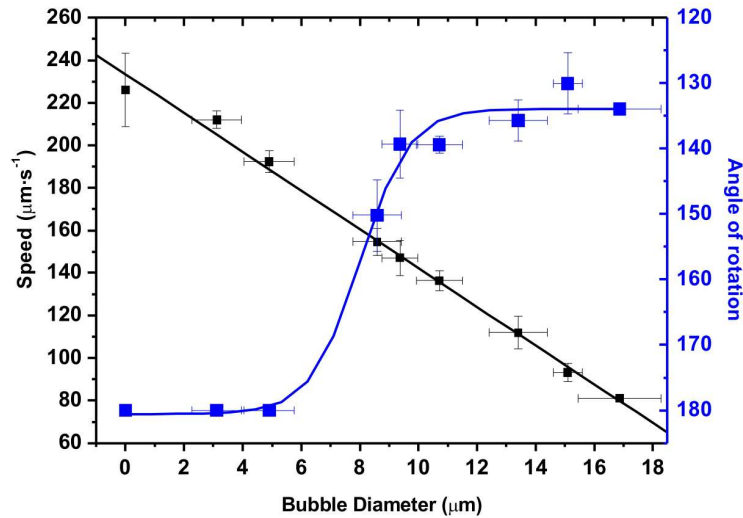
Figure 5.5: Influence of the bubble diameter of the front-side bubble on the speed and the rotation angle of Ti/Au-SAM-Catalase microjets. The error bars represent the standard deviation.

Figure 5.5 plots the quantitative analysis of the angle of rotation (50 μm long microjet) and speed with the diameter of the front-side bubble. Briefly, when releasing small front-side bubbles, i.e. 3 μm in diameter, the microengines do not change significantly their direction and likewise their speed is only slightly reduced. This scenario can be reproduced by adding small amounts of common soap (*Fit Gmbh*) to

the fuel solution. In contrast, when these front-side bubbles are larger than the diameter of microtubes (i.e. from 4 to 12 of diameter) the speed decreases linearly following the Stokes law. The hybrid microengines exhibit a force of 16.44 ± 0.75 pN, which is 4 times higher than found for 50 μm long Pt based microengines, indicating that larger cargo particles could be transported by these hybrid microengines.

5.2.2. Dynamics altered by Front Side Bubbles

Figure 5.6 (A-D) shows the optical images of a hybrid microengine releasing small front-side-bubbles during a period of 3 seconds. The Ti/Au-SAM-catalase microengine was immersed in a 1.5 wt % H_2O_2 fuel and 0.02 % SDS surfactant as in all previous experiments. However, in this experiment small amounts of common soap (*Fit Gmbh*) were added to the fuel solution in order to reduce the surface tension and consequently the radius of all the released bubbles (front and back side). This change in the surface tension leads to such small bubbles that neither the speed of the microengines nor the direction of motion is affected by the size of those front-side-bubbles as observed from the blue arrows in Figure 5.6.
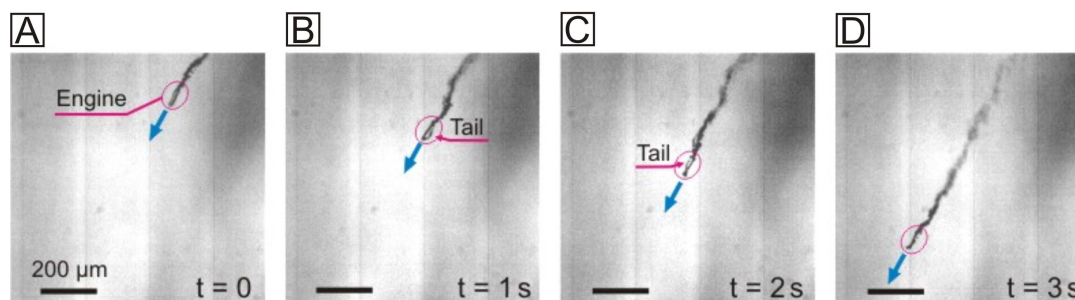
Figure 5.6: Straight motion of hybrid microengine in 1.5 % H_2O_2 fuel solution containing common soap. Blue arrow indicates the direction of motion and pink arrows point the "tail" from the small front-side bubbles.

5.3 Summary

A novel hybrid biocatalytic microjet engine was designed based on enzyme catalase. An inner layer of microtubes was functionalized by biocatalyst. Catalase can convert millions of molecules of hydrogen peroxide to water and oxygen each second. This novel approach leads to faster, more powerful and efficient engines compared to those based on a Pt catalyst as well as the use of lower concentration of hydrogen peroxide fuel. At concentration 1.5 wt % H_2O_2 the hybrid microengines move at 10 bl·s^{-1} compared with 1 bl·s^{-1} from the Pt based-microengines.[23] However, important to note that due to degradation of enzymes the Pt based microjets can work during longer time than biocatalytic microjets. These hybrid biocatalytic microengines can pave the way to other chemical configurations to induce motion and to-

wards the finding of biocompatible fuels. Such specific functionalization of the inner layer of microtubes with molecules can lead to other configurations to generate motion from different chemical energy sources. Coupling glucose oxidize in the same system with catalase would allow transforming of glucose fuel into motion. However, for real biomedical applications the reaction products of a possible glucose-powered micromachine must be removed or consumed by an organism. In any case, the ultimate goal is the development of very efficient micro- and nanomachines with efficiency close to biological motors. On the other hand, if micromachines can be powered and controlled by external fields, a fuel-free propulsion can be achieved..

6 Magnetic Control of Microjet Engines and the Delivery of Cargo

The motion of Ti/Fe/Pt microengines can be controlled by external magnetic field to load, transport and deliver cargo-microobjects in solution. Since ferromagnetic (Fe) layer is integrated into the body of microjets external magnetic field is used to control the directionality of microjet engines motion or even confine them into dynamic circular "micro-docks". Conceptually, a microfactory is realized, where microjets can capture, transport and deliver particles, thin solid films and biological cells, shown in Scheme 6.1. When injected into microfluidic channels microengines are able to move and carry microcargo, along and against flowing fluidic streams. It shows a potential of being integrated with versatile Lab-on-a-Chip systems (parts of this Chapter were adapted from refs. [23, 24, 42]).
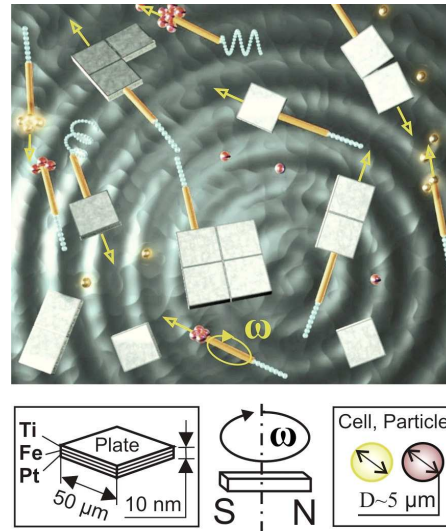
Scheme 6.1: Schematic of microfactory, where micro-cargo is transported, assembled and delivered into desired locations using remote controlled microjet engines.

6.1 Introduction

Man-made factories use macroscale machines for the transportation and assembly line production. It is of interest to miniaturize factories, where new products can be fabricated or synthesized at lower cost.[138] Even at lower scale, main inspiration of nanofactory comes from biology. A working instrument of "biological nanofactories" is the ribosome, consisting of ribosomal RNA (rRNA) and protein machines. Together they read messenger RNAs and translate the encoded information to a protein machine.[7] It is not known how to make a similar synthetic nanofactory and the de-

sirable first step consists in the controllable transportation and assembly of cargo objects. Sen's and Wang's groups demonstrated remote control of catalytic electrophoretic nanomotors.[22] These nanomotors were used to transport cargo particles. Former advances of these nanomotors were handicapped by two drawbacks, i) extra functionality was required either to the nanomotor or to the cargo (e.g. magnetic or electrostatic interactions, chemical modification) [15, 139, 140], or ii) low power micromachines could load only one particle at time.[140] However, practical applications require higher towing forces and simple mechanisms to bind and un-bind different types of cargo in a controllable way. To date, the realization of these tasks was not known. Here, effective and remotely controlled microjet engines are used for the transportation, delivery and assembly of multiple inorganic and organic cargo microobjects. Easy mechanisms of binding and release of cargo by pumping/capillary force is shown.[23, 24, 42]

6.2 Results and Discussions

Figure 6.1 shows the remote controlled rolled-up Ti/Fe/Pt microjets by external magnetic field (a permanent NdFeB magnet located underneath of microjets is used). External magnetic field is used to turn or rotate individual catalytic microjet, as shown in optical microscopy sequences of Figure 6.1 A.
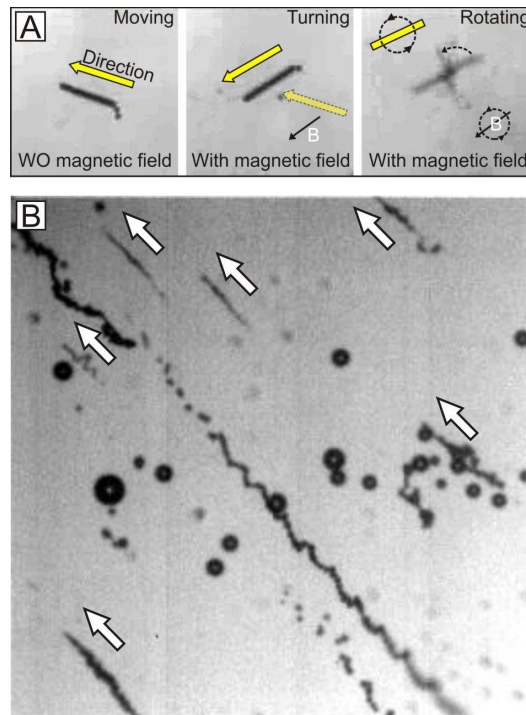
Figure 6.1: Magnetic control of 50 μm long catalytic microjets using external magnetic field. (A) Changing the directionality of motion and rotation of individual microjet (directionality of motion is indicated by yellow arrows). (B) Alignment of several microjets along external magnetic field. Window width is equal 420 μm.

Figure 6.1 A, left-side image, shows catalytic microjet moving in straight without magnetic field. When a static magnetic field is applied, moving microjet changes its direction (Fig. 6.1 A, middle-side image), and rotates when a rotating magnetic field is applied (Fig. 6.1 A, right-side image). Figure 6.1 B shows several self-propelled microjets, which move in straight trajectories. Interestingly, even microjets which moved in circular or helical trajectories without magnetic field, turned into straight motion in magnetic field. When rotational magnetic field is applied (using magnetic stirring plate), microjets start localizing in circular trajectories, i.e. dynamic "micro-docks". Figure 6.2 A, black curve, shows fit to experimental points of how the localization radius of microjets depends on the rotating frequency of magnetic field at constant linear velocity 305 µm·s⁻¹. The highest sensitivity of localization radius was found at a lower frequency of rotational magnetic field. Fig. 6.2 A, blue line, shows experimental points how the localization radius changes with increased linear velocity of microjets at constant frequency of rotational magnetic field, $f(B) = 0.3$ Hz.
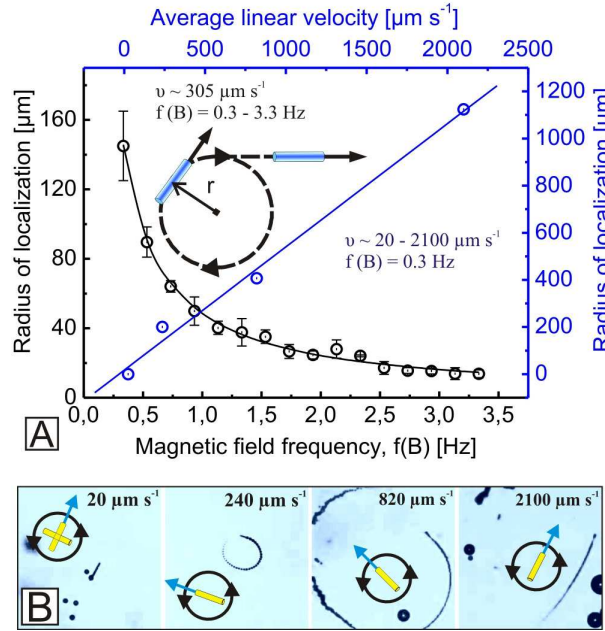
Figure 6.2: Confinement of self-propelled microjets into circular trajectories using external rotational magnetic field. (A) Localization radius as a function of magnetic field frequency at the constant linear velocity (black curve is exponential fit) and a dependence of localization radius on the mean linear velocity at constant rotational magnetic field (blue line is linear fit). (B) Optical microscopy images of different microjets moving at different linear velocities but located in the same frequency of magnetic field, i.e. linear speeds are written on top of individual images. Yellow drawings with attached blue arrows show schematic of micro-jets and the directions of their velocity vectors. Round black circles illustrates the direction of rotational magnetic field.

According to kinematic equation, localization radius can be described as a function of the linear velocity and frequency of rotation $r = \upsilon/(2\pi f_B)$, where υ is the

linear velocity of microjet and f_B the frequency of body rotation. Using average value of linear velocity (305 μm·s^{-1}) and substituting values of magnetic field frequencies in the range of 0.3–3.3 Hz, the equation is plotted (black curve) in Fig. 5.2 A. It illustrates that frequency of magnetic field is synchronized with the rotation of microjet. According to these results, the localization radius has a linear dependence on the velocity. However, at higher frequencies of magnetic field microjets start hitting their own tails, it leads to fluctuations of the linear and angular velocities. Subsequently, tunable "micro-docks" of microjets can be achieved which are well controlled by external magnetic field.

6.2.1. Remote Delivery and Assembly of Cargo

Magnetic control of self-propelled catalytic Ti/Fe/Pt microtubes is used to perform selective loading of multiple particles by microengines. Suspended polystyrene microparticles (5 μm in diameter) were dispersed in a fluid and moved by Brownian diffusion. The poles of the magnet were slowly moved into the desired direction to perform a specific task (rotation should be slower than around 1 rev s^{-1}). Once the magnet (and the tube) is turned at an angular speed larger than one revolution per second the particles are delivered. Cargo loading works in the following way, the suction of the fluid into the tubular microjets induces inward fluid motion which streamlines near the entrance of the tubes, dominating over the Brownian diffusion of the particles. Therefore, when the particles are located close enough to the microjets, they remain absorbed at the entrance of the tubes. The suction is inhibited and that allows the Brownian diffusion of the particles away from the tube to take effect so that the particle is not tightly locked. This movement, in turn allows more fuel to enter the tube restarting the pumping. This process repeats in a cyclic behaviour.

Figure 6.3 A shows a sequence of optical microscope images of the microjet transporting (i) 3, (ii) 27, (iii) 44, and (iv) 58 polystyrene particles. Figure 6.3 B presents a quantitative study of the microjet speed as a function of the number of loaded particles in 5 % v/v peroxide solution. As expected, there is a decrease of the speed from 80 to 18 μm·s^{-1} due to the increased drag force, when a larger number of microparticles are absorbed. The drag force of a single microparticle depends linearly on velocity at low Reynolds numbers and is calculated using Stokes drag formula. The Stokes drag force for one particle moving at a velocity 80 μm·s^{-1} is calculated to be 3.77 pN, and a transport of up to 60 particles was achieved. Gibbs and Zhao measured a driving force of Si/Pt microsphere-based motor equal to 0.07 pN.[141] It is remarkable that the microjet loading such a large number of particles can overcome the high viscosity of fluid at low Reynolds number. Different types of cargo can be delivered by the directed transportation, assembly and reorganization of Ti/Fe/Pt nanoplates (25 nm thick and 50 μm wide) at the air-liquid interface.
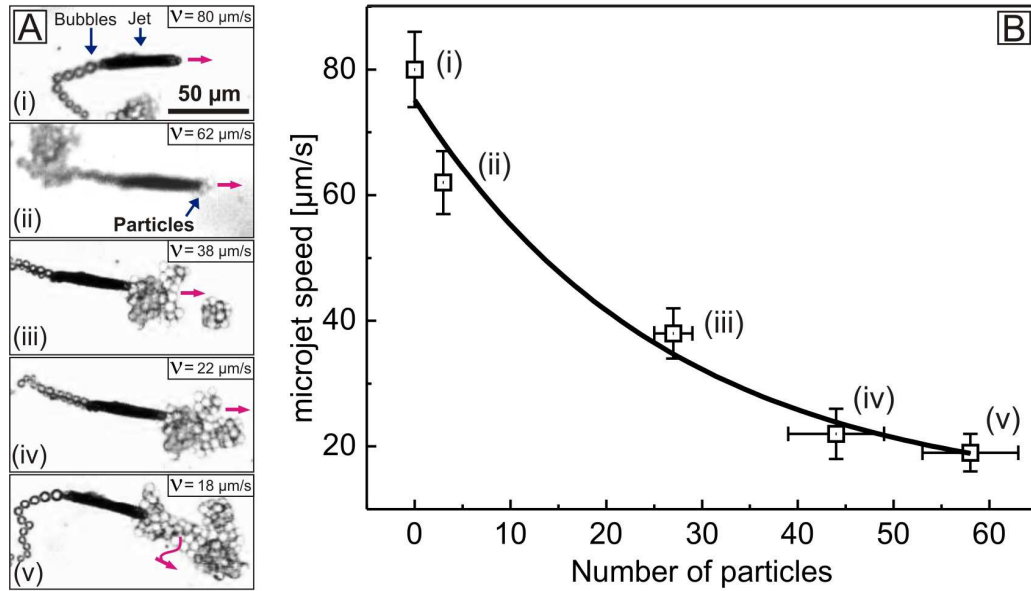
Figure 6.3: Transportation and delivery of polystyrene microparticles of 5 μm diameter. (A) Optical microscopy images of individual microjet loading and transporting i) 3, ii) 27, iii) 44, and iv) around 58 microparticles. The insets show an average speed of the microjet. (B) Plot shows the speed of the microjet depending on the number of loaded microparticles. The red arrow bar shows the direction of microjet motion with particles. Fuel solution used: hydrogen peroxide (5 % v/v) and 0.005 % BC, 1 % v/v isopropanol.
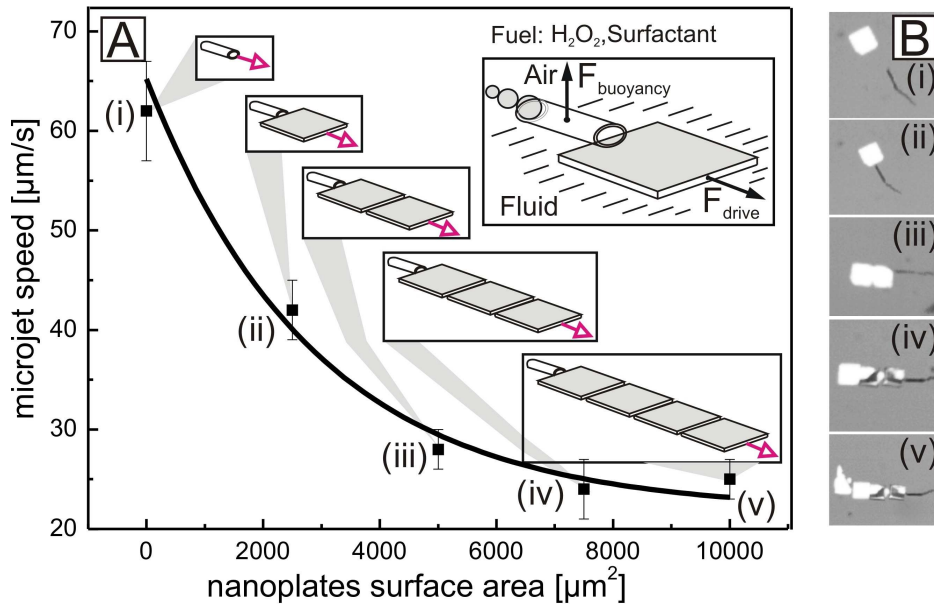
Figure 6.4: Remote assembly of metallic thin films, i.e. "nanoplates", in a raw by microjets. (A) A number of plates, i.e. surface area of transported nanoplates influences the microjet speed. The insets show schematic of the microjet moving one nanoplates and acting forces, schematic of the transportation of several plates. (B) Optical microscopy images of individual microjet which carried nanoplates, images correspond to experimental points (i–v) in (A). The fuel solution: hydrogen peroxide (5 % v/v), 0.005% surfactant and 1 v/v % of isopropanol.

Plot in Figure 6.4 A shows self-propelled microjet engine transporting from 1 to 4 nanoplates (i-v). Thin Ti/Fe/Pt plates are anchored at the air-liquid interface because of their hydrophobic properties. The microjet is filled with oxygen gas that also moves it to the air-liquid interface (schematically shown as inset in Fig. 6.4 A) due to the buoyancy force. The nanoplates contain ferromagnetic (Fe) layers for an easy alignment towards the moving microjets, i.e., the magnetic field causes rotation but not a linear displacement of the nanoplates. Once a single nanoplate was captured, the microjet was directed to other nanoplates until the loading of four consecutive objects was achieved. An inverse exponential behaviour of the speed was observed as the surface area of the transported plates' increases. Figure 6.4 B shows optical images of the microjet loading, transporting and assembling nanoplates, which corresponds to the experimental points (i-v) in Fig. 6.4 A.

Different assembly of nanoplates were accomplished by the remote microjets, illustrated in Figure 6.5 (A-F). After loading of 3 consecutive objects (Fig. 6.5 A-C), the microjet was turned so that the nanoplates could change their configuration (Fig. 6.5 D). Figure 6.5 F shows four nanoplates assuming a square shape. It indicates remote assembly of microscale cargo into desired configurations.
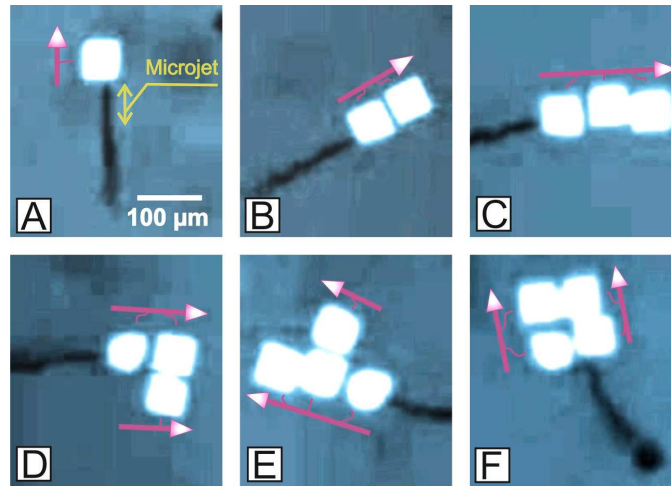
Figure 6.5: Optical microscopy images of the remote controlled microjet that transported and assembled nanoplates into different configurations (A-F). Fuel solution: hydrogen peroxide (5 % v/v), 0.005% BC and 1v/v % isopropanol.

6.2.2. Delivery of Multiple Mammalian Cells

Multiple neuronal CAD cells (Cathecolaminergic cell line from the central nervous system) were loaded, transported and delivered by the catalytic microjets.[24] The described methodology of micromachine enabled task was followed by the group of Wang to isolate and capture cancer cells using microjets.[29] Fig. 6.6 A shows SEM and optical (Fig. 6.6 B) images of individual fabricated microjet with absorbed CAD cell (CAD cell was located near the microtube after supercritical drying). Details of

CAD culture preparation are provided in the *Appendix*. Experiments were done in the following way. The microengines were directed towards the suspended cells (Fig. 6.7 A), where cells were loaded and delivered (Fig. 6.7 B-C) into the desired location. In the optical sequences, shown in Fig. 6.7, the microjet moves along pushing the cells over a period of about 9 s and after releasing them it can return to re-load new cells. A long working time of catalytic microjets allows their operation for several hours.
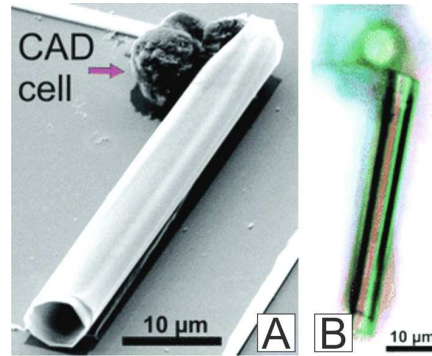
Figure 6.6: Microjet with CAD cells. (A) SEM and (B) optical images of Ti/Fe/Pt microjet with one individual cell.
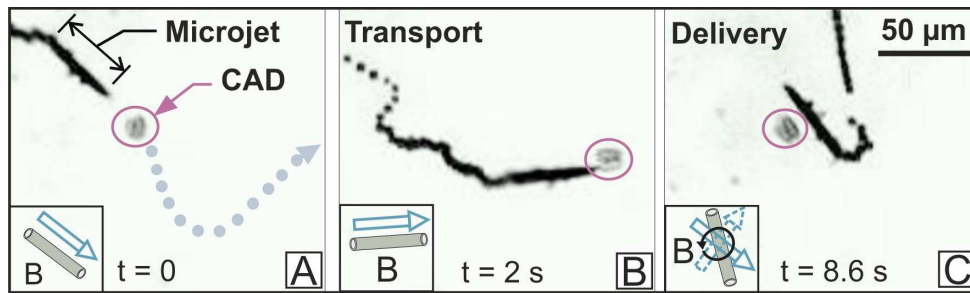
Figure 6.7: Remote controlled microjet loading, transporting and delivering CAD cells in the solution of hydrogen peroxide. By a rapid turning of the magnet the cells can be delivered into desired place.
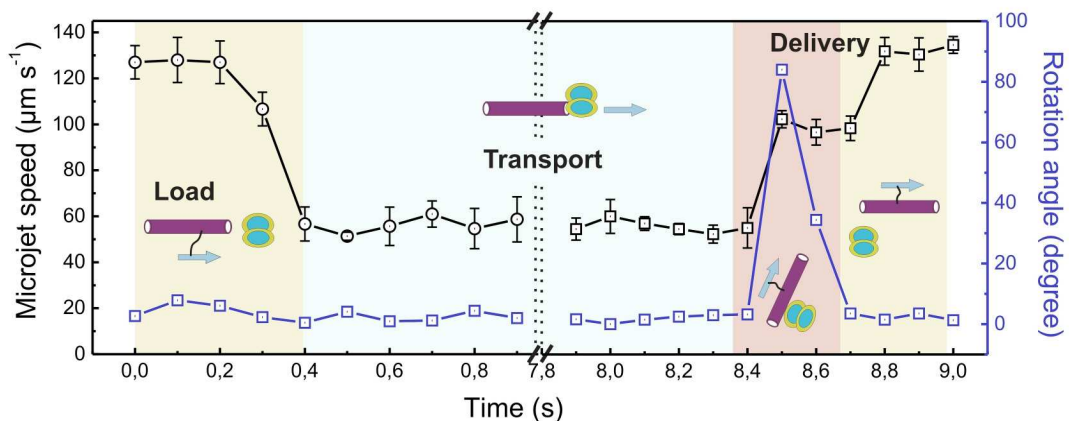
Figure 6.8: Speed of the microjet (left *y* axis, black circles) and the angle of rotation (right *y* axis, blue line) during loading, transportation and delivery of CAD cells. Background colours: yellow - microjet free of cells; grey – transporting two cells; orange – delivery of cells.

Fig. 6.8 illustrates the microjet speed and angle of rotation during the loading, transportation and delivery of the CAD cells. The microjet is self-propelled in 4 % v/v peroxide containing 0.005 v/v % of benzalkonium chloride and 25 % of cells medium. The initial speed, i.e., before loading cells, is 130 $\mu m \cdot s^{-1}$ and it is reduced to 60 $\mu m \cdot s^{-1}$ right after the loading of CAD cells (Fig. 6.8, left y axis). The main reason of the deceleration of the microjet speed is the increase on the drag force exerted by the loaded cells. During the next 8 seconds the speed does not change significantly until the magnetic field is abruptly turned 90° within 0.2 s (Fig. 6.8, right y axis) leading to the delivery of the cells (detachment) and consequently an increase of the speed up to 70 $\mu m \cdot s^{-1}$ is observed. It is important to note that the cells remain loosely attached to the wall of the microjet. Shortly after the first turn, another 'shake' of 40° was necessary to achieve the total delivery of the cells.

6.3 Microengines in Microfluidic Channels

Synthetic micromachines are of high interest to integrate with Lab-On-a-Chip devices. In particular, only one report concerning application of catalytic nanomotors in microfluidic channels has been made.[140] Although the performance of microjets was well demonstrated, their motion in microfluidic channels and the transport of multiple particles have not been reported so far. Besides, the motion of the catalytic micromachines in the microchannels with flowing fluidic streams mimic hydrodynamic conditions of the human circulatory system. Thus, it is of interest for medical applications of microjets. Here, the controlled motion of Ti/Fe/Pt microjets in the microfluidic channels is demonstrated, where microjets capture and transport polysterol particles in microfluidic channels. The motion of microjets is reported against and along the flowing microfluidic streams.

6.3.1. Results and Discussions

The accurate control of autonomous microjets self-propelled within polydimethylsiloxane (PDMS) microfluidic channels is shown in Figure 6.9. First, the Ti/Fe/Pt microjets were suspended along with polystyrene microparticles (5 μm in diameter) in a reservoir chamber (1 cm^2) containing hydrogen peroxide solution (8.75 % v/v) and a common soap (*Fit Gmbh*, 5 % v/v). The optical images in Fig. 6.9 A-C show a microjet moving and being directed from the wide microfluidic channel (Fig. 6.9 A) toward the narrower working areas (Fig. 6.9 B, C), wherein microparticles were loaded and transported. It is important to note that in the case of microfluidic channels a high concentration of common soap (5 % v/v) was used to reduce the size of the bubbles, which otherwise would expand and block the channels. At a higher concentration of soap, microbubbles are small enough and microjets can easy overcome them.
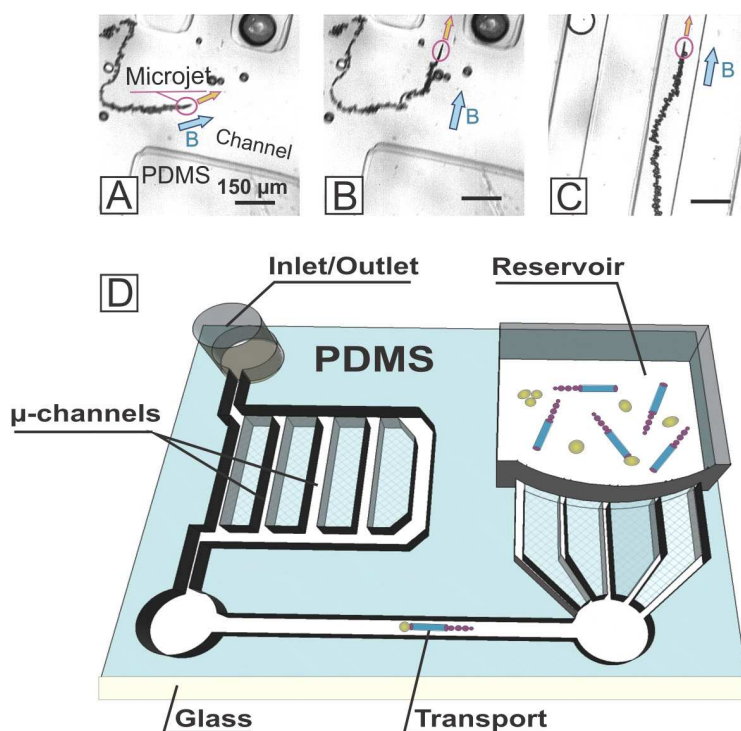
Figure 6.9: Remote controlled motion of microjets in microfludic channels. (A–C) Optical microscopy sequence of the microjet moving in the microchannels of a PDMS chip. The blue arrows represent the direction of the magnetic field and yellow arrows show the direction of the microjet motion. (D) Scheme of the fabricated microfluidic chip which was used to study microjets motion in channels.

The microjet faced the entrance of the microchannel (Figure 6.9 B) and then followed a straight trajectory achieved while the magnetic field was kept stationary (Figure 6.9 C). As an example, a microjet moved against flow (with speed 73 $\mu m \cdot s^{-1}$) at 78 $\mu m \cdot s^{-1}$ for 13 s. Tracer polystyrene particles with diameters of 5 μm were used to correlate the flow rate. The multiple and individual steering of microjets, either in free bulk solution and/or in microchannels with spatial precision is possible. A reduction in the speed of nanomotors propelled in the PDMS microchannels relative to that of nanomotors in free solution was previously reported. The authors hypothesized that lower speeds were caused by absorption of the stationary H_2O_2 into the PDMS matrix.[140] To overcome the possible absorption of fuel, a flow of hydrogen peroxide solution was introduced into the microchip chamber that allows at the same time a continuous supply of the fuel to the microjets. In order to study whether our microjets were able to produce enough propulsion power by themselves without further alterations, they were directed against flowing streams, as shown in Figure 6.10 A. The laminar flow in the microchannels had a parabolic profile [45] (i.e., the flow is faster at the center than at the edges). This phenomenon can be observed in the motion of the particles.
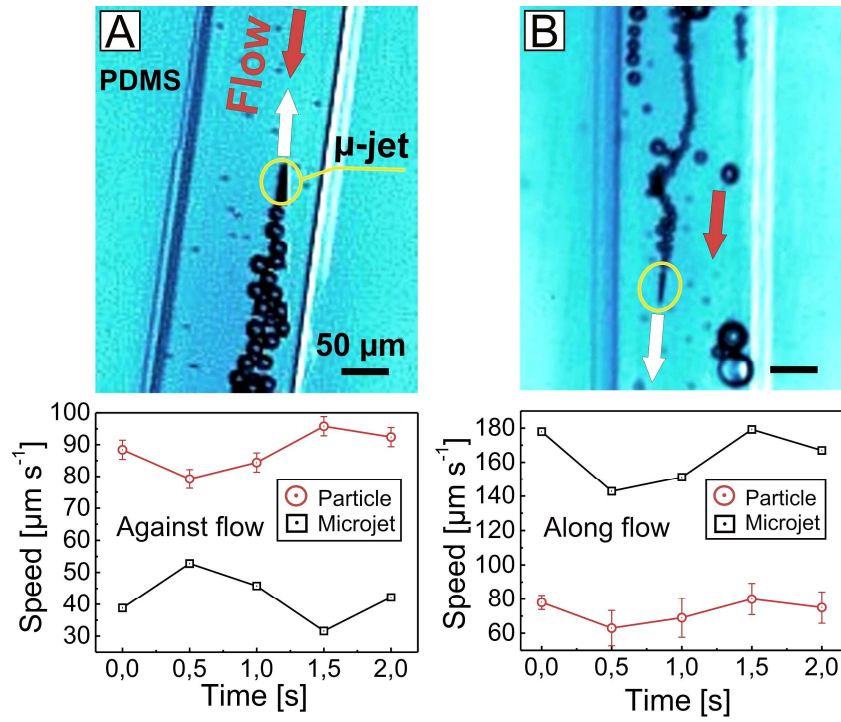
Figure 6.10: Microjets moving (A) against and (B) along the continuously induced flow of fuel in the microchannels. The plots at the bottom depict the speed of the tracer particles (*n* = 5) and the microjets in absolute values.

Thus, all of the represented data points in Fig. 6.10 correspond to particles moving near the microjet in the center of the microchannel. Also, the microjet was navigated to the center of the channels to obtain either the maximal propulsion or the maximal drag force. As expected, the increase in the flow rate (and thus a higher hydrodynamic drag force) induced a reduction in the motion of the microjets, whose speed dropped from 50 to 30 $\mu m \cdot s^{-1}$ as the flow rate increased from 80 to 100 $\mu m \cdot s^{-1}$ in the opposite direction (Figure 6.10 A). In addition, a microjet moving along, i.e. in the same direction, as the flow accelerated, acquiring speeds ranging from 140 to 180 $\mu m \cdot s^{-1}$ (Figure 6.10 B).

The loading of microparticles into microchannels was studies, as represented in Figure 6.10. The speed of the microjet decreased with the number of particles loaded; nevertheless, the microjet was able to load two consecutive particles, one after another. The microjet moved at a speed of ~160 $\mu m \cdot s^{-1}$ when free of cargo and decelerated linearly as more particles were loaded. The pickup of the first particle is shown in Figure 6.11 A–B. At this point, the speed was reduced from 125 $\mu m \cdot s^{-1}$ with one particle loaded (see zoomed image in Figure 6.11 B) to 72 $\mu m \cdot s^{-1}$ when transporting two particles (zoomed images in Figure 6.11 B, C). The reduction in speed is attributed to two reasons: (i) the increase in the drag force with increasing number of particles transported and (ii) the partial blocking of the entrance of the tube by the loaded particles, which might reduce the fluid pumping and therefore the

propulsion. The equivalent microjet force for pushing a single 5 μm diameter particle was calculated to be 7.3 pN.
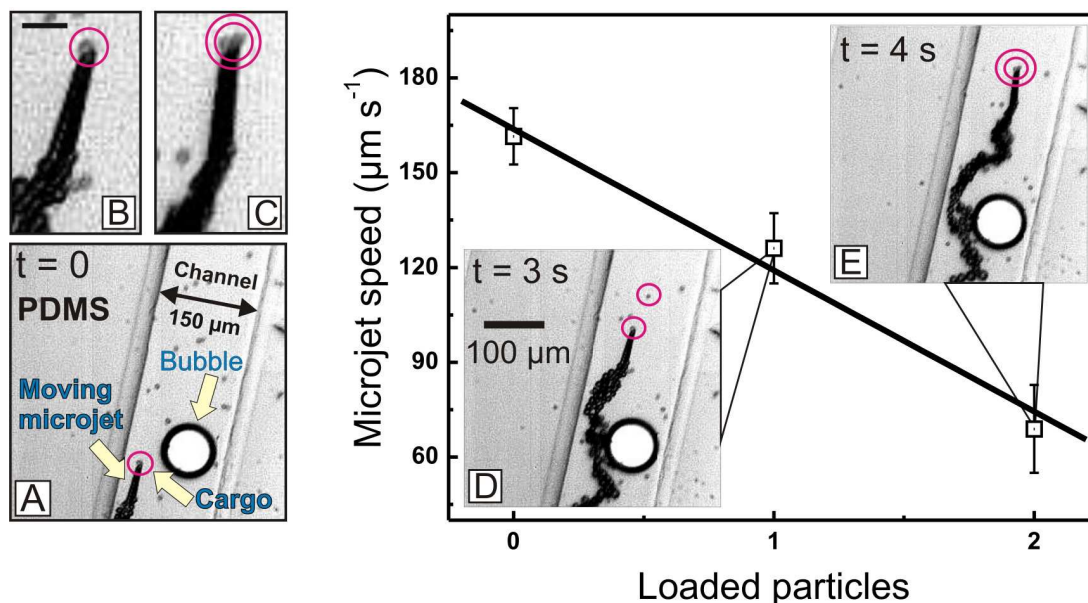
Figure 6.11: Catalytic Ti/Fe/Pt microjet loading and transporting 5 μm diameter polysty-rene particles in microfluidic channels. The plot shows the dependence of the microjet speed on the number of particles loaded. (A) Moving microjet sorting a residual bubble into a 150 μm wide microchannel in a PDMS microchip. (B, C) Zoomed images of the microjet loading (B) one and (C) two microparticles. (D, E) Microjet transporting (D) one and (E) two microparticles in the micro-channels.

6.4 Summary

The integration of ferromagnetic (Fe) layer into the body of microengines enabled the remote control of their motion. Moving trajectories can be controlled by external magnetic field, which can lead to the motions in straight lines or circular "micro-docks". These results show that the peroxide fuel is pumped into the front end of the microjet engines, while microbubbles are generated at the opposite end. The loading of particles was facilitated by the pumping of fluid into the microtubes via catalytic reaction. The movement control of the microengines by external magnetic field helped to accurately load and deliver cargo into desired places. Thus, microengines have enough power to carry many particles without any magnetic or chemical modi-fication of the cargo-microjet system. Different kinds of materials, such as polymer, metallic and biological cargo microobjects were transported. Important to note, bio-logical cells which were loaded at the front end of the microjets do not halt the sup-ply of fuel and therefore the motion does not stop. Demonstrated motion of microjet engines in microfluidic channels show high potential of microjets for Lab-on-a-Chip devices.

7 Light-Controlled Power of Micro-Jet Engines

The tuning of the propulsion power of Ti/Cr/Pt catalytic microjet engines is demonstrated through illumination of solution with a white light source, shown in Scheme 7.1. Light suppresses the generation of microbubbles, produced by the catalytic microengine, stopping the microengines if they are fixed or self-propelled above a platinum-patterned surface. The microengines are re-activated by switching off or decreasing the intensity of the light source that illuminates the fuel solution. The influence of local fuel conditions, wavelengths and intensities of light in the visible spectrum (500–750 nm) on the generation of microbubbles are investigated (parts of this Chapter were adapted from ref. [25]).

Scheme 7.1: New method of microjet control by a white light source is shown. Optical microscopy images (bottom) show individual self-propelled (left) and stopped (right) microengine right after it was illuminated using a white light source.

7.1 Introduction

The control over the power of machines is essential for real applications. Particularly, it is important for micro- and nanotechnology. Consequently, a versatile machines should be able to be turned on and off on demand. Although external magnetic field can be used to turn the directionality of microjets motion, it has no influence on the catalytic reaction, i.e. the power of the microjet engine. Recently, the use of a light source has been implemented to propel particle-based micromotors,[142] which generate force by self-diffusiophoresis. Despite of this demonstration, the motion of these micromotors is limited rigorously by the dissolution of the motor own material or to the ultra-violet (UV) spectrum of light.[143] Up to date, a reversible method to start and stop self-propelled micromachine by means of a visible light source has remained a challenge. A new method to control the power of catalytic microjet engines by a white light source is described in the following pages.[25]

7.2 Results and Discussions

Microjet engines are self-propelled above platinum patterned silicon surface in aqueous solution of H_2O_2 (2.5 % v/v) and BC surfactant (0.5 % v/v). A white light source is used to stop the motion of microjet engines. At concentrations of both chemicals above a certain threshold, the generation of microbubbles is started. Conditions when microengines start moving by microbubbles allow to investigate a concentration region close to the bistable state, i.e. when the probability of stopping the generation of microbubbles is high.
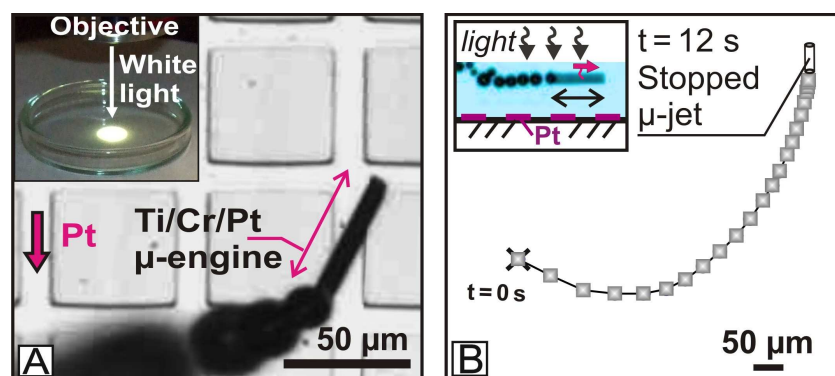
Figure 7.1: Light-controlled motion of individual catalytic microjet engines. (A) Optical image of a self-propelled Ti/Cr/Pt µ-engine moving above a platinum patterned silicon surface. Inset: local illumination of the fuel solution containing the microjet. (B) Tracked trajectory of a microjet stopped after 12 seconds of illumination above a Pt-patterned Si surface. The time interval between two spots in the plot is 0.5 s. Inset: optical image of the mobile microjets self-propelled above the patterned surface. Rolled-up Ti/Cr/Pt catalytic tubular microengines with diameters of 5–10 µm and a length of 50 µm were prepared as described in the *Appendix*.

Fig. 7.1 A shows an optical microscopy image of a self-propelled µ-engine above a Pt patterned silicon substrate (1 nm thick Pt layer) placed in a Petri dish (~50 mm diameter) under the illumination from a tungsten lamp (inset in Fig. 7.1 A). The microjets moving within the illuminated area rapidly reduce their speed and stop after a few seconds, as shown in Fig. 7.1 B (each point represents the position of the µ-engine after every 0.5 s). As a control experiment, the motion of microjets above unpatterned silicon and glass substrates was studied. Their speed does not decrease with time despite an illumination for more than 1 min (shown in Fig. 7.5) indicating that the presence of a Pt substrate has an important effect on the generation of microbubbles.

Figure 7.2 shows the analyzed deceleration of a microengine which was switched 'off' (Fig. 7.2 A) and switched 'on' (Fig. 7.2 B). Both studied µ-engines are navigating above a Pt-patterned silicon surface. First, the power of the light source is turned to maximum (Fig. 7.2 A) which leads to a full stop of the microjet after a time

lapse of 12 seconds (from 65 to 0 $\mu m \cdot s^{-1}$). This phenomenon is also reversible since by dimming the light source, a static μ-engine activates and accelerates from 0 to 55 $\mu m \cdot s^{-1}$ as the light intensity is further decreased. In both studied cases, i.e. start and stop, the phenomenon is not immediate and thus it requires a few seconds to either fully stop or to acquire maximum speed. The speed of the microjets is directed to the concentration of available hydrogen peroxide.
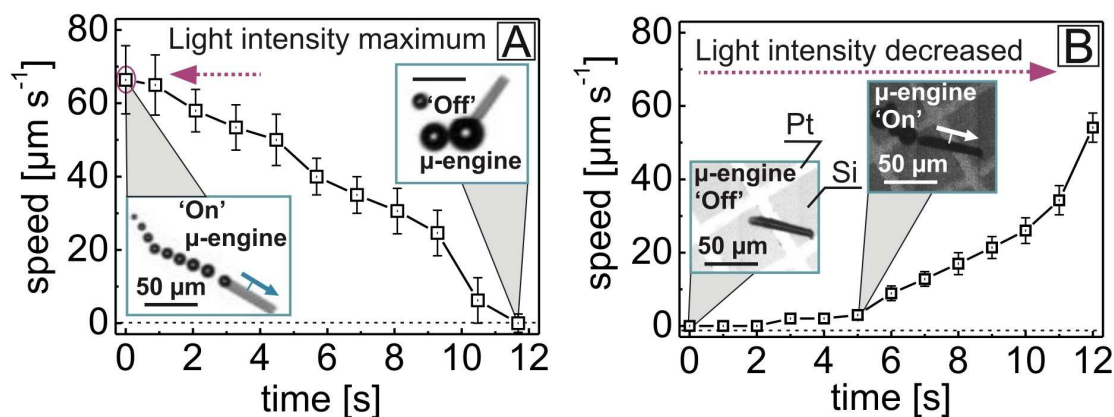
Figure 7.2: Switching the propulsion of individual microjets "off" (A) and "on" (B) using a white light source. (A) The microjets decelerate and stop after a 12 s exposure of the maximum white light power. The insets show a microjet moving (left inset) and stopped (right inset). (B) Starting of the self-propulsion of a microjet while decreasing the intensity of light.

The decomposition of H_2O_2 under visible and UV light is accompanied by the generation of highly reactive oxygen species such as -OOH and •OH radicals.[144, 145, 146] Response to visible light by photo-catalysts can also be increased due to Pt loading into semiconductor structures.[147] This can create reactive radicals with an addition of hydrogen peroxide solution.[148] Surfactants degradation by an addition of peroxide while illumination with light, have been well studied in cases of the photo-Fenton process,[149, 150] and photocatalysts.[151, 152] The wetting of the inside of the microengines is very sensitive to the surface tension of the fuel, which is regulated by the surfactant.[23] Thus, a small decrease in its concentration will lead to a reduction of the speed and to the formation of larger bubbles. Insets in Fig. 7.2 A show a difference in bubble size before and after illumination, which indicates that the surfactant and hydrogen peroxide concentration has been modified during the exposure of light.

Microbubbles study at different peroxide and BC concentrations at low intensity of white light is presented in Figure 7.3. Here, it is important to note that the microjets are only stopped when they are self-propelled directly above the Pt-patterned substrates, confirming the *in situ* decomposition of peroxide enhanced by Pt in the presence of visible light.

7.2.1. Influence of White Light Power, Surfactant and Fuel

Since the continuous motion of self-propelled microjets complicates a thorough study, the influence of the light illumination on microjets attached to a Pt-patterned Si substrate was investigated [This experiment was carried out in collaboration with Dr. E. J. Smith]. Figure 7.3 A shows the influence of the H_2O_2 concentration on the bubble generation at different light intensities while maintaining a constant BC concentration (5 v/v %). A transition from 2 % to 3 v/v % of H_2O_2 changed the initial bubble frequency from 1.5 Hz to 7.25 Hz (intensity of 140 arb. u.). This jump in frequency is 4.2 times higher in comparison to a jump from 3 % to 4 % peroxide concentration.
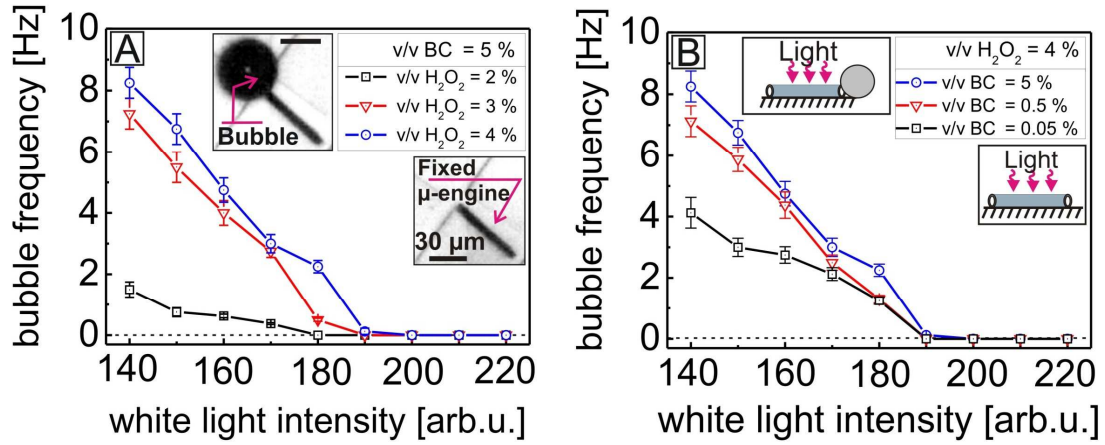
Figure 7.3: Bubble frequency of fixed microjets at different intensities of white light while varying the (A) H_2O_2 and (B) BC concentrations. The insets show optical micrographs and schematic of the microbubble recoil from a microjet, before (left) and after (right) being stopped by light. Error bars in both figures represent statistical data of microbubble generation from individual microjets over 4 seconds.

Despite the different initial peroxide concentration, the bubble frequency decreases in all cases when the intensity of light reaches 190 arb.u. Beyond this intensity, no more bubbles are released from the tubes (yellow region on the plots). Fig. 7.3 B shows data of microjets by varying the BC concentration from 0.05–5 v/v %, while maintaining a constant concentration of hydrogen peroxide (4 v/v %). Reducing the BC concentration by one order of magnitude from 5 to 0.5 % does not produce an enormous change of the bubble frequency. However, decreasing it to 0.05 %, reduces the frequency to half of the initial (from 8.2 Hz to 4.1 Hz). Consequently, it is clear that the release of bubbles is sensitive to both components of the fuel and to the light intensity. A reversible switching 'off' and 'on' of microjets is achieved by an increase and decrease of the white light intensity. This effect is local and it takes place only in the illuminated region. For instance, if the illuminated area is moved along the surface with the fixed microjets, the no-longer-illuminated regions activate im-

mediately after, while the microengines under the illuminated region are stopped. It is hypothesized that the reactivation of the microengines is due to fluid diffusion from the nonilluminated surroundings (i.e. replenishment of un-degraded peroxide and surfactant, allowing for a recovering of the initial propelling conditions).

7.2.2. Influence of Laser Light Wavelength and Power

A supercontinuum white light laser source in conjunction with a monochrometer is used to determine the spectral and intensity influence of visible light on the frequency of microbubbles [This experiment was carried out in collaboration with Dr. E. J. Smith]. For this purpose a laser spot, emitted from a fiber output of the monochrometer, illuminates the sample surface. Experimental setup consisting of the laser, monochrometer, and a 50:50 beam splitter for *in situ* monitoring of the intensity of light illuminating the sample (the setup is described in Chapter 2). This setup allows performing *in situ* monitoring of the microbubble frequency in response to a predefined intensity and wavelength (wavelength resolution 2 nm full width at half maximum).
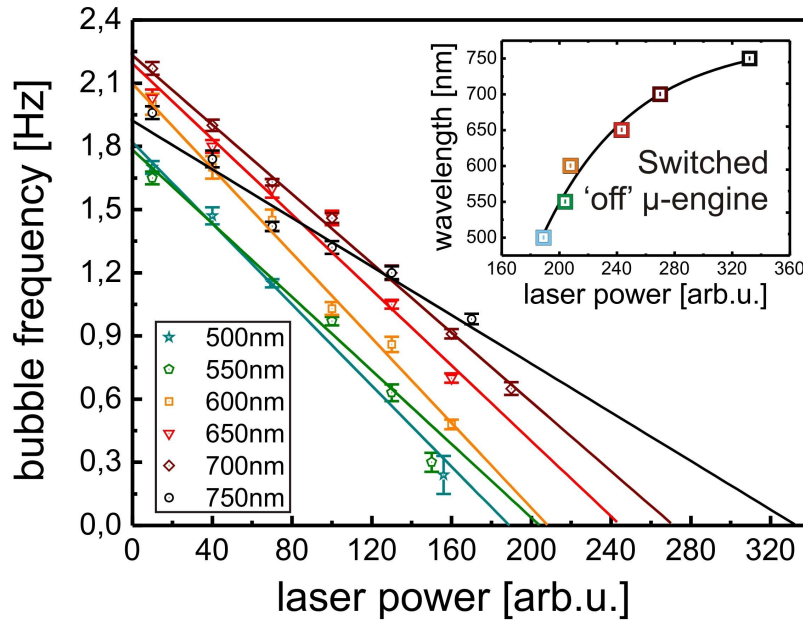
Figure 7.4: Dependence of bubble frequency on the individual wavelengths from a white light laser. Straight lines represent a linear fit to experimental points, extrapolated to the point where the microengines are not active. The inset plots the extrapolated points corresponding to the power required to switch 'off' the micro-jets depending on the laser wavelength. Below this curve, the microbubbles are switched 'off'.

Fig. 7.4 shows a quantitative analysis of μ-engines illuminated by the laser spot at different wavelengths and intensities (here 1 arb.u. ≈ 1 μW) immersed in a 2 v/v % H_2O_2 and 0.5 v/v % BC aqueous solution. The graph in Fig. 7.4 shows linear fits to the experimental points, representing the change in microbubble frequencies at

different laser power and wavelengths with interval steps of 50 nm. The linear plots are extrapolated to the point of zero bubble frequency in order to determine the conditions of the light intensity and power to stop the microengines. The inset graph of Fig. 7.4 shows a logarithmic fit to the extrapolated points. The region below the curve reveals an area where a μ-engine is switched 'off' and the region above the curve is where it is switched 'on'. This data clearly shows that the sensitivity of microbubble generation is highest at shorter wavelengths. Nevertheless, it is possible to fully stop the generation of microbubbles at longer wavelengths by increasing the intensity of the light. The energy of a photon depends on its wavelength (λ) and equals $E = h \cdot c/\lambda$, where c is the speed of light and h is Planck's constant. Subsequently, light with higher energy, corresponding to shorter wavelengths (i.e. for $\lambda =$ 500 nm $E = 2.48$ eV, and $\lambda = 750$ nm $E = 1.65$ eV) degrades the H_2O_2 more rapidly. Error bars here were calculated as the standard deviation of 20 to 100 (depending on available data points) independent measurements of microbubble generation.

7.2.3. Non-Stoppable Propulsion

Motion of the catalytic microjets was studied under white light above planar Si surface using the same solution, which is sample from the same batch, described for Fig. 7.1. Fig. 7.5 displays an individual self-propelled Ti/Cr/Pt μ-engine which did not decrease its propulsion power with time under maximum intensity of white light (illuminated by 100 W bulb 10x ocular of Zeiss Microscope).
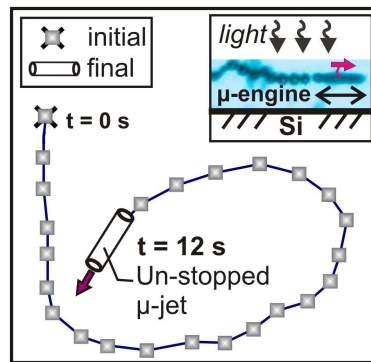
Figure 7.5: Tracked trajectory of an individual microjet engine self-propelled above bare silicon surface during 12 seconds. Insets show self-propelled microjet with length of 50 μm in solution with schematics, showing the light beam illuminating the μ-engine (note: micrograph picture was actually a top view, here it is represented as side view to understand better the location of microjet). Each point represents microengine position every 0.5 s.

The initial average speed 190 μm·s^{-1} was not affected after 66 seconds of illumination. The crossed square shows an initial position of the microjet and the schematic microjet shows its final pos tion over longer period of time. The investiga-

tion of several microengines confirmed ition. The trajectory was tracked over 12 seconds which demonstrates microjets mo that it is not possible to stop generation of oxygen microbubbles and consequently the propulsion of catalytic microjets above Si or glass surfaces.

7.2.4. Optimization of Surfactant and Hydrogen Peroxide Concentrations

Figure 7.6 shows how bubble radius depends on the surface tension of the fuel solution (adjusted by an addition of BC surfactant) and concentration of H_2O_2 [This experiment was carried out in collaboration with Dr. S. Sanchez]. An array of microengines integrated on Si substrate (containing Pt patterned surface) was studied. To avoid influence of white light and understand better how solution affects microbubbles diameter we kept white light at the lowest possible intensity.
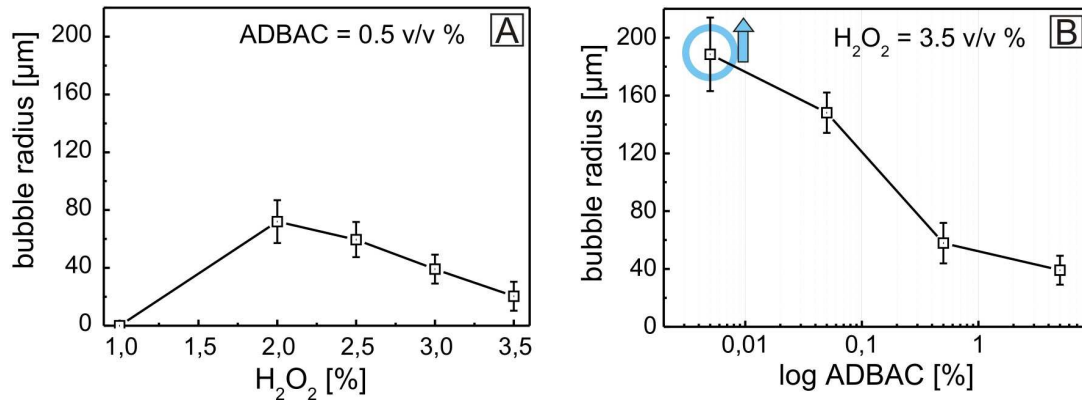
Figure 7.6: Study of different solutions, which effect generating bubble radius at a low intensity of white light, (A) different concentrations of hydrogen peroxide (1–3.5 v/v %) and constant concentration of surfactant BC (0.5 v/v %) and (B) different concentration of BC ($5 \cdot 10^{-3}$ – 5 v/v %).

Every point in plot represents an average of five consecutive bubbles from different microengines located on the same substrate. Graph 7.6 A shows that upon systematic decrease of hydrogen peroxide concentration, the average radius of the microbubbles increases, however below 2 v/v % H_2O_2 the generation of microbubbles is stopped. A similar trend, shown in Fig. 7.6 B, is observed upon the decrease of BC concentration. However, at very low concentrations of surfactant, the microbubbles do not disappear – they grow and reach sizes of about 190 µm of radius and bigger. It is indicated that by the blue circle and arrow bar at concentration $5 \cdot 10^{-3}$ v/v %. It is expected that if only surfactant is degraded by light, which must increase local surface tension, microbubbles would not disappear upon exposure to light. Because microbubbles do disappear during illumination we conclude that peroxide degradation must also take place which can influence a local surface tension as explained in the

main text. In addition, the study of surface tension before and after exposure to light confirms that degradation of surfactant must be mediated by reactive species created during the illumination of hydrogen peroxide.

7.2.5. Cyclic Voltammetry

By means of electrochemical measurements the generation of oxidizing species from a H_2O_2 solution was investigated after illumination with white light. Fig. 7.7 depicts the Cyclic Voltammetry measurements, showing that the oxidation peak at 0.8 V (vs Ag/AgCl) increases after illumination, meaning that ionic species are generated in the solution [This experiment was carried out by Dr. S. Sanchez and Dr. C. C. Bof Bufon]. All cyclic voltammetric experiments were performed using an electrochemical analyzer μ-Autolab type III potentiostat/galvanostat (Ecochemie, Utrecht, the Netherlands) connected to a computer. Electrochemical experiments were carried out in a 5 mL voltammetric cell at room temperature (25 °C), using a three-electrode configuration.
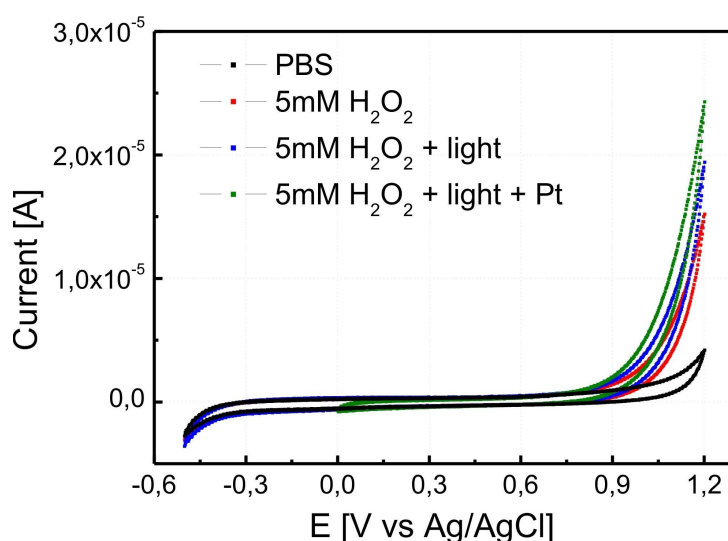
Figure 7.7: Cyclic voltammetry in PBS solution pH = 7 of 5 mM H_2O_2 before (red) and after (blue) the illumination with white light to the solution and (green) after illuminating a solution containing a wafer sputtered with Pt thin film.

A platinum electrode served as an auxiliary electrode and an Ag/AgCl electrode as a reference and glassy carbon electrodes (3 mm diameter). All values of electrochemical potential reported in this work are stated vs. Ag/AgCl. Cyclic voltammetric experiments were carried out at a scan rate of 100 mV·s^{-1} using Phosphate Buffer Solution (PBS) pH 7.0. The effect of platinum as catalyst in the electrochemical oxidation of hydrogen peroxide has been broadly reported in literature. The cyclic voltammograms (Fig. 5.18) show that the oxidation peaks of 5 mM hydrogen peroxide (red line) starts at +0.9 V. When a white light source illuminates the peroxide so-

lution for 1 min, the intensity of the voltammetric signal increases in the current response (blue line). Next, a Pt-patterned Si wafer was placed in close contact to the electrodes, enhancing the decomposition of H_2O_2 in an electrochemical cell as clearly seen in the increase of the oxidative current (green line). All the depicted voltammograms correspond to the third voltammetric cycle. Such response clearly shows that light influences the electrocatalytic decomposition of hydrogen peroxide at Pt surfaces. The reactions describing the hydrogen peroxide decomposition have been previously reported in the literature.[153] The H_2O_2 can decompose into O_2 and ·OH radicals which might lead to an increase on the anodic current while illuminating the solution in the presence of Pt catalyst. These oxidative species might lead into decomposition of the surfactant molecules in the close vicinity of Pt surface, in similar manner as reported before.[154] Although the electrochemical experiments are not conclusive by themselves, the analysis on surface tension to confirm this hypothesis was performed.

7.2.6. Measurement of Surface Tension

Surface tension measurements confirm that the combination of light and Pt surfaces degrades the surfactant, increasing the surface tension of the solution, as shown in Table 7.1 [This experiment was carried out in collaboration with Dr. S. Sanchez]. Surface tension of the working solution, i.e. H_2O_2 2 v/v % and BC from 0.5–0.05 % v/v was measured before and after exposure to white light. Results are shown in Table 7.1. Surface tension measurements were performed by evaluating the drop profile for each surfactant in a computer controlled KSV CAM101- optical contact angle and surface tension meter. A 150 W white lamp was used for the light exposure.

Experiment	BCl, 0.5 %	BCl, 0.05 %
Solution before exposure to light (mN/m)	32.4	35
Solution after exposure to light, Si surface (mN/m)	33.6	41.7
Solution after exposure to light, Pt patterned on Si (mN/m)	35.3	54.9

Table 7.1: Solution surface tension measured before exposure to white light, probed from Si surface and Pt patterned Si surfaces.

In comparison to initial value, the results of BC 0.5 v/v % and H_2O_2 2 v/v % clearly indicate an increase of surface tension on 3 % after switch on of white light over Si surface and on 9 % if Pt patterned surface is used. For BC 0.05 v/v % and H_2O_2 2 v/v % this difference is even increased. The surface tension after light expo-

sure over Si surface is 19 % higher and 57 % higher than the initial value if a Pt patterned Si surface is used. The results indicate that a degradation of the surfactant is taking place, enhanced by the presence of light and Pt layers.

7.3 Summary

The control over the propulsion of microbubble-driven Ti/Cr/Pt microjet engines with a white light source is demonstrated. Light induces a local concentration decrease of both the hydrogen peroxide fuel and the surfactant. An implemented white light source was used to switch "off" and "on" the microjet power/speed on demand during timescale of seconds. This process was mediated through the illumination of the fuel solution above platinum patterned silicon surfaces. Although white light can be used to switch off microengine propulsion, shorter wavelengths suppress the generation of microbubbles more rapidly in comparison to longer wavelength. It was shown that an interior of microjets, i.e., generation of microbubbles, is very sensitive towards change of surface tension and concentration of the hydrogen peroxide molecules. A local illumination of the Pt patterned silicon substrate creates highly reactive oxygen species from hydrogen peroxide. It was hypothesized that these reactive species cause the degradation of surfactant which indicate measurements of solution surface tension. Electrochemical measurements support this finding. In future the role of Pt patterned surface has to be determined. It can have additional effect due to possible interaction with light, like in case of semiconductor materials, where additional charges can appear (electron-hole pairs). These results open the door towards many practical applications including full remote control over the power of micro- and nanomachines.

8 Self-Propelled Nanotools based on the Nano-Jet Engine

Nanoscale tools are described in the form of autonomous and remote controlled catalytically self-propelled InGaAs/GaAs/(Cr)Pt tubes. These rolled-up tubes with diameters in the range of $280 - 600$ nm, move in hydrogen peroxide solutions with speeds as high as 180 $\mu m \cdot s^{-1}$. The effective transfer of chemical energy to translational motion has allowed these tubes to perform useful tasks such as the transport of cargo. Furthermore, it was observed that asymmetrically rolled-up nanotubes move in a corkscrew-like trajectories allowing these tubes to drill and embed themselves into fixed cancer cells, shown in Scheme 8.1. These observations suggest that the shape and asymmetry of nanomaterials can be utilized to direct the motion of catalytic nanojets and enable mechanized functions at the nanoscale (parts of this Chapter were adapted from ref. [26]).
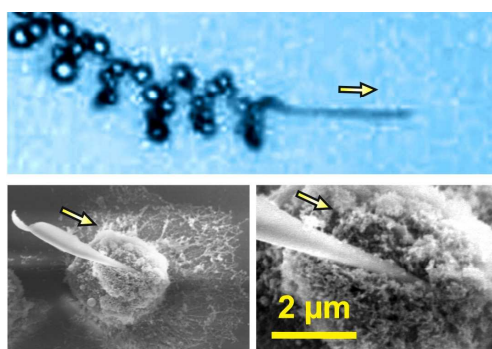
Scheme 8.1: Optical microscopy (top) and SEM images (bottom) of self-propelled nanotube which drilled autonomously cancer cells material.

8.1 Introduction

The mimicry of mechanized macroscale functions at the nanoscale is important for nanomanufacturing and nanorobotics.[1, 18] However, even simple macroscopic tasks are extremely challenging at these small scales, since it is hard to achieve and control nanoscale actuation reproducibly, reversibly and especially in a wireless manner. It is noteworthy that versatile methods to roll-up nanomembranes into functional tubes have been previously demonstrated.[31, 130, 155, 156, 157] Among these methods, roll-up nanotechnology on polymers, described througout this dissertation. However, these methods do not allow the reduction of tubular diameter to nanoscale. Here, catalytic nanotubes, representing "the smallest man-made jet engine", are fabricated by using heteroepitaxial layers.[158, 159] Furthermore, it was found that the asymmetry in the shape of the rolled-up heteroepitaxial nanotubes is im-

portant for trajectories of their motion and that it can be utilized to enable functional nanotools. The use of rolled-up tubes as nanomechanical tools, such as nanodrillers, was motivated by the proposal made over ten years ago by Schmidt, Eberl,[130] and recently demonstrated miniaturized mechanical surgeons.[160, 161, 162] Here, the proof-of-concept of nanotools realization is provided.

8.2 Results and Discussions

Molecular beam epitaxy (MBE) was utilized to deposit thin films of InGaAs/GaAs on sacrifical AlAs layers and bulk GaAs substrate. Considerable strain in such heteroepitaxial layers cause them to roll up into tubes with nanoscale diameters upon release from the substrate, as previously demonstrated.[163, 164] In order to create self-propelled tubes it was necessary to deposit a catalytically active platinum (Pt) layer. Even with this Pt layer, it was observed that the strain in the MBE membranes was high enough so that catalytic nanotubes with diameters approximately 20 times smaller than previously reported rolled-up catalytic microjets [20, 23, 24]. Consequently, results about the smallest man-made catalytic jet engines are described here. Using these smaller tubes, several important questions were addressed. Can nanotubes overcome Brownian diffusion and move along a specific trajectory? Can the shape be utilized to alter their trajectories and as a result permit new functionalities? Can the power derived from such motion be used to perform useful tasks?

To create catalytically active roll-up tubes, the successive growth of the sacrificial AlAs layer (20 nm) and the strained $In_{0.33}/Ga_{0.67}$ As/GaAs bilayer (3/3 nm) by Molecular Beam Epitaxy on a GaAs (001) substrate was followed by magnetron sputtering of different thicknesses of Pt layers. After the deposition of metals, trenches were defined for under-etching, by scratching the samples. The selective etching of the AlAs layer was achieved using an 8.3 % (v/v) HF solution for 30 seconds, which induced the roll-up process by strain relaxation. Samples were fabricated with different thicknesses of Pt layers from 0.5 nm to 2 nm and observed that a thicker Pt film leads to an increase in the diameter of the nanotubes from 280 up to 600 nm (Fig. 8.1). This increase is attributed to the increase in the overall layer thickness, as has been discussed before.[164, 165, 166]

8.2.1. Fabrication of Nanotools

The fabrication process is depicted in the lower inset of Fig. 8.1, showing the roll-up of the heteroepitaxially grown InGaAs/GaAs/Pt nanomembranes. The upper inset of Fig. 8.1 shows a Focused Ion Beam (FIB) cut SEM image of a cross-section of an individual nanotube consisting of InGaAs/GaAs/Pt (3/3/0.5 nm) films.
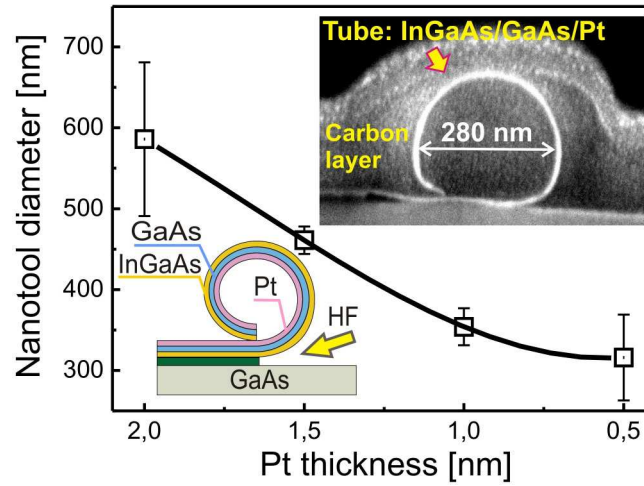
Figure 8.1: Scalability of the diameter of rolled-up nanotubes consisting of hybrid heteroepitaxial catalytic InGaAs (3 nm)/GaAs (3 nm)/Pt thin films. Bottom inset shows the rolled up fabrication process by selective under-etching of the sacrificial AlAs (20 nm) layer. Top inset depicts a SEM image containing a focused-ion-beam (FIB) cut of an individual tube composed of InGaAs/GaAs/Pt (0.5 nm).
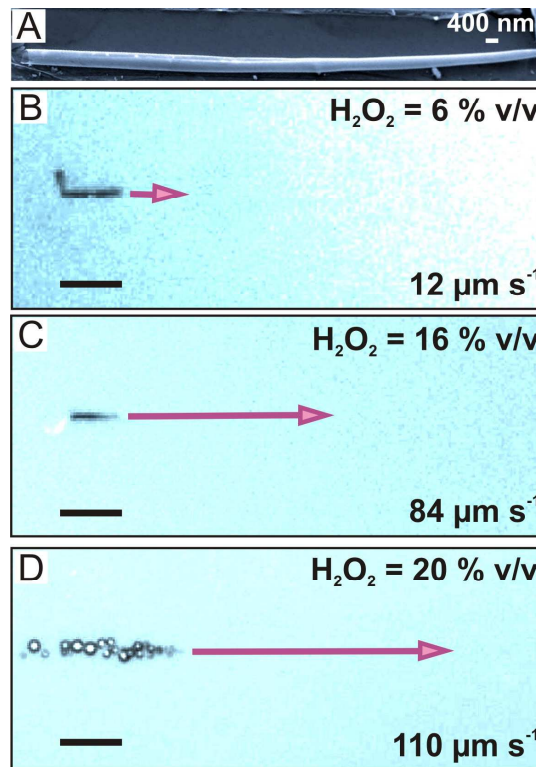
Figure 8.2: Motion and speeds of cylindrical catalytic rolled-up nanotubes (nanojets) in different concentrations of fuel solution. (A) SEM image of hybrid heteroepitaxial catalytic InGaAs/GaAs/Cr/Pt (3/3/1/1 nm) nanotube with average diameter 600 nm. (B-D), optical microscopy images of catalytic nanojets self-propelled in 6, 16 and 20 % v/v H_2O_2, recorded during 1 second. Arrows shows the velocity magnitude at different fuel conditions. Scale bar in B-C is 15 μm and in D is 30 μm.

In order to enhance the stability and mechanical rigidity of the tubes for reproducible nanotools, Cr (1 nm) as an additional adhesion layer was sandwiched between the InGaAs and Pt layers. The rolled-up thin film stack of InGaAs/GaAs/Cr/Pt (3/3/1/1 nm) had an average tube diameter of 600 nm. This number is similar to the diameter achieved when 2 nm of Pt is deposited in a thin film system of InGaAs/GaAs/Pt, as can be seen from Fig. 8.1. Cylindrical or asymmetrically rolled tubes can be obtained by scratching the thin films in different directions. Fig. 8.2 A shows an SEM image of an InGaAs/GaAs/Cr/Pt nanotube with a slightly conical-like geometry of 10 μm length. Platinum coated rolled-up tubes move autonomously as nanojets when they are immersed in a solution of hydrogen peroxide. The catalytic nanojets are powered by the decomposition of H_2O_2 into molecular oxygen which accumulates in the small cavity and eventually gets released from one end of the nanotube as visible bubbles (Fig. 8.2 B-D). Figure 8.2 B-D illustrates the motion and trajectories of In-GaAs/GaAs/Cr/Pt (3/3/1/1 nm) nanojets immersed in different concentrations of peroxide fuel. The depicted nanojets move at speeds of 12, 84, and 110 μm s^{-1} for 6, 16, and 20% v/v H_2O_2, correspondingly. These results demonstrate that bubble driven catalytic nanojets can indeed overcome Brownian diffusion as well as the high viscous forces of the fluid at low Reynolds numbers.[4] To reduce the high surface tension inside the small tubes, 10% v/v of surfactant was added into the fuel solution. Since at 20 % v/v H_2O_2 the nanojets acquire high speeds and yet controllable directionality, we selected those fuel conditions as ideal to demonstrate the capabilities of these jets as nanotools.

8.2.1. Kinematics of Nanotools

While a few tubes rolled-up into cylinders (Fig. 8.3 A), the vast majority of tubes rolled up at an angle, mainly due to the substrate orientation since layers favor rolling along the (In)GaAs <100> direction. As a result, many of the fabricated nanotubes present a sharp tip, clearly seen in Fig. 8.3 A (b-c). The release of bubbles from these rolled-up structures is asymmetric in nature, thus the catalytic nanojets move in curved trajectories (Fig. 8. 3 B, b and c). As a comparison, nanojet (a) which has a straight opening self-propels linearly at 50 μm s^{-1} during 2.2 seconds, whereas nanojet (b) moves in a circular trajectory at speed of 63 μm s^{-1} during 3 seconds. Nanojet (c) containing a sharper tip moves in circular trajectories with a larger radius at a speed of 68 μm s^{-1} during 5.2 seconds and at the same time it performs a corkscrew movement. To achieve that specific type of motion, the front end of the nanojet (c) propagates in a straight line along its long axis of symmetry while the back end of the tube performs a helix-like motion. The screw-like motion is observed only for this type of nanojets (Fig. 8.3. A (c)), and it has never been reported either for previ-

ous microscale engines,[20, 23] nor for electrophoretic nanowire-based nanomotors. Fig. 8.3 C shows a schematic of the nanotools' (a) circular, (b) straight and (c) screw-like motions. Straight arrows indicate the direction of motive force and circular arrows show torques (τ) acting on the nanojets. The magnitude of torques depends on the driving force, the length of the lever arm, and the angle between the driving force vector and the lever arm. In the case of straight motion (nanojet (a)), the driving force acts along the long axis of symmetry and it propels the tube in a straight line. In contrast, the origin of a torque in the z-x plane (τ_{zx}) leads to a circular motion, shown in Fig. 8.3 C (b). If an additional torque (τ_{zx}) is present due to a further asymmetry at the edge of the nanotube, it can rotate the tube around its long axis and consequently lead to a cork-screw like motion, shown in Fig. 8.3 C (c).
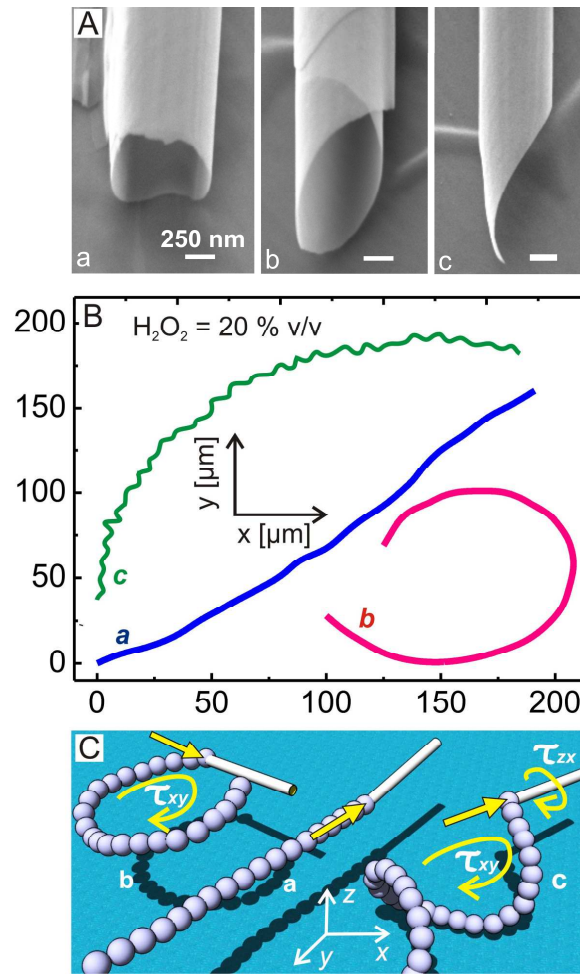
Figure 8.3: SEM images of rolled-up nanotubes with cylindrical and asymmetric geometries and their autonomous trajectories in 20 % v/v H_2O_2 and 10 % v/v surfactant. (A) SEM images of rolled up InGaAs/Cr/Pt layers forming (a) straight cylindrical opening and (b-c) asymmetric "sharp tip" like structures. (B) tracked trajectories of self propelled nanotools following (a) straight (b), circular and (c) corkscrew-like trajectories. (C) Schematic of the trajectories with forces represented by straight yellow arrows and torques represented by circular yellow arrows.

In order to serve as practical tools, guidance from long distance could also be achieved by incorporation of a ferromagnetic layer. The deposition of a thin iron (Fe, 10 nm) layer on the top of the rolled-up tubes allowed steering the nanojets using a small external magnet placed underneath the working solution. Fig. 8.4 A demonstrates the remote magnetic control over the directionality of the motion of the self-propelled nanotools as reported previously for microjet engines.[23] Yellow arrows indicate the direction of nanojet propulsion whereas white arrows show the direction of the external magnetic field (B). It is clear that a small change in the direction of the magnetic field is enough to alter the direction of the nanojets.
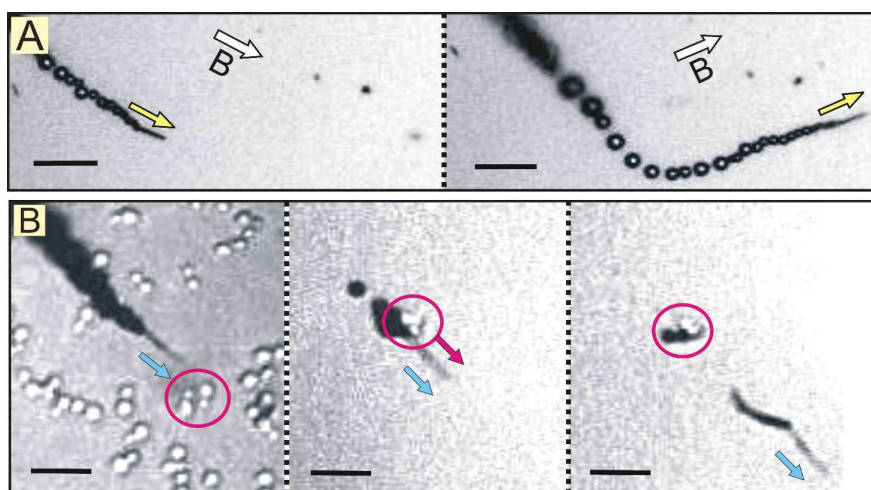
Figure 8.4: Remote magnetic guidance of InGaAs/GaAs/(Cr)/Pt nanotools. These nanojets were sputtered with a 10 nm thick layer of Fe after rolling-up, to enable magnetic guidance. (A) image sequences showing that the nanojets are aligned in the direction of the external magnetic field. (B) Image sequences illustrating the use of self-propelled nanotools for loading, transport and delivery of multiple yeast cells. Scale bars in A and B correspond to 15 and 10 µm.

The capabilities of the nanotools as shuttles of yeast cells were exploited. Fig. 8.4 B illustrates the pick-up, transport and delivery of multiple yeast cells by a catalytic nanotool in 20 % v/v H_2O_2. In the absence of attached cells, the nanotool propels within a region crowded with yeast cells at a speed of 125 µm s^{-1}. The nanotool could be guided to specific cells to be loaded (Fig 8.4 B central panel); when loaded with three yeast cells, the tool decelerated down to a speed of 25 µm s^{-1}. It is noteworthy that even though the nanotool has a length of 10 µm, a dimension similar to the diameter of the three transported cells, it moves at 2.5 body lengths s^{-1} while transporting the cells, illustrating the high power output of the catalytic nanojets.

Since functionalization with antibodies was not used, it is believed that the cells were attached to the outer surface of the nanotool by van der Waals type interactions. The loaded cells were transported over a period of 25 seconds from a

"crowded" area to a "clean" area enabling the transport of cells in solution by self-propelled and remotely controlled nanotools. The continuous rotation of the nanotool and the drag force weakens the attachment of the cells to the tube, so that they are eventually released. We observed that the release of the cells lead to an acceleration of the nanotool reaching speeds of about 180 μm s^{-1}. Note that this speed is higher than the initial speed in the "crowded" area, where the nanotool collided with several yeast cells, slightly reducing its velocity. Although the transport of cells by larger catalytic microjets was previously reported in Chapter 6 [23] and by Wang's group [29] the jets utilized here are much smaller, and yet powerful enough to transport cells.

8.2.2. Drilling of fixed Cancer *HeLa* Cells

The corkscrew propulsion was exploited of the nanojets to drill into biomaterials such as those constituting *HeLa* cells, which are an immortal cell line derived from cervical cancer [Dr. W. Xi prepared cells in this experiment].

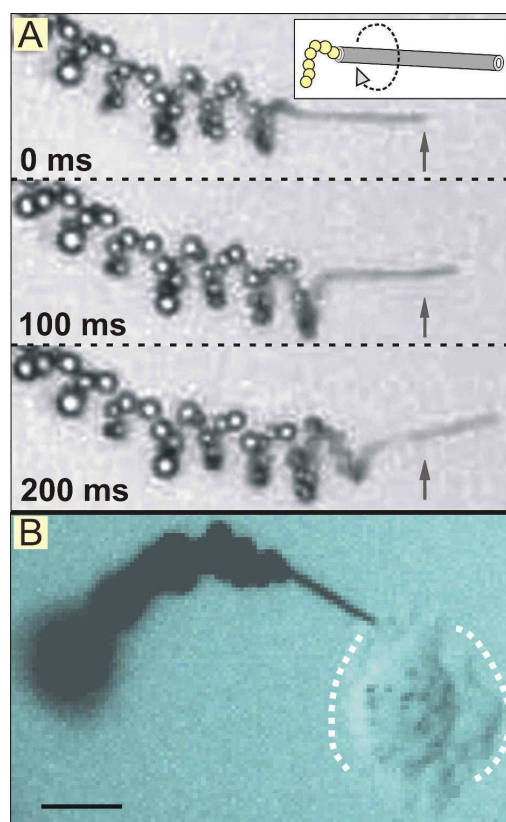Figure 8.5: Cork-like movement of nanotools. (A) Autonomous corkscrew-like motion of a single InGaAs/GaAs/Cr/Pt (3/3/1/1 nm) rolled-up nanotool. Arrows indicate relative motion of the nanojet between panels and the schematic inset shows this type of motion. (B) Optical microscopy image of an active nanotool drilling into a crosslinked biomaterial – a paraformaldehide-fixed *HeLa* cell. Scale bar 10 μm.

It should be noted that paraformaldehyde was utilized to fix the cells prior to the drilling experiments for two reasons: (a) to remove the influence of any chemically induced deformation of the cell during drilling in the H_2O_2 fuel, (b) these fixed cells represent a cross-linked version of a realistic cellular biomaterial, so it was rationalized that if the nanotools could generate enough force to drill into fixed cells, they would likely have more than enough force to drill into uncrosslinked cells. The type of motion needed for drilling is clearly shown in Fig. 8.5 by optical microscope sequences of an individual nanojet which self-propels in a screw-like motion during 200 ms at a rotational frequency of 10 Hz (fuel composition: 20 % v/v H_2O_2, 10 % v/v surfactant). Straight arrows in the images indicate the linear displacement of the nanojet during the studied time. The inset of Fig. 8.5 A depicts a schematic of the rotation of the nanojet during translation. The optical image in Fig. 8.5 B displays a single nanotool which self-propels and embeds itself into a fixed *HeLa* cell.
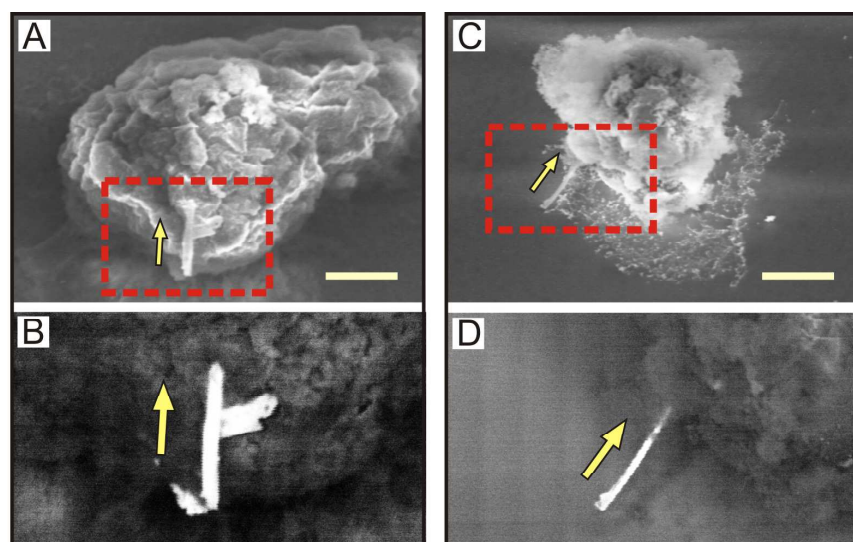
Figure 8.6: Rolled-up nanotool drillers. (A, C) Representative secondary electron SEM images of tubular nanotools which were autonomously embedded into a biomaterial (fixed Hela cells). (B, D) Corresponding backscattered SEM images showing the bright contrast of the embedded nanotool compared to the soft cellular material [Prof. Dr. D. H. Gracias provided these SEM images].

Once the cellular boundary is reached, the nanotools stick to it and start drilling the cellular biomaterial over several minutes. To gain insight into the drilling phenomena, SEM study was performed using a secondary (Fig. 8.6 A, C) and backscatter (Fig. 8.6 B, D) detector which show individual nanotools drilled into *HeLa* cells. The contrast in the back scatter images Fig. 8.6 B and D is due to different atomic masses and allows us to clearly differentiate between the metallic tubes and the paraformaldehyde fixed cells. They show that the metallic nanotools were indeed embedded into these fixed *HeLa* cells. The yellow arrows indicate an initial

direction of nanotools drilling into the cells. We also observed this drilling via optical microscopy and observed that once the nanotools reach the fixed cells, they insert a repetitive motion at a frequency above 40 Hz for the studied fuel conditions. Since a smooth rotational motion was sometimes impeded by the roughness of the object surface, a translational or impulse motion was observed. Subsequently, once bound to the target cell each nanotool asserted this repetitive force over two thousand times a minute which facilitated their penetration inside the fixed cell.

8.3 Summary

In summary, the application of self-propelled catalytic nanojets fabricated by the roll-up of thin films deposited by molecular beam epitaxy was demonstrated. MBE growth of ultra-thin heteroepitaxial layers allows the reduction of the tube diameter down to 280 nm, representing the smallest jet engine reported to date. The particular asymmetry of the tubular structures provides a screw-like motion which was employed for drilling into fixed cells. When a ferromagnetic layer was deposited on top of the rolled-up nanojets, an additional remote control over the motion of such nanotools enabled their directed guidance. Despite the small size, the nanotools are able to pick up and transport multiple yeast cells to desired targets. Although the fuel employed for self-propulsion is still toxic to sustain viable cellular functions, alternative mechanisms of powered motion and working conditions foresee the use of this concept in diverse applications such as biomedical engineering, biosensing and biophysics. While hydrogen peroxide may be acceptable for applications in nanomanufacturing and nanorobotics, biocompatible fuels need to be developed for live-cell applications. Nonetheless, due to the reduced dimensions but yet the high propulsion power, these results suggest strategies of using shape, size and asymmetry of catalytic nanostructures as tools to realize mechanized functions at the nanoscale.

9 Self-Organization of Micro-Jet Engines at the Air-Liquid Interface

Autonomous catalytic Ti/Cr/Pt microjet engines with diameter $5 - 10$ μm, buoyed by oxygen microbubbles, act as catalytic microstriders at the air-liquid interface of the solution fuel. Microengines, buoyed and self-propelled by oxygen bubbles, are attracted to solid edges and islands by the meniscus climbing effect, which is one of the main features found in the behaviour of biological water striders. Scheme 9.1 shows schematic of self organization of microengines into bistable swarm, consisting of multiple microengines. Here, a balance between the microengines attractive capillary and repulsive driving forces sets self-organization of catalytic microjets (parts of this Chapter were adapted from ref. [27]).
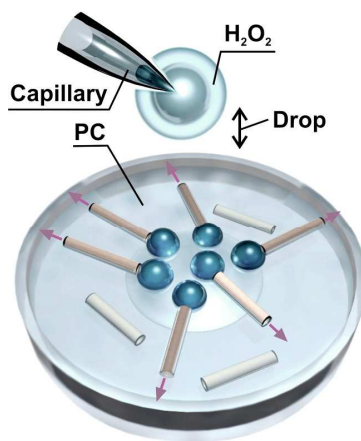
Scheme 9.1: Schematic of microengines activation and self-organization at the solution fuel surface of hydrogen peroxide mixture in propylene carbonate (PC).

9.1 Introduction

Self-organization play a fundamental role in biology, it concerns multiple fundamental functions ranging from molecular proteins and biological cells to multicellular organisms.[167] However, biosystems are difficult to study because of their high complexity. Physical models with dissipation/conversion of energy and simple competing interactions can help both to understand better fundamental principles of self organization and engineer materials and devices with emerging properties, such as more complex micro- and nanomachines.[70, 80, 99, 103, 107] Besides, microscale systems have an advantage that their research does not require any sophisticated methods – all interacting components of such systems can be easy fabricated and simultaneously studied by optical microscopy methods with integrated video camera. One of such systems represent the meniscus-climbing effect, that is well-known for

biological water striders. Striders walk on the surface of water, climb onto solid edges and self-organize into colonies.[105, 168] Furthermore, there is great interest to build artificial water-walking devices.[169, 170, 171] Although static attractive bubbles at the air-liquid interface are well known, to date there has been no report on the use of dynamic bubbles to demonstrate the meniscus-climbing micromachines and their self-organization.

9.2 Results and Discussions

Catalytic microengines consisting of Ti/Cr/Pt layers with diameters of 5 – 10 μm and length of 50 μm were fabricated and used in these experiments. To demonstrate the "strider behaviour" of microengines at the air–liquid interface, a thin aqueous film was created by adding a drop of 30 % v/v H_2O_2 aqueous solution on propylene carbonate (PC), which was intermixed with catalytic microjets. After fuel addition, H_2O_2 diffused into PC [172] and activated/lifted the catalytic microengines to the solution surface due to the buoyancy force of oxygen microbubbles generated by microengines.

Microengines moved at the aqueous surface (air-liquid interface) for minutes until the H_2O_2 fuel was consumed. The microengines position at the fuel surface is explained by a higher acting buoyancy force (microengines considered in Chapters 2–8 were in the H_2O_2 solution with an addition of surfactant. Although buoyancy force in those solutions can be high enough to bring microengines to the air-liquid interface, however it is not strong enough to induce the meniscus climbing effect). Thus, if half of the microengine with a 5 μm diameter and a 50 μm length is full of O_2 gas, the induced buoyancy force is around 5 pN in propylene carbonate (PC) or water. The buoyancy force in PC is 1.2 times larger than that in water. However, the weight of a microengine with the same diameter is around 2.5 pN for the Ti/Cr/Pt (5/5/2 nm in thickness) composition. Since the buoyancy force depends on the gas generated in the microengine, it is possible to derive the filling volume of gas in the microengine. Because PC with a slightly higher density (1.205 g/ml) can lift the microengine but water can not, the buoyancy force in water is smaller than the weight of the tube, but that in PC is bigger. Thus, it can be deduced that the buoyancy force in water and PC should be very close to the weight of 2.5 pN, which is roughly the buoyancy force generated in one quarter of the tube. As a result, the filling volume of gas in the tube is around one quarter of the body volume of our catalytic striders, which is enough to take the microengines to the air–liquid interface.

It was found that catalytic microengines firmly attached to bubbles can attract each other at an aqueous fuel surface and self-organize into colonies due to the meniscus-climbing effect, as sketched in Figure 9.1 A. Bubbles pull attached microengines together and form self-organized structures of microengines (a colony in Figure 9.1 A and a danymic array in Figure 9.1 B). The microengines are well aligned in

certain directions and pile up in abundance (Figure 9.1 B). Once the existed microbubbles break, the microengines separate but sometimes return, depending on the balance between the attractive capillary due to new generated bubbles and repulsive driving forces. Such a balanced system offers an intriguing way to study self-organized systems. By tuning the surface tension of the fuel, the attaching and detaching times of bubbles to and from microengines can be adjusted for a controllable self-organization. For example, one can completely mix PC with H_2O_2 aqueous solution (up to 1:5 v/v) as a fuel since PC is soluble to large extent in water (20 wt %).[172] This mixture still easily powers the micromachines, but the bubbles break immediately after ejection from the microjet ends. Hence, the catalytic microjets run independently at the fuel surface without attraction.
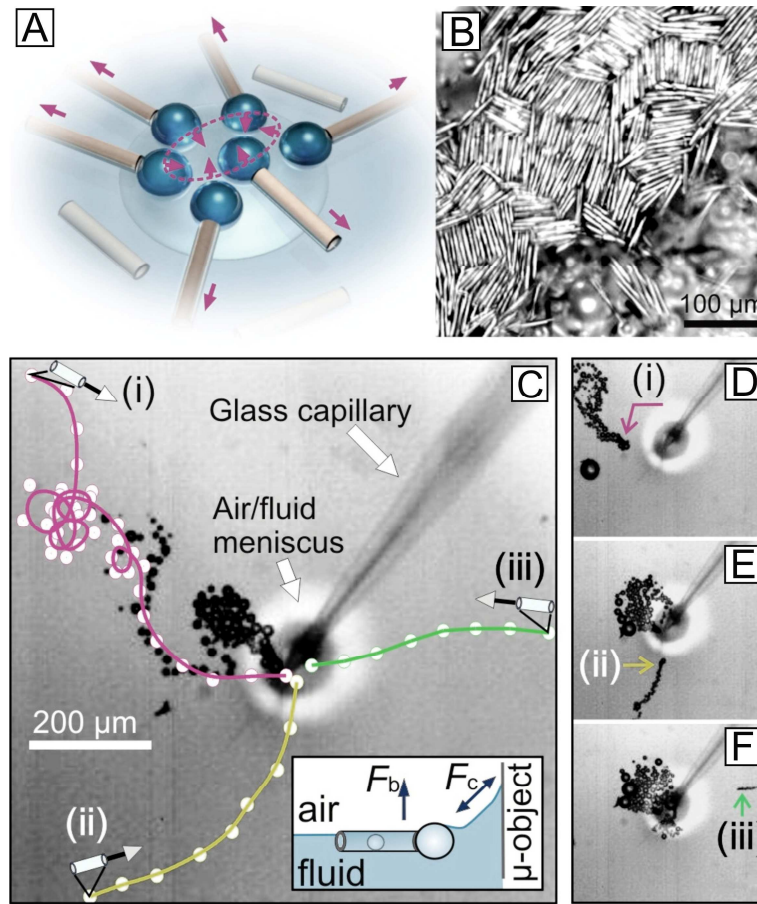
Figure 9.1: (A) Schematic illustration of microjets' meniscus-climbing effect and self-organization. The individual arrows represent the repulsion forces due to the bubble recoiling mechanism, while the arrows within the dashed circle denote the meniscus-climbing effect (attraction), initiated by capillary forces. (B) Optical image of self-organized microtube array, where 100 μl 30 % v/v H_2O_2 fuel was added into 200 μl PC. (C) The Meniscus-climbing microtubes (i-iii) rushing towards a glass capillary. The lines and solid circles show the corresponding trajectories for each microjet. (D-F) Selected video frames for the individual microtubes in (C). The arrows show directions of moving microjets.

It is noticed that with a pure aqueous H_2O_2 solution with surfactants, the catalytic microjet machines run independently in bulk solution but not at the surface.[20] It is deduced that bubbles in PC generate a stronger buoyancy force compared to that in water, and thus drives the catalytic microtubes to the surface, since the density of PC (1.205 g/ml) is higher than that of water.

The attracting capillary force induced by the meniscus-climbing effect was studied by inserting a glass capillary into the surface to anchor the microjets. As displayed in Figure 9.1 C, a glass capillary is inserted into a fuel surface. Several catalytic micromachines moving around previously rush spontaneously towards the capillary at the liquid surface. Individual images for three microjets are shown in Figure 9.1 D–F, which correspond to the tubes (i-iii) shown in Figure 9.1 C, respectively. As schematically shown in the inset of Figure 9.1 C, a generated bubble with a connected tube is pulled towards a micro-object (here glass capillary) by the capillary force (F_c), while the buoyancy force (F_b) from the bubbles lifts the microjet to the fluid surface. Such a landing or climbing behavior of our artificial micromachines is similar to that of water-walking insects like *Mesovelia*, *Hydrometra* and the *Beetle larva*.[105] In addition, we described the blocking effect of catalytic engines by bubbles in ref. [20] It can also support the self-organization of microjets by ceasing the catalytic reaction. In this case closely packed microengines can decrease their fuel supply, leading to closely packed assembly shown in Figure 9.1 B.

9.2.1. Analysis of Dynamic Colonies

The capillary force among water-walking insects enables them to attract each other and to self-organize into a colony,[173] which is similar to the behaviour of catalytic microjets. Interestingly, the self organizaiton of microjets reveal a dynamic characteristic, which mainly depends on the fuel concentrations. As shown in the top image of Figure 9.2 A, several catalytic micromachines have gathered into a colony after adding a drop of H_2O_2 solution. The resultant trajectories of several microjets within one second are shown in the bottom image of Figure 9.2 A. However, after several seconds these powered catalytic microjets disassemble due to their reduced power since the fuel is being consumed. As revealed in Figure 9.2 B, the micromachines are dispersed in 10 seconds after Figure 9.2 A is recorded. The gradual separation of all microtubes is revealed by their trajectories (bottom image of Figure 9.2 B). The tubes do not aggregate again until fuel is refilled by an addition of a new droplet of hydrogen peroxide. It is noted that as long as sufficient fuel is provided, a cyclic behaviour was observed of self-assembly and self-disassembly of the catalytic microjet engines. A statistical analysis of the disassembly behaviour described above was carried out. Figure 9.3 A shows examples of microjets self-organization when a droplet of hydrogen peroxide was added locally and diffuses into bulk PC solution.
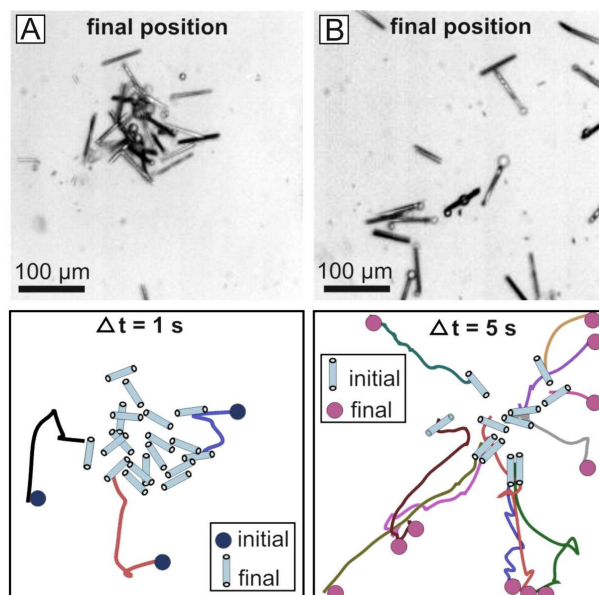
Figure 9.2: (A) Top, optical image of self-organizing microjets into a colony after adding a drop of the hydrogen peroxide solution (20 µl 30 % v/v H_2O_2) into 100 µl PC. Bottom, recorded trajectories leading to the top image within one second. (B) Top, optical image of powered catalytic microjets dis-assembled after several seconds. Bottom, recorded trajectories leading to the top image within five seconds. Notice that the final position in (A) is not the initial position in (B). There are several seconds between (A) and (B) without recording.
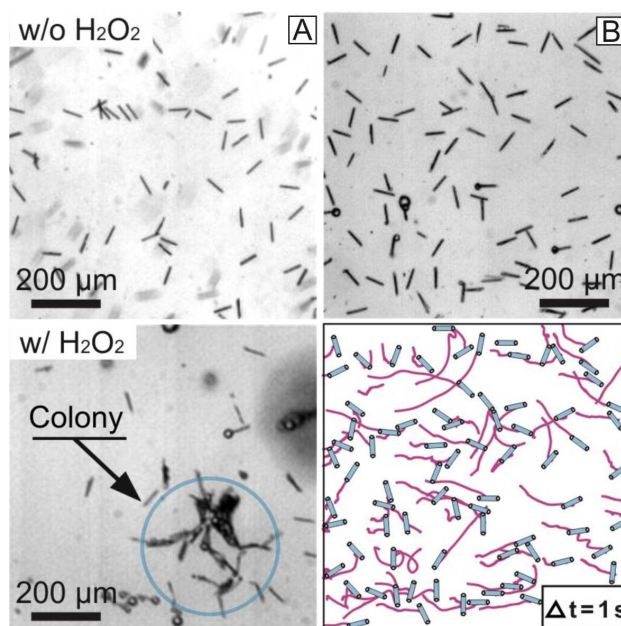
Figure 9.3: (A) Top, optical image of propylene carbonate (PC) liquid containing rolled-up microtubes. Most of them are sitting at the bottom due to sedimentation. Bottom, optical image of powered catalytic microjets organizing into a colony (blue circle) after adding a drop of hydrogen peroxide solution (20 µl 30% H_2O_2) into 100 µl PC. (B) Top, optical image of catalytic microtubes moving independently at the surface of the mixed PC/H_2O_2 (v/v 5/2) solution. Bottom, the resultant trajectories starting from the top image within one second reveal no attraction effect.

One-second videos were chosen when the microjets change from the self-organized state to the dispersed one. In contrary, microjets in the mixture of peroxide with PC did not self-organize. The average bubble radius as a function of time is shown in Figure 9.4 A. The bubble radius reduces with time, while the micromachines separate more and more (sketched in the insets). Basically, two major conditions influence the bubble size. One is the fuel concentration, where higher concentrations lead to smaller bubbles.[20] The other is the surface tension of the fluid. The micromachine velocity was tested in a constant H_2O_2 concentration but with various ratios of water in PC (fully mixed), which slightly changes the surface tension.[174] As presented in Figure 9.4 B, the bubble radius becomes smaller when decreasing the ratio of water in PC, while the micromachine velocity increases even with a constant fuel concentration. Hence, one can explain why powered catalytic microtubes disassemble with time in the case of adding a drop of H_2O_2.
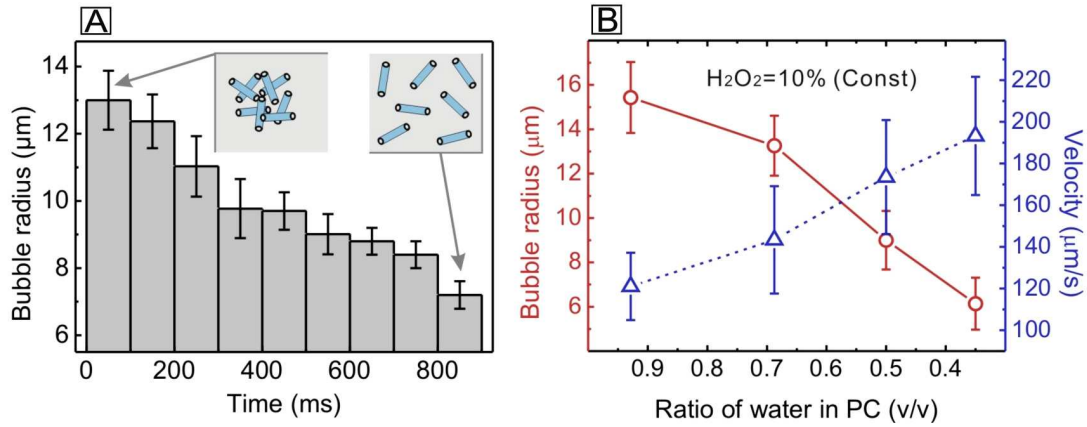
Figure 9.4: (A) Bubble radius as a function of time. The data is taken from the video, which corresponds to Fig. 9.3 A. The insets sketch the self-organization and disassembly behaviors of the microengines for the indicated time. (B) Bubble radius and velocity of catalytic microengines as a function of ratio of water in PC (v/v) at a constant concentration of H_2O_2 (10%).

When the tubes become disperse, the bubble radius reduces (Figure 9.4 A) and thus the attracting force decreases. However, the velocity still could rise due to the evaporation of water because of Figure 9.4 B, which means the drag force responsible for dispersion is enhanced. Therefore, the micromachines disassemble with time.

9.2.2. Dynamics of Individual Microengines

The velocity and bubble size play a critical role for the assembly of microjets. As shown in Figure 9.5 A, three typical microjet engines are selected for analysis with bubble sizes of around 5, 12, 21 μm (microtube #1, #2, and #3, respectively). Connected circles in Figure 9.5 A mark their trajectories, #1 moves away from the huge central bubble, #2 moves in a dynamic equilibrium, while #3 runs towards the big

bubble. This observation confirms the explanation of Figure 9.4, where small bubbles tend to lead to disassembly behaviour. Further analysis in Figure 9.5 B and C discloses the kinematic characteristics of the three microjets including travelling distance and velocity with time. The distance and velocity along a trajectory away from (towards) the huge central bubble are treated as a positive (negative) value. The micromachine #1 generating small bubbles (below 5 μm) runs away from the huge central bubble, which is indicated by a positive and increasing travel distance (B) as well as a positive velocity (C). The micromachine #3 with big bubbles (21 μm) is rushing into the huge central bubble, which is reflected by a negative and increasing travel distance as well as a negative velocity.
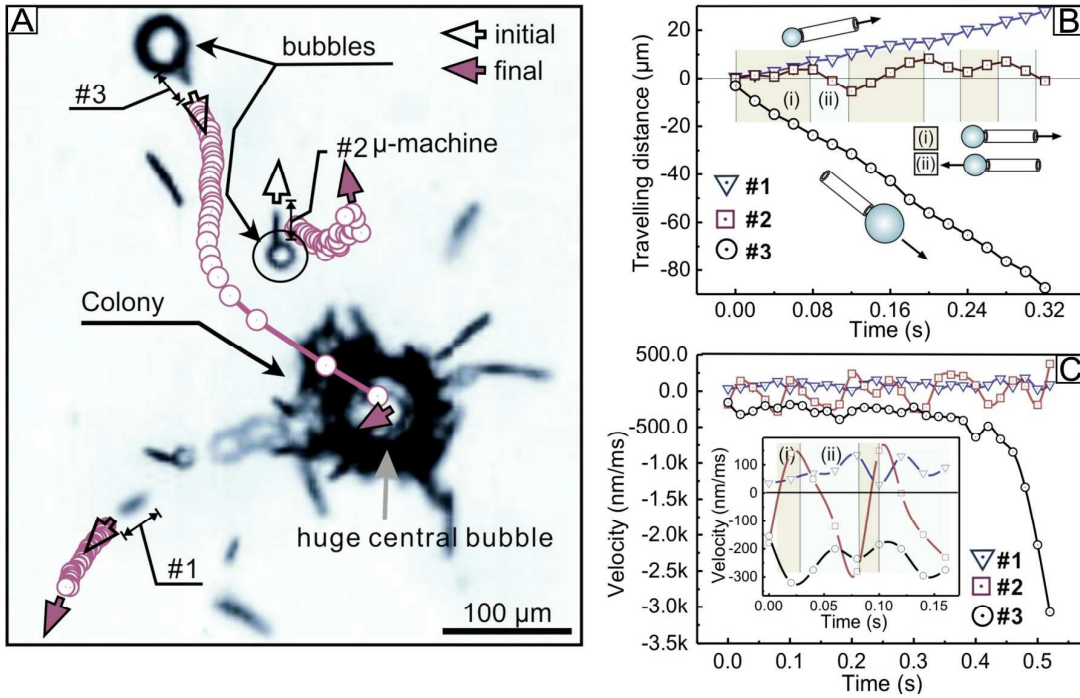
Figure 9.5: Analysis of individual microjets at the air-liquid interface interacting with a colony containing one big bubble. (A) Optical image showing dynamics of three microengines (#1, #2, and #3), where #1 is leaving away from the bubble and colony; #2 is in oscillating state; while #3 is running to the bubble. Kinematics: (B) travelling distance and (C) velocity with time of three individual microengines.

The micromachine #2 with mediate bubbles (12 μm) finds itself in a oscillating state, and walks forth [labelled as (i)] and back (ii) for several times. This effect is generated by the balance between the attractive capillary and repulsive motive forces. Generally, water striders in nature can attract neighbours over a distance comparable to the capillary length.[173] Grzybowski group have described a two-spheres system (with center-to-center distance L) with a capillary force $F_c \propto \gamma R^2/L$ (explained in details in Chapter 1), where γ is the surface tension of the applied liquid

and R is the radii of the spheres.[99] So the attractive capillary force increases with the radii of the spheres. If this principle is applied to the considered system, big bubbles (with bigger radii) can supply a higher capillary force for attraction and small ones produce a relatively weak force. The driving force of microengines is due to continuously generated microbubbles with a certain frequency and size. However an attraction originates from the generated bubbles connected to a microengine. The connection time between the bubbles and microengines is relatively short (maximum estimated tens of milliseconds) for bubbles in mixture of hydrogen peroxide and propylene carbonate. Thus, as long as the generated bubbles are connected to microengines they attract them, but when bubbles break away, the attraction ceases and striders move apart. Hence, if the driving force is higher than the weak attraction force between small bubbles, the microengines move away from the positive menisci curvature created by a glass capillary. The attraction force leads to capture of the catalytic microengines. Based on the equation of lateral capillary force, one could deduce that the capillary force (i.e. attraction force) reduces with the decrease of the bubble size.[99] The striders in the same system have similar driving force, but smaller bubbles lead to a weaker capillary attraction force compared to the driving force.
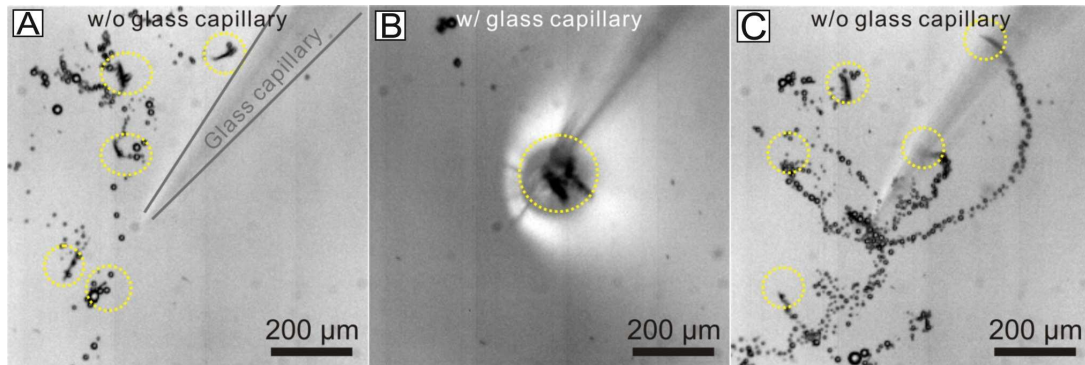
Figure 9.6: A reproducible demonstration of the meniscus-climbing microtubes (highlighted by yellow circles) rushing towards a glass capillary. (A) The microengines move randomly at the air-liquid interface without the glass capillary. (B) The microengines attached to the immersed glass capillary; microjets are highlighted by the dashed yellow circles. (C) Once the glass capillary is removed, the microjets run away in random directions.

Hence, the striders with smaller bubbles leave the glass capillary, which is exactly the behaviour of the #1 microjet in Figure 9.5. Moreover, a micro-object was introduced to replace the huge central bubble as shown in Figure 9.6. The catalytic micromachines can still move around and climb "attacking" the defined object at the fuel-air interface, which thus strengthens the above interpretation. A reproducible demonstration of the meniscus-climbing effect has also been revealed. At first the glass capillary is positioned above the liquid surface, and random motion of the catalytic microengines (highlighted by yellow circles) is observed in Figure 9.6 A. Once

the glass capillary is immersed into the liquid fuel, the microengines run towards the capillary and attach to it (Figure 9.6 B). The black area in the center (close to the capillary tip, highlighted by yellow circles) is populated by the attached microjets. When the capillary tip is removed from the liquid, all striders (highlighted by yellow circles) still stay at the air–liquid interface but move away randomly. The bubble tails reveal their trajectories. This demonstration has been reproduced six times and proves the concept of catalytic microstriders at the air–liquid interface.
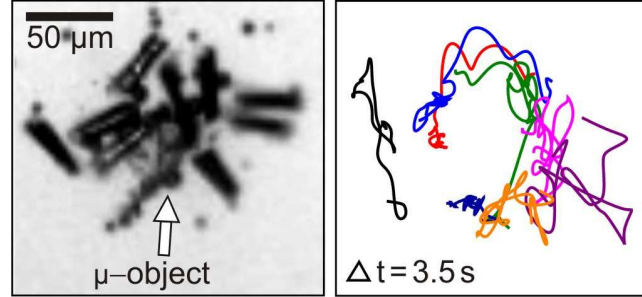

Figure 9.7: Microengines attraction to a microscale object. Left, optical image of catalytic microstriders moving around and climbing on the microobject. Right, tracked trajectories of the microengines during 3.5 s.

Figure 9.7 shows additional experiment, on the left side of Fig. 9.7 optical microscopy image of several microjets "attacking" microobject is shown. Microobject is located at the air-liquid interface. Figure 9.7 on the right demonstrates tracked trajectories of microjets motion during 3.5 seconds, indicating that microengines stay near boundaries of the microobject.

9.3 Summary

Microjet-based water striders and their self-organization was well demonstrated due to low weight of catalytic microtubes in solution and high buoyancy force, which brings them to the air-liquid interface. When capillary interaction between microengines overlaps and exceeds the driving force of microengines they self-organize into colonies or swarms. If local peroxide fuel/water diffuses into bulk solution of propylene carbonate it leads to a decrease of an average bubble size, generated by microengines, and subsequently, to the decrease of capillary attraction. In this case microengines are dispersed and self-propelled independently. Immersed microcapillary allows in some way a "fishing" of microengines as they rush immediately towards the capillary. This principle can be used for micromachines climbing onto objects. Besides, it is of interest for future studies to investigate how microengines can repel and avoid objects, e.g., if negative meniscus or hydrophobic objects are used.

In conclusion, Table 6.1 shows several examples of self organized systems in comparison to microjet engines. These examples show particles which form spatio-

temporal patterns in space. These patterns depend on the supply or conversion of energy. Examples shown in Table 6.1 include: a) autonomous millimeter-scale Pt-boats in the solution of hydrogen peroxide.[80]; b) magnetic millimeter-scale spinners, which form dynamic patterns controlled by the frequency of external magnetic field (ω) [175]; c) light-driven AgCl particles swarming in water, induced by light [142]; d) autonomous nanorotors in solution of hydrogen peroxide [176]; e) biological species *Anurida* which form colonies [177], f) catalytic microjets, demonstrated throughout this dissertation. Interestingly, both biological species (e) which can be considered as "complex machines" and microjets which are "simple machines" (f) self-organized by the same meniscus-climbing effect. In future studies it will be of high interest to consider other energy sources and interactions to engineer self-organized systems.
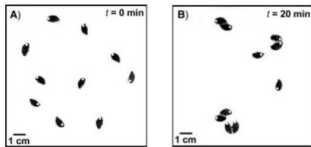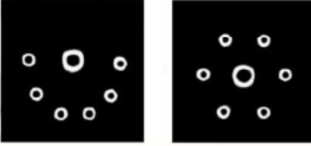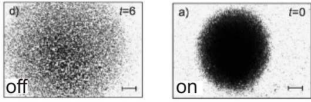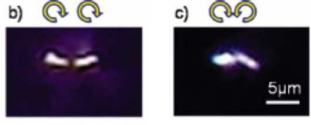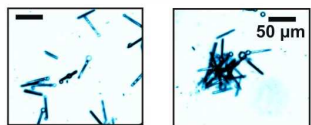
Self-Organized patterns	Key components (and interaction)	Fuel source
(a)	PDMS Boat (Hydrophobic-hydrophilic, meniscus effect)	Chemical molecules (hydrogen peroxide)
(b)	Magnetic disk (magnetic and fluid shear)	Magnetic field
(c)	Ag/Cl Micromotor (diffusiophoresis)	Light, temperature
(d)	Cr/SiO$_2$/Cr/Au/Pt Nanorotor (fluid shear)	Chemical molecules (hydrogen peroxide)
(e)	*Anurida* insect (meniscus effect)	Chemical molecules (complex composition)
(f)	Ti/Cr/Pt Microjet engine (meniscus effect)	Chemical molecules (hydrogen peroxide)

Table 9.1: Examples of self-organization of different objects. Synthetic components (a-d, f) and biological water-striders (e). Microjets (f) use meniscus-climbing effect similar to *Anurida* (e). Inset images (a, b, c, d, e) are copied from the corresponding refs. [80, 175, 142, 176, 177]. Note that light, temperature or magnetic field is not really a "fuel source" of patterns. It changes interactions between particles and the formation of patterns depends on it.

10 Outlook

This dissertation showed effective catalytic microjet engines, methods of their remote control and applications towards specific tasks. Some of goals require biocompatible fuels, e.g. nanomachines enabled fight with cancer *in vivo*. It is expected that when more "intelligent" micromachines are created we will be able to solve human problems not only at the small scale but at global one. Several ultimate goals and preliminary results of what can be done next are discussed in the following pages.

Can microjets be more efficient and powerful?

It was shown that microjets require a certain threshold concentration of hydrogen peroxide fuel (0.05 % v/v H_2O_2) at room temperature. Estimated energy conversion efficiency of microjet engines is on the order of 10^{-10} %, it is comparable to values calculated by Paxton for catalytic nanomotors.[86] In contrast, biological nanomotors efficiency is often higher than 50 % due to their ability to couple motions of molecular architectures with the transport of single ions or fuel molecules. Firstly, this principle can be used in the design of future microengines. Secondly, better understanding of reaction and diffusion processes at the microscale can lead to more efficient microjets. It is proposed to design a microjet with smaller tubular openings than the diameter of the body of an engine. This geometry can restrict the fast diffusion of reaction products (oxygen) out of the tubular openings and provide an accumulation, i.e., nucleation of bubbles at a lower concentration level of hydrogen peroxide. Alternatively, a higher power/speed of microjets was already demonstrated by increasing the temperature of working solution to physiological values.[48]

Can technology lead to smaller microjets?

It was found that only 1 nm of Pt-catalyst is enough for nanoengines to operate and thus, it is feasible to fabricate even smaller nanojets. Rolled-up nanotechnology allows the reduction of diameter of heteroepitaxial tubes to 20 nm.[33] However, it is unlikely that such nanojets can be driven by nanobubbles because of bubbles instabilities at a smaller size, i.e., due to a very high Laplace pressure. In this case other motive mechanisms have to be found, for instance, reactions of polymerization used by the nanojet driven bacteria.

Can more complex "intelligent" micromachines be made of microjets?

It is of high interest to build more complex micromachines to increase machines' functionalities. At the moment microjets can be considered as "simple machines". One way to create more complex machines consists in the integration of other functional units with microjets, illustrated in Fig. 10.1 A (for details see ref. [32]). In this approach other machine's parts can be miniaturized and integrated, such as actuators, sensors, computer controllers, logic, battery, antenna. These units are currently under development in our group. On the other hand, it is interesting to consider that several processes which take place, such as the interplay between the reaction and diffusion,

conversion of chemical energy into movement are used by both: biological systems and microjet engines.

Can microjets sense chemical gradients?

Chemotactic behaviour is widespread in nature and consists in the complex ability of biological organisms to orient in chemical gradients and particularly, to find their source of food. Sen's group reported about non-biological chemotaxis of electrophoretic Au/Pt nanomotors. These nanomotors elongate their trajectories of motion when they approached a higher concentration of the hydrogen peroxide fuel, i.e., nanorods were "attracted" to the hydrogen peroxide soaked gel by the active diffusion mechanism.[78] It is important to note that it does present a real biological chemotaxis, but this observation can have important practical applications. However, the power of the former nanomotors was too low, particularly, nanomotors required many hours to reach their target. Since microjets are in two orders of magnitude faster than electrophoretic nanomotors it is of high interest to find conditions for chemotaxis of microjets. Fig. 10.1 B shows schematic of the desired goal, where individual microjet is "attracted" towards a pathogen, while carrying drugs along with it to support "friendly cells".

Can microjets self-propel without µ-bubbles?

Propulsion of microjets without bubbles are important for biomedical and on-chip applications. Fig. 10.1 C shows preliminary result of one individual microjet (yellow line shows tracked trajectory) moving without bubbles in the mixture of hydrogen peroxide and propylene carbonate. The propulsion speed is as high as 200 μms^{-1}, that is comparable to the fastest electrophoretic nanomotors. At the moment it is not clear what is the mechanism of motion. Future studies will determine its origin, that is expected to be self-electrophoresis or self-diffusiophoresis.

Can microjets self-propel in environments other than fluid ones?

It was demonstrated that microjets can self-propel only in fluids. Although foam contains fluid, it is a mixture of gas and a fluid. Fig. 10.1 D shows preliminary results of individual microjet moving through a dense foam of bubbles, which are composed of hydrogen peroxide, water and amphiphilic soap molecules. Interestingly, such microjets are not blocked by bubbles and they are able to move through the foams and even can be remote controlled using magnetic field (not shown). This study may help in the design of microjets which can travel at high speeds in 3-d foams or overcome clogged channels in microfluidic devices.

Can microjets be useful in medicine?

Minimally invasive medicine based on dynamic micro- and nanomachines (rather than medicine based on static nanoobjects/drugs) can advance the field of medicine. Recently the group of Gracias showed enzymatically-triggered and tetherless thermobiochemically actuation of miniaturized grippers and tools.[178, 179, 180]. Nelson discussed recent advantages of microbots with a small size, which can adopted in the near future for a possible medical use in the circulatory, the urinary and the cen-

tral nervous systems.[181] Particularly, to operate in body the size of machines must be smaller than the diameter of capillaries of the cardiovascular system, which can be as small as 8 μm. The rolled-up nanotechnology allowed the fabrication of such small tubes. At the moment an application of micro- and nanojets in medicine requires the development of biocompatible fuels. As alternative to this we performed a "fuel free" motion and drilling of animal liver by microtubes *in vitro*, shown in Fig. 10.1 E. In this experiment by increasing the frequency of the magnetic field microtubes changed their rotation from the planar to the vertical position, i.e., they can stand up on the surface and walk towards the center of rotational magnetic field. Figs. 10.1 E inset shows optical microscopy sequences and SEM image (i) of the embedded microtube in the liver tissue and the hole left (ii) after the microtube was removed (SEM images were taken by Dr. W. Xi and Prof. Dr. D.H. Gracias).
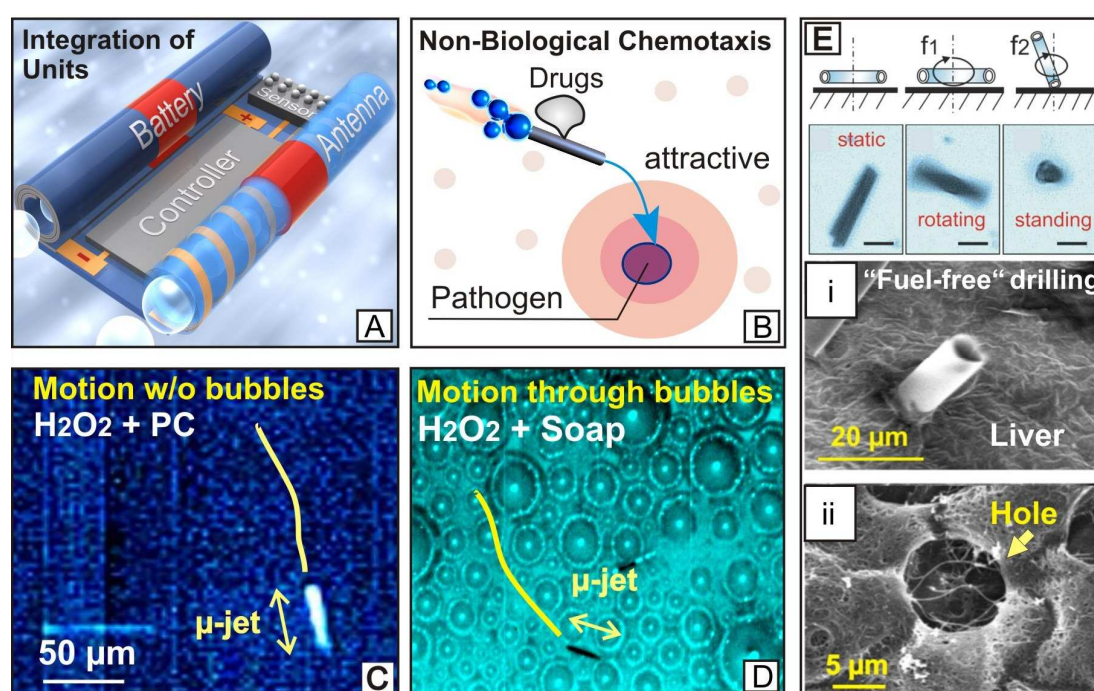
Figure 10.1: Outlook and several promising results of microjet engines (A) Schematic design of a more complex micromachine, where tweens–microjets can be integrated with other functional units, described in details in ref. [32]. (B) Schematic of the desirable experiment of non-biological chemotaxis of catalytic microjet engines, which could attract towards pathogens, while delivering drugs to "friendly cells". (C) Preliminary result, optical microscopy image showing motion of microjet without bubbles. (D) Preliminary result, optical microscopy image of motion of microjet through foam, consisting of bubbles. (E) Preliminary result of the fuel-free propulsion of magnetic microjets, driven by external magnetic field to drill liver tissue *in vitro*. Tubes rotate at a lower frequency (f_1) and start drilling tissue at a higher frequency (f_2) of magnetic field. SEM images (i-ii) showing individual embedded microtube in the liver and the hole left after the microtube was removed (experiment of liver drilling *in vitro* was done in collaboration with Dr. W. Xi, Dr. S. Sanchez and Prof. Dr. D. H. Gracias).

Bibliography

[1] R. P. Feynman. There is a Plenty of Room at the Bottom. *Eng. Sci.*, **23**, 22 (1960).

[2] Definition of the "Hydrogen Peroxide Fuel", source: *wikipedia.com*

[3] Engine on a Chip and Turbine Engine History, source: *thefutureofthings.com*

[4] E. M. Purcell, Life at Low Reynolds Number, *Am. J. Phys.*, **45**, 3 (1977).

[5] C. Wolgemuth, E. Hoiczyk, D. Kaiser, G. Oster. How Myxobacteria Glide. *Curr. Biol.*, **12**, 369–377 (2002).

[6] J. M. Y. Carrillo, J.H. Jeon, A. V. Dobrynin. A Model of Polymeric Nanopropulsion Engine. *Macromolecules*, **40**, 14, 5171–5175 (2007).

[7] M. G. L. van den Heuvel, C. Dekker. Motor Proteins at Work for Nanotechnology. *Science*, **317**, 5836, 333–336 (2007).

[8] A. Goel, V. Vogl. Harnessing Biological Motors to engineer Systems for Nanoscale Transport and Assembly. *Nat. Nanotech.*, **3**, 465–475 (2008).

[9] T. Mirkovic, N. S. Zacharia, G. D. Scholes, G. A. Ozin. Fuel for Thought: Chemically Powered Nanomotors Out-Swim Nature's Flagellated Bacteria. *ACS Nano*, **I**, 4, 1782–1789 (2010).

[10] J. Wang, K. M. Manesh. Motion Control at the Nanoscale. *Small*, **6**, 3, 338–345 (2010).

[11] W. F. Paxton, K. C. Kistler, C. C. Olmeda, A. Sen, S. K. St. Angelo, Y. Cao, T. E. Mallouk, P. E. Lammert, V. H. Crespi. Catalytic Nanomotors: Autonomous Movement of Striped Nanorods. *J. Am. Chem. Soc.,* **126**, 13424 (2004).

[12] G. A. Ozin, I. Manners, S. Fournier-Bidoz, A. Arsenault. Dream Nanomachines. *Adv. Mater.*, **17**, 3011–3018 (2005).

[13] W. R. Browne, B. L. Feringa. Making Molecular Machines Work. *Nat. Nanotech.*, **1**, 25 (2006).

[14] H. C. Berg, Motile Behavior of Bacteria. *Physics Today*, **53,** 1, 24–29 (2000).

[15] S. Sundararajan, P. E. Lammert, A. W. Zudans, V. H. Crespi, A. Sen. Catalytic Motors for Transport of Colloidal Cargo. *Nano Lett.*, **8**, 5, 1271–1276 (2008).

[16] J. Wang. Can Man-made Nanomachines Compete with Natural Biomotors? *ACS Nano*, **3**, 1, 4–9 (2009).

[17] E. R. Kay, D. A. Leigh, F. Zerbetto. Synthetic Molecular Motors and Mechanical Machines. *Angew. Chem. Int. Ed.*, **46**, 72–191 (2007).

[18] G. M. Whitesides. The Once and Future Nanomachine. *Scientific American* (09.2001)

[19] R. B. Vallee, P. Höök. Molecular Motors: A Magnificent Machine. *Nature*, **421**, 701 (2003).

[20] A. A. Solovev, Y. F. Mei, E. Bermúdez Ureña, G. S. Huang, O. G. Schmidt. Catalytic Microtubular Jet Engines Self-Propelled by Accumulated Gas Bubbles, *Small*, **5**, 14, 1688–1692 (2009).

[21] A. A. Solovev, Samuel Sanchez, Yongfeng Mei, Oliver G. Schmidt. Tunable Catalytic Tubular Micro-Pumps Operating at Low Concentrations of Hydrogen Peroxide. *Phys. Chem. Chem. Phys.*, **13**, 10131–10135 (2011).

[22] T. R. Kline, W. F. Paxton, T. E. Mallouk, A. Sen. Catalytic Nanomotors: Remote-Controlled Autonomous Movement of Striped Metallic Nanorods. *Angew. Chem. Int. Ed.*, **44**, 744–746 (2005).

[23] A. A. Solovev, S. Sanchez, M. Pumera, Y. F. Mei, O. G. Schmidt. Magnetic Control of Tubular Catalytic Microbots for the Transport, Assembly and Delivery of Micro-objects. *Adv. Func. Mater.*, **20**, 15, 2430–2435 (2010).

[24] S. Sanchez, A. A. Solovev, S. Schulze, O. G. Schmidt. Controlled Manipulation of Multiple Cells using Catalytic Microbots, *Chem. Comm.*, **47**, 698 (2011).

[25] A. A. Solovev, E. Smith, C. C. Bof Bufon, S. Sanchez, O. G. Schmidt. Light Controlled Propulsion of Catalytic Microengines. *Ang. Chem. Int. Ed.,* **50** (46), 10875–10878 (2011).

[26] A. A. Solovev, W. Xi, D. H. Gracias, S. Harazim, C. Deneke, S. Sanchez, O. G. Schmidt. Self-Propelled Nanotools. *ACS Nano*, online: DOI: 10.1021/nn204762w

[27] A. A. Solovev, Y. F. Mei, O. G. Schmidt. Catalytic Microstrider at the Air–Liquid Interface. *Adv. Mater.,* **22**, 39, 4340–4344, (2010).

[28] D. Kagan, S. Campuzano, S. Balasubramanian, F. Kuralay, G.-U. Flechsig, J.Wang. Functionalized Micromachines for Selective and Rapid Isolation of Nucleic Acid Targets from Complex Samples. *Nano Lett.*, **11** (5), 2083–2087 (2011).

[29] S. Balasubramanian, D. Kagan, C.-M. Jack Hu, S. Campuzano, M. J. Lobo-Castañon, N. Lim, D. Y. Kang, M. Zimmerman, L. Zhang, J. Wang. Micro-machine-Enabled Capture and Isolation of Cancer Cells in Complex Media. *Ang. Chem. Int. Ed.,* **50**, 18, 4161–4164 (2011).

[30] S. Campuzano, J. Orozco, D. Kagan, M. Guix, W. Gao, S. Sattayasamitsathit, J. C. Claussen, A. Merkoçi, J. Wang. Bacterial Isolation by Lectin-Modified Microengines. *Nano Lett.*, **12** (1), 396–401 (2012).

[31] Y. F. Mei, G. Huang, A. A. Solovev, E. Bermüdez Ureña, I. Mönch, F. Ding, T. Reindl, R. K. Y. Fu, P. K. Chu, O. G. Schmidt. Versatile Approach for Integrative and Functionalized Tubes by Strain Engineering of Nanomembranes on Polymers. *Adv. Mater.*, **20**, 4085–4090 (2008).

[32] Y. F. Mei, A. A. Solovev, S. Sanchez, O. G. Schmidt. Rolled-up Nanotech on Polymers: From Basic Perception to Self-Propelled Catalytic Microengines. *Chem. Soc. Rev.*, **40**, 2109–2119 (2011).

[33] C. Deneke, C. Müller, N. Y. Jin-Phillipp, O. G. Schmidt. Diameter Scalability of Rolled-up In(Ga)As/GaAs Nanotubes. *Semicond. Sci. Technol.*, **17**, 1278 (2002).

[34] E. B. Ureńa, Y. F. Mei, E. Coric, D. Makarov, M. Albrecht, O. G. Schmidt. Fabrication of Ferromagnetic Rolled-up Microtubes for Magnetic Sensors on Fluids. *J. Phys. D: Appl. Phys.*, **42**, 055001 (2009).

[35] H. Ji, Y. F. Mei, O. G. Schmidt. Swill Roll Nanomembranes with Controlled Proton Diffusion as Redox Micro-Supercapacitors. *Chem. Commun.*, **46**, 3881–3883 (2010).

[36] G. S. Huang, S. Kiravittaya, V. A. Bolańos Quińones, F. Ding, M. Benyoucef, A. Rastelli, Y. F. Mei, O. G. Schmidt. Optical Properties of Rolled up Tubular Microcavities from Shaped Nanomembranes. *Appl. Phys. Lett.*, **94**, 141901 (2009).

[37] G. S. Huang, Y. F. Mei, D. J. Thurmer, E. Coric, O. G. Schmidt. Rolled up Transparent Microtubes as Two Dimensionally Confined Culture Scaffolds of Individual Yeast Cells. *Lab Chip*, **9**, 263–268 (2009).

[38] U. Vogl, A. A. Solovev, A. Sass, Y. F. Mei, O. G. Schmidt, M. Weitz. Light Confinement by a Cylindrical Metallic Waveguides in a Dence Buffer Gas Environment. *Phys. Rev. A,* **83**, 053403 (2011).

[39] G. M. Whitesides. The Origins and the Future of Microfluidics. *Nature*, **442**, 368 (2006).

[40] T. R. Kline, W. F. Paxton, Y. Wang, D. Velegol, T. E. Mallouk, and A. Sen. Catalytic Micropumps: Microscopic Convective Fluid Flow and Pattern Formation. *J. Am. Chem. Soc.*, **127**, 17150–17151 (2005).

[41] S. Sanchez, A. A. Solovev, Y. F. Mei, O. G. Schmidt. Dynamics of Biocatalytic Microengines Mediated by Variable Friction Control. *J. Am. Chem. Soc.*, **132,** 38, 13144–13145 (2010).

[42] S. Sanchez, A. A. Solovev, S. Harazim, O. G. Schmidt. Microbots Swimming in the Flowing Streams of Microfluidic Channels. *J. Am. Chem. Soc.*, **133**, 4, 701–703 (2011).

[43] J. G. Gibbs, Y. Zhao. Self-Organized Multiconstituent Catalytic Nanomotors. *Small*, **6**, 15, (2010).

[44] Definition of Swimming Speeds: blue whale, copepod, man; the source: *wikipedia.com*

[45] P. Tabeling. Introduction to Microfluidics. *Oxford University Press* (2005).

[46] B. R. Munson, D. F. Young, T. H. Okiishi, W. W. Huebsch. Fundamentals of Fluid Mechanics. *Sixth Ed.*, *Wiley* (2010).

[47] R. W. Fox, P. J. Pritchard, A. T. Mcdonald. Introduction to Fluid Mechanics. *Seventh Ed., Wiley* (2010).

[48] S. Sanchez, A. N. Ananth, V. M. Fomin, M. Viehrig, O. G. Schmidt. Superfast Motion of Catalytic Microjet Engines at Physiological Temperature. *J. Am. Chem. Soc.*, **133** (38), 14860–14863 (2011)

[49] W. Gao, S. Sattayasamitsathit, J. Wang. Catalytically propelled micro-/nanomotors: how fast can they move? *The Chemical Records*. DOI: 10.1002/tcr.201100031

[50] M. Schliwa, G. Woehlke. Molecular Motors. *Nature*, **422**, 759 (2003)

[51] C. W. Wolgemuth, G. Oster. The Junctional Pore Complex and The Propulsion of Bacterial Cells. *J. Mol. Microbiol. Biotech*, **7**, 72–77 (2004).

[52] M. Sanders, J. A. Theriot. Tails from the Hall of Infection: Actin based Motility of Pathogens, *Trends in Microbiology*, **4**, 6, 211–213 (1996).

[53] S. C. Kuo, J. L. Mcgrath. Steps and Fluctuations of Listeria Monocytogenes during Actin-based Motility. *Nature*, **407**, 1026 (2000).

[54] M. B. Goldberg. Actin-Based Motility of Intracellular Microbial Pathogens. *Microbiol. Molec. Biol. Rev.*, **65,** 4**,** 595–626 (2001).

[55] A. Mogilner, G. Oster. Force Generation by Actin Polymerization II: The Elastic Ratchet and Tethered Filaments. *Biophys. J.*, **84**, 1591–1605 (2003).

[56] J. Jeon, A. V. Dobrynin. Polymer Confinement and Bacterial Gliding Motility. *Eur. Phys. J. E*, **17**, 361–372 (2005).

[57] H. C. Berg. The Rotary Motor of Bacterial Flagella. *Annu. Rev. Biochem*., **72**, 19 (2003).

[58] S. C. Schuster, S. Khan. The Bacterial Flagellar Motor. *Annu. Rev. Biophys. Biomol. Struct*., **23**, 509–539 (1994).

[59] T. Atsumi L. McCartert, Y. Imae. Polar and lateral flagellar motors of marine Vibrio are driven by different ion-motive forces. *Nature,* **355**, 182–184 (1992).

[60] H. Wada, R. Netz. Hydrodynamics of Helical-Shaped Bacterial Motility. *Phys. Rev. E*, **80**, 021921 (2009).

[61] D. B. Hill, V. Swaminathan, A. Estes, J. Cribb, E. T. O'Brien. Force Generation and Dynamics of Individual Cilia under External Loading. *Biophys. J*., **98**. 57–66 (2010).

[62] A. R. McNeill. The Invertebrates. London*, Cambridge University Press* (1979).

[63] K. Kinbara, T. Aida. Toward Intelligent Molecular Machines: Directed Motions of Biological and Artificial Molecules and Assemblies. *Chem. Rev.*, **105**, 1377–1400 (2005).

[64] K. J. Böhm, R. Stracke, P. Mühlig, E. Unger. Motorprotein-Driven Unidirectional Transport of Micrometer-Sized Cargoes Across Isopolar Microtubule Arrays. *Nanotechnology*, **12**, 238–244 (2001).

[65] M. Burghard. A Freight Train of Nanotubes for Cargo Transport on the Nanoscale. *Angew. Chem. Int. Ed.*, **47**, 8565–8566 (2008).

[66] K. Svoboda, C. F. Schmidt, B. J. Schnapp, S. M. Block. Direct Observation of Kinesin Stepping by Optical Trapping Interferometry. *Nature*, **365**, 721 (1993).

[67] H. Yin, M. D. Wang, K. Svoboda, R. Landick, S. M. Block, J. Gelles. Transcription Against an Applied Force. *Science*, **270**, 1653 (1995).

[68] D. Stock, A. G. W. Leslie, J. W. Walker. Molecular Architecture of the Rotary Motor in ATP Synthase. *Science,* **286**, 1700 (1999).

[69] R. Seidel, C. Dekker. Single-Molecule Studies of Nucleic Acid Motors. *Curr. Opin. Struct. Biol.*, **17**, 1, 80–86 (2007).

[70] B. A. Grzybowski, K. J. M. Bishop, C. J. Campbell, M. Fialkowski, S. K. Smoukov. Micro- and Nanotechnology via Reaction–Diffusion. *Soft Matter*, **1**, 114–128 (2005).

[71] A. Einstein. Investigations on the Theory of Brownian Movement. *Dover,* New York (1956).

[72] A. Einstein. *Ann. Phys.*, Leipzig, **17**, 549 (1905).

[73] N. S. Zacharia, Z. S. Sadeq, G. A. Ozin. Enhanced Speed of Bimetallic Nanorod Motors by Surface Roughening. *Chem. Comm.*, 5856–5858 (2009).

[74] C. Stock, N. Heureux, W. R. Browne, B. L. Feringa. Autonomous Movement of Silica and Glass Micro-Objects based on a Catalytic Molecular Propulsion System. *Chem. Eur. J.*, **14**, 3146–3153 (2008).

[75] Definition of "catalyst" from wikipedia.com; definition of "Hydrogen Peroxide Decomposition" from: newworldencyclopedia.org/entry/Hydrogen_peroxide

[76] I. Arslan, J. C. Walmsley, E. Rytter, E. Bergene, P. A. Midgley. Towards Three Dimensional Nanoengineering of Heterogeneous Catalysts. *J. Am. Chem. Soc.*, **130**, 17, 5716–5719 (2008).

[77] L. F. Valadares, Y.-G. Tao, N. S. Zacharia, V. Kitaev, F. Galembeck, R. Kapral, G. A. Ozin. Catalytic Nanomotors: Self-Propelled Sphere Dimers. *Small*, **6**, 4, 565–572, (2010).

[78] A. Sen, M. Ibele, Y. Hong, D. Velegol. Chemo- and Phototactic Nano/Microbots. *Faraday Discuss.*, **143**, 15–27 (2009).

[79] R. S. Disselkamp**.** Can Aqueous Hydrogen Peroxide be used as a Stand-Alone Energy Source? *Intern. J. Hydrogen Energy*, **35**, 3, 1049–1053 (2010).

[80] R. F. Ismagilov, A. Schwartz, N. Bowden, G. Whitesides. Autonomous Motion and Self Assembly. *Angew. Chem. Int. Ed.*, **41**, 4 (2002).

[81] K. M. Manesh, M. Cardona, R. Yuan, M. Clark, D. Kagan, S. Balasubramanian, J. Wang. Template-assisted Fabrication of Salt-Independent Catalytic Tubular Microengines. *ACS Nano*, **4**, 4, 1799–1804 (2010).

[82] J. G. Gibbs, Y.-P. Zhao. Autonomous motile catalytic nanomotors by bubble propulsion. *Appl. Phys. Lett.***, 94**, 163104 (2009).

[83] C. Stock, N. Heureux, W. R. Browne, B. L. Feringa. Autonomous Movement of Silica and Glass Micro-Objects Based on a Catalytic Molecular Propulsion Sytem. *Chem. Eur. J.*, **14,** 3146–3153 (2008).

[84] P. Snabre, F. Magnifotcham. Formation and Rise of a Bubble Stream in a Viscous Liquid. *Eur. Phys. J. B*, **4**, 369–377 (1998).

[85] W. F. Paxton. S. Sundararajan, T. E. Mallouk, A. Sen. Chemical Locomotion. *Angew. Chem. Int. Ed.*, **45**, 5420–5429 (2006).

[86] W. F. Paxton, A. Sen, T. E. Mallouk. Motility of Catalytic Nanoparticles through Self-Generated Forces. *Chem. Eur. J.*, **11**, 6462–6470 (2005).

[87] Y. Wang, R. M. Hernandez, D. J. Bartlett, Jr., J. M. Bingham, T. R. Kline, A. Sen, T. E. Mallouk. Bipolar Electrochemical Mechanism for the Propulsion of Catalytic Nanomotors in Hydrogen Peroxide Solutions. *Langmuir*, **22**, 10451–10456 (2006).

[88] W. F. Paxton, P. T. Baker, T. R. Kline, Y. Wang, T. E. Mallouk, A. Sen. Catalytically Induced Electrokinetics for Motors and Micropumps. *J. Am. Chem. Soc.*, **128**, 14881–14888 (2006).

[89] M. Pumera. Electrochemically Powered Self-Propelled Electrophoretic Nanosubmarines. *Nanoscale*, **2**, 1643–1649 (2010).

[90] P. Dhar, Th. M. Fischer, Y. Wang, T. E. Mallouk, W. F. Paxton, A. Sen. Autonomously Moving Nanorods at a Viscous Interface. *Nano Lett.*, **6**, 1, 66–72 (2006).

[91] R. Laocharoensuk, J. Burdick, J. Wang. Carbon-Nanotube-Induced Acceleration of Catalytic Nanomotors. *ACS Nano*, **2**, 5, 1069–1075 (2008).

[92] U. K. Demirok, R. Laocharoensuk, K. M. Manesh, J. Wang. Ultrafast Catalytic Alloy Nanomotors. *Ang. Chem. Int. Ed.*, **47**, 48, 9349–9351 (2008).

[93] J. M. Catchmark, S. Subramanian, A. Sen. Directed Rotational Motion of Microscale Objects Using Interfacial Tension Gradients Continually Generated via Catalytic Reactions, *Small,* **1**, 2, 202–206 (2005).

[94] J. G. Gibbs, Y.-P. Zhao. Design and Characterization of Rotational Multicomponent Catalytic Nanomotors. *Small*, **5**, 20, 2304–2308 (2009).

[95] N. B. Saidulu, K. L. Sebastian. Interfacial Tension Model for Catalytically Driven Nanorods. *J. Chem. Phys.*, **128**, 074708 (2008).

[96] J. R. Howse, R. A. L. Jones, A. J. Ryan, T. Gough, R. Vafabakhsh, R. Golestanian. Self-Motile Colloidal Particles: From Directed Propulsion to Random Walk. *Phys. Rev. Lett.*, **99**, 048102 (2007).

[97] R. Golestanian, T. B. Liverpool, A. Ajdari. Propulsion of a Molecular Machine by Asymmetric Distribution of Reaction Products. *Phys. Rev. Let*., **94**, 220801 (2005).

[98] S. J. Ebbens, J. R. Howse. In Pursuit of Propulsion at the Nanoscale. *Soft Matter*, **6**, 726–738 (2010).

[99] M. Fialkowski, K. J. M. Bishop, F. Klajn, S. K. Smoukov, C. J. Campbell, and B. A. Grzybowski. Principles and Implementations of Dissipative (Dynamic) Self-Assembly. *J. Phys. Chem. B*, **110**, 2482–2496 (2006).

[100] R. Klajn, K. J. M. Bishop, B. A. Grzybowski. Light-controlled Self-Assembly of Reversible and Irreversible Nanoparticle Suprastructures. *Pros. Nat. Acad. Sci.*, **104**, 25, 10305–10309 (2007).

[101] S. Soh, K. J. M. Bishop, B. A. Grzybowski. Dynamic Self-Assembly in Ensembles of Camphor Boats. *J. Phys. Chem. B*., **112**, 10848–10853 (2008).

[102] H. Hess. Self-Assembly Driven by Molecular Motors. *Soft Matter*, **2**, 669–677 (2006).

[103] S. Mann. Self-Assembly and Transformation of Hybrid Nano-Objects and Nanostructures under Equilibrium and Non-Equilibrium Conditions. *Nat. Materials*, **8**, 781–792 (2009).

[104] B. A. Grzybowski, C. E. Wilmer, J. Kim, K. P. Browne, K. J. M. Bishop. Self-Assembly: From Crystals to Cells. *Soft Matter*, **5**, 1110–1128 (2009).

[105] D. L. Hu, B. Chan, J. W. M. Bush. The Hydrodynamics of Water Strider Locomotion. *Nature* **424**, 663–666 (2003).

[106] K. J. M. Bishop, C. E. Wilmer, S. Soh, B. A. Grzybowski. Nanoscale Forces and Their Uses in Self Assembly. *Small,* **14**, 1600–1630 (2009).

[107] J. Pelesko. Self Assembly: The Science of Things That Put Themselves Together. *Chapman & Hall, CRC Press* (2007).

[108] E.J. Smith, D. Makarov, S. Sanchez, V. M. Formin, O. G. Schmidt. Magnetic Microhelix Coil Structures. *Phys. Rev. Lett.*, **107**, 097204 (2011).

[109] S. Y. Teh, R. Lin, L-H. Hung, A. P. Lee. Droplet Microfluidics. *Lab Chip*, **8**, 198–220 (2008).

[110] Definition of "PDMS" material, source: *wikipedia.com*

[111] S. F. Jones, G. M. Evans, K. P. Galvin. Bubble Nucleation from Gas Cavities – a Review. *Adv. Colloid Interface Sci.*, **80**, 27–50 (1999).

[112] M. Kukizaki, Y. Baba. Effect of Surfactant Type on Microbubble Formation Behavior using Shirasu Porous Glass Membranes. *Colloids and Surfaces A: Physicochem. Eng. Aspects*, **326**, 129–137 (2008).

[113] Definition of "Benzalkonium Chloride", source: *wikipedia.com*

[114] L. Maggi, M. L. Torre, P. Giunchedi, U. Conte. Supramicellar Solutions of Sodium Dodecyl Sulphate as Dissolution Media to Study the *in vitro R*elease Characteristics of Sustained- release Formulations Containing an Insoluble Drug. *Int. J. Pharmaceuticals,* **35**, 1, 73–79 (1996).

[115] N. Mano, A. Heller. Bioelectrochemical Propulsion. *J. Am. Chem. Soc.*, **127**, 11574–11575 (2005).

[116] D. Pantarotto, W. R. Browne, B. L. Feringa. Autonomous Propulsion of Carbon Nanotubes Powered by a Multienzyme Ensemble. *Chem. Commun.*, 1533–1535 (2008).

[117] J. F. Dijksman. Hydro-Acoustics of Piezoelectrically Driven Ink-Jet Print Heads Flow, Turbulence and Combustion*, Kluwer Adademic Publishers*, **61**, 211 (1999).

[118] A. Nisar, N. Afzulpukar, B. Mahaisavariya, A. Tuantranont, "MEMS-based Micropumps in Drug Delivery and Biomedical Applications, *Sensors and Actuators*, B **130**, 971–942 (2008).

[119] S.-H. Chiu, C.-H. Liu. An Air Bubble Actuated Micropump for On-Chip Blood Transportation. *Lab Chip*, **9**, 1524–1533 (2009).

[120] S. T. Chang, E. Beaumont, D. N. Petsev, O. D. Velev. Remotely Powered Distributed Microfluidic Pumps and Mixers Based on Miniature Diodes. *Lab Chip*, **8**, 117–124 (2008).

[121] S. T. Chang, V. N. Paunov, D. N. Petsev, O. D. Velev. Remotely Powered Self-Propelling Particles and Micropumps based on Miniature Diodes. *Nat. Mater.*, **6**, 235–240 (2007).

[122] M. W. J. Prins, W. J. J. Welters, J. W. Weekamp, Fluid Control in Multichannel Structures by Electrocapillary Pressure. *Science*, **291**, 277–280 (2001).

[123] B. S. Gallardo, V. K. Gupta, F. D. Eagerton, L. I. Jong, V. S. Craig, R. R. Shah, N. L. Abbott. Electrochemical Principles for Active Control of Liquids on Submillimeter Scales. *Science*, **283**, 57. (1999).

[124] D. E. Kataoka, S. M. Troian. Patterning Liquid Flow on the Microscopic Scale. *Nature*, **402**, 794 (1999).

[125] T. R. Kline, J. Iwata, P. E. Lammert, T. E. Mallouk, A. Sen, D. Velegol. Catalytically Driven Colloidal Patterning and Transport. *J. Phys. Chem. B*, **110**, 24513–24521 (2006).

[126] S. Subramanian, J. M. Catchmark. Control of Catalytically Generated Electroosmotic Fluid Flow through Surface Zeta Potential Engineering. *J. Phys. Chem. C*, **111**, 11959–11964 (2007).

[127] M. E. Ibele, Y. Wang, T. R. Kline, T. E. Mallouk, A. Sen. Hydrazine Fuels for Bimetallic Catalytic Microfluidic Pumping. *J. Am. Chem. Soc*. **129**, 7762–7763 (2007).

[128] W. F. Paxton, P. T. Baker, T. R. Kline, Y. Wang, T. E. Mallouk, and A. Sen. Catalytically Induced Eletrokinetics for Motors and Micropumps. *J. Am. Chem. Soc.*, **128**, 14881–14888 (2008).

[129] D. J. Thurmer, C. Deneke, Y. F. Mei, O. G. Schmidt. Process Integration of Microtubes for Fluidic Applications. *Appl. Phys. Lett.*, **89**, 223507 (2006).

[130] O. G. Schmidt, K. Eberl. Thin Solid Films Roll into Nanotubes. *Nature*, **410**, 168 (2001).

[131] E. J. Smith, S. Schulze, S. Kiravittaya, Y. F. Mei, S. Sanchez, O. G. Schmidt. Lab-in-a-Tube: Detection of Individual Mouse Cells for Analysis in Flexible Split-Wall Microtube Resonator Sensors. *Nano Lett.* **11**, 10, 4037–4042 (2011).

[132] G. A. Bekey. Autonomous Robots: From Biological Inspiration to Implementation and Control (Ingelligent Robotics and Autonomous Agents series). *The MIT Press, Cambridge, Massachusetts* (2005).

[133] W.Stumm. Chemistry on the Solid-Water Interface*, John Wiley and Sons,* New York, NJ*, **4** (1993).

[134] V. B. Shenoy, D. T. Tambe, A. Prasad, J. A. Theriot. A Kinematic Description of the Trajectories of Listeria Monocytogenes Propelled by Actin Comet Tails. *Proc. Nat. Acad. Sci.*, **104**, 20, 8229–8234 (2007).

[135] L. Betancor, A. Hidalgo, G. Fernandez-Lorente, C. Mateo, R. Fernandez-Lafuente, J. M. Guisan. Preparation of an Stable Biocatalyst of Bovine Liver Catalase using Immobilization and Postimmobilization Techniques. *Biotechnol. Prog.*, **19**, 763– 767 (2003).

[136] R. K. Soong, G. D. Bachand, H. P. Neves, A. G. Olkhovets, H. G. Craighead, C. D. Montemagno. Powering an Inorganic Nanodevice with a Biomolecular Motor. *Science*, **290**, 5496, 1555–1558 (2000).

[137] D. B. Weibel, P. Garstecki, D. Ryan, W. R. DiLuzio, M. Mayer, J. E. Seto, G. M. Whitesides. Microoxen: Microorganisms to Move Microscale Loads. *Proc. Nat. Acad. Sci.*, **102**, 34, 11963–11967 (2005).

[138] D. Velegol, H. A. Jerri, J. J. McDermott, and N. Chaturvedi. Microfactories for Colloidal Assemblies. *Am. Institute Chem. Eng.*, **56**, 3, 564–569 (2010).

[139] P. Dhar, Y. Cao, T. Kline, P. Pal, C. Swayne, T. M. Fischer, B. Miller, T. E. Mallouk, A. Sen, T. H. Johansen. Autonomously Moving Local Nanoprobes in Heterogenerous Magnetic Fields. *J. Phys. Chem. C*, **111**, 3607–3613 (2007).

[140] J. Burdick, R. Laocharoensuk, P. M. Wheat, J. D: Posner, J. Wang. Synthetic Nanomotors in Microchannel Networks: Directional Microchip Motion and Controlled Manipulation of Cargo. *J. Am. Chem. Soc.*, **130**, 8164–8165 (2008).

[141] J. G. Gibbs, Y. P. Zhao. Measurement of Driving Force of Catalytic Nanomotors in Dilute Hydrogen Peroxide by Torsion Balance. *Rev. Sci. Instrum.,* **79,** 8, 086108 (2008).

[142] M. Ibele, T. E. Mallouk, A. Sen. Schooling Behavior of Light-powered Autonomous Micromotors in Water. *Angew. Chem. Int. Ed.*, **48**, 3308–3312 (2009).

[143] Y. Hong, M. Diaz, U. M. Córdova-Figueroa, A. Sen. Light-Driven Titanium-Dioxide-Based Reversible Microfireworks and Micromotor/Micropump Systems. *Adv. Function. Mater.*, **20**, 10, 1568–1576 (2010).

[144] T. R. Kline, A. Sen. Reversible Pattern Formation through Photolysis. *Langmuir*, **22**, 7124–7127 (2006).

[145] M. Kolb, P. Rach, J. Schäfer, A. Wild, Fresenius. Investigations of Oxidative UV Photolysis. *J. Anal. Chem.*, **342**, 341 (1992).

[146] O. Feuerstein, D. Moreinos, D. Steinberg, Synergic Antibacterial Effect Between Visible Light and Hydrogen Peroxide on Streptococcus Mutans. *J. Antimicrob. Chemother.*, **57**, 872 (2006).

[147] Z-G. Zhao, M. Miyauchi. Nanoporous-Walled Tungsten Oxide Nanotubes as Highly Active Visible-Light Driven Photocatalysts. *Ang. Chem., Int. Ed.*, **47** (37), 7051–7055 (2008).

[148] J. Kim, C. W. Lee, W. Choi. Platinized WO3 as an Environmental Photocatalyst that Generates OH Radicals under Visible Light. *Environ. Sci. Technol.*, **44**, 6849 (2010).

[149] O. Horvath, R. Huszank. Degradation of Surfactants by Hydroxyl Radicals Photogenerated from Hydroxoiron(III) Complexes. *Photochem. Photobiol. Sci.,* **2**, 960 (2003).

[150] A. Cuzzola, M. Bernini, P. Salvadori. A Preliminary Study on Iron Species as Heterogeneous Catalysts for the Degradation of Linear Alkylbenzene Sulphonic Acids by Hydrogen Peroxide. *Appl. Catal. B*, **36**, 231, 3–8 (2002).

[151] J. Kou, Z. Li, Y. Yuan, H. Zhang, Y. Wang, Z. Zou. Visible-Light-Induced Photocatalytic Oxidation of Polycyclic Aromatic Hydrocarbons over Tantalum Oxynitride Photocatalysts. *Environ. Sci. Technol.*, **43**, 2979 (2009).

[152] R. Abe, H. Takami, N. Murakami, B. Ohtani. Pristine Simple Oxides as Visible Light Driven Photocatalysts: Highly Efficient Decomposition of Organic Compounds over Platinum-Loaded Tungsten Oxide. *J. Am. Chem. Soc.*, **130**, 7780 (2008).

[153] S. B. Hall, E. A. Khudaish, A.L. Hart. Electrochemical Oxidation of Hydrogen Peroxide at Platinum Electrodes. Part 1. An Adsorption-Controlled Mechanism**.** *Electrochim. Acta*, **43,** 5, 579–588 (1998).

[154] C. H. Liao, M. D. Gurol. Chemical Oxidation by Photolytic Decomposition of Hydrogen Peroxide. *Environ. Sci. Technol.*, **29**, 3007–3014 (1995).

[155] S.V. Golod, V.Ya. Prinz, P. Waegli, L. Zhang, O. Kirfel, E. Deckardt, F. Glaus, C. David, D. Gruetzmacher. Freestanding SiGe/Si/Cr and SiGe/Si/Si$_x$N$_y$/Cr Microtubes. *Appl. Phys. Lett.,* **84**, 3391 (2004).

[156] P. Tyagi, N. Bassik, T. G. Leong, J. H. Cho, B. R. Benson, D. H. Gracias. Microassembly based on Hands Free Origami with Didirectional curvature. *J. Microelectromech. Syst*., **18**, 784, (2009).

[157] C. C. Bof Bufon, J. D. C. Gonzalez, D. J. Thurmer, D. Grimm, M. Bauer, O. G. Schmidt. Self-Assembled Ultra-Compact Energy Storage Elements Based on Hybrid Nanomembranes. *Nano Lett*., **10** (7), 2506–2510 (2010).

[158] S. Sanchez, A. A. Solovev, S. M. Harazim, Ch. Deneke, Y. F. Mei, O. G. Schmidt. The Smallest Man-Made Jet Engine. *Chem. Records*, **11** (6), 367–370 (2011).

[159] http://www.guinnessworldrecords.com/records-9000/smallest-jet-engine

[160] R. Fernandes, D. H. Gracias. Towards a Miniaturized Mechanical Surgeon. *Materials Today*, **12**, 14–20 (2009).

[161] T. G. Leong, C. L. Randall, B. R. Benson, N. Bassik, G. M. Stern, D. H. Gracias. Tetherless thermobiochemically Actuated Microgrippers. *Proc. Nat. Acad. Sci.*, **106**, 703–708 (2009).

[162] N. Bassik, A. Brafman, A. M. Zarafshar, M. Jamal, D. Luvsanjav, F. M. Selaru, D. H. Gracias. Enzymatically Triggered Actuation of Miniaturized Tools. *J. Am. Chem. Soc.*, **132**, 16314–16317 (2010).

[163] V. Ya. Prinz, V. A. Seleznev, A. K. Gutakovsky, A. V. Chehovskiy, V. V. Preobrazenskii, M. A. Putyato, T. A. Gavrilova. Free-Standing and Overgrown InGaAs/GaAs Nanotubes, Nanohelices and Their Arrays. *Physica E, **6***, 828–831 (2000).

[164] C. Deneke, C. Müller, N. Y. Jin-Phillipp, O. G. Schmidt. Diameter Scalability of Rolled up In(Ga)As/GaAs Nanotubes. *Semicond. Sci. Technol*., **17,** 1278–1281 (2002).

[165] M. Grundmann. Nanoscroll Formation from Strained Layer Heterostructures. *Appl Phys. Lett*., **83**, 2444–2446 (2003).

[166] G. P. Nikishkov. Curvature Estimation for Multilayer Hinged Structures with Initial Strains. *J. Appl. Phys.*, **94** (8), 5333–5336 (2003).

[167] A. S. Mikhailov, G. Ertl. Non-equilibrium Microstructures in Reactive Monolayers as Soft Matter Systems. *Chem. Phys. Chem*., **10** (1), 86-100 (2009).

[168] X. Gao, L. Jiang. Water-Repellent Legs of Water Striders. *Nature*, **432**, 36 (2004).

[169] S. Floyd, M. Sitti. Design and Development of the Lifting and Propulsion Mechanism for a Biologically Inspired Water Runner Robot. *IEEE Tran. Robot.*, **24**, 698 (2008).

[170] L. Jiang, X. Yao, H. Li, Y. Fu, L. Chen, Q. Meng, W. Hu, L. Jiang. Water Strider: Legs with a Self-Assembled Coating of Single-Crystalline Nanowires of an Organic Semiconductor. *Adv. Mater*. **22**, 376 (2010).

[171] D. L. Hu, M. Prakash, B. Chan, J. W. M. Bush, *Exp. Fluids*, **43**, 769. Water-Walking Devices (2007).

[172] G. Palazzo, D. Fiorentino, G. Colafemmina, A. Ceglie, E. Carretti, L. Dei, P. Baglioni. Nanostructured Fluids based on Propylene Carbonate/Water Mixtures. *Langmuir*, **21**, 6717 (2005).

[173] J. W. M. Bush, D. L. Hu, M. Prakash. The Integument of Water-Walking Anthropods: Form and Function. *Adv. Insect Physiol.*, **34**, 118 (2008).

[174] The Surface Tension Value for Propylene Carbonat at 20 °C is 41.93 dyn/cm, from the source: *macro.lsu.edu/HowTo/solvents/Propylene%20Carbonate.htm*, Water (at 20 °C) 72.8 dyne/cm, from the source *hyperphysics.phy-astr.gsu.edu/Hbase/surten.html.*

[175] B.A. Grzybowski, H. A. Stone, G. M. Whitesides. Dynamic Self-Assembly of Magnetized Millimetre-sized Objects Rotating at a Liquid–Air Interface *Nature*, **405**, 1033–1036 (2000).

[176] Y. Wang, S. Fei, Y.M. Byun, P. E. Lammert, V. H. Crespi, A. Sen, T. E. Mallouk Dynamic Interactions between Fast Microscale Rotors. *J. Am. Chem. Soc.*, **131,** 29, 9926–9927 (2009).

[177] Image of Meniscus-Climbing Insect from the Source: *http://www.me.gatech.edu*

[178] N. Bassik, A. Brafman, A. M. Zarafshar, M. Jamal, D. Luvsanjav, F. M. Selaru, D. H. Gracias. Enzymatically Triggered Actuation of Miniaturized Tools. *J. Am. Chem. Soc.*, **132** (46), 16314–16317 (2010).

[179] R. Fernandes, D. H. Gracias. Toward a Miniaturized Mechanical Surgeon. *Materials Today*, **12** (10), 14–20 (2009).

[180] T. G. Leong, C. L. Randall, B. R. Benson, N. Bassik, G. M. Stern, D. H. Gracias. Tetherless Thermobiochemically Actuated Microgrippers. *Proc. Nat. Acad. Sci.*, **106** (3) 703-708 (2009).

[181] B. J. Nelson, I. K. Kaliakatsos, J. J. Abbott. Microrobots for Minimally Invasive Medicine. *Annu. Rev. Biomed. Eng.*, **12**, 55–85 (2010).

Appendix

Photolithography and electron-beam deposition:

- Microtubes, such as Ti/Cr/Pt, Ti/Au, Ti/ Fe/Cr/Pt, Ti/Fe/Au /Ag were fabricated by e-beam deposition of thin metallic films on lithographically patterned photoresist layers. Square or circular photoresist patterns with sizes 10–1000 μm were prepared on 1.5-inch silicon wafers or glass substrates;
- Samples were cleaned in acetone bath (ultrasound) for 1 min followed by the rinsing in isopropanol and drying in nitrogen;
- Photoresist AR-P 3510 was spin-coated on samples at 3500 rpm for 35 s, followed by 1 minute of baking using hotplate at 90° C;
- Samples were exposed during 5 seconds to UV light using Karl Suss MA56 Mask Aligner (410-605 nm), followed by the development of structures in a 1:1 AR300-35:H_2O during 45-60 s and rinsing in pure water for 1 minute;
- Angular deposition of materials by e-beam. Layers with a total thickness from 5 to 15 nm were used (detected by quartz crystal microbalance). Layers were deposited at angles from 60 to 75 degrees from horizontal line. Note: for different machines tooling factors of materials depositions must be optimized for the e-beam, the described parameters give diameters of microtubes from 5 to 10 micrometers. When magnetron sputtering is used, the thickness of Pt should not exceed 1 nm to avoid the coverage of photoresist shadow windows;
- By underetching of sacrificial photoresist layer in acetone (thin films roll-up into microtubes). In some cases if tubed did not roll in aceton another solvent N-Methyl Pyrrolidone (NMP) was used. The rolled-up process in this case can take several days;
- To avoid microtubes collapsing in the air they were kept in a liquid or supercritical point drying method was used.

Catalytic microengines for different applicaitons:

Tubular micropumps

Fabrication of rolled-up micropumps: Rolled-up microtubes consisting of Ti/Cr/Pt thin films (10/10/1 nm) were prepared according to photolithography procedure, described above. Ti/Cr layers of 10/10 nm were prepared in *Edwards* thin film systems machine at evaporation rates of 2.0 and 1.5 Å s^{-1} respectively. Initial chamber pressure of 5·10^{-7} mbar was used. Pt was sputtered by using *MTD 450 DCA* instruments machine with a total thickness of 1 nm at 4.4 nm min^{-1}. Samples deposited by e-beam were tilted to an angle of 75 degrees from horizontal line. A flat sputtering (0 degrees) was done for the Pt deposition. In order to activate the micropumps, the fabricated arrays of microtubes were immersed into hydrogen peroxide solution containing Benzalkonium Chloride (BC) at 0.5 v/v %. The surfactant concentration was kept constant during all experiments. The concentration of the hydrogen peroxide was varied from 0.009 to 11 v/v %. Polystyrene microspheres (Duke Scientific Corp., 1 % Solids) with diameters of 1 μm and 7 μm were used in the experiment for particle pumping.

Autonomous motion

For demonstrations of autonomous motion Ti/Cr/Pt (5/5/1 nm) microtubes were used. Pt was prepared by magnetron sputtering, 1 or 2 nm. For autonomous motion of nanotubes, heteroepitaxial layers have been used, described below.

Magnetic control of motion

Ferromagnetic material was incorporated in tubular layers which allowed magnetic remote control of self-propelled microjets. Different materials combinations have been successfully used, including: Ti/Fe/Ag/Pt, Ti/Fe(Co)/Au/Pt, Ti/Fe/Co/Pt, Ti/Fe/Cr/Pt. However, the remote control study was concentrated on Ti/Fe/Cr/Pt microtubes. *Fuels:* aqueous solution of hydrogen peroxide in mixture with different concentration of surfactant or a common soap were used.

Meniscus-climbing effect and self-organization

Microtubes consisted of Ti/Cr/Pt (5/5/1 nm) layers were used. Application of propylene carbonate (PC) gives a stronger meniscus capillary force than in other cases. There was no any surfactant in the fuel. In some cases, to create a local gradient of the fuel and the surface tension, a droplet of hydrogen peroxide was added into the bulk PC to activate microtubes and bring them to the air-liquid interface. *Fuel*: propylene carbonate in mixtures with water and hydrogen peroxide.

Preparation of synthetic micro-cargo

Polysterene microparticles (Duke Scientific Corp., 1 % solids) with the diameter 7 μm has been used for transportation and delivery of cargo. Other objects included square thin films, i.e. "nanoplates" with a width of 50 μm. Nanoplates consisted of thin hydrophobic metallic films, usually made of Ti/Fe/Pt (10/5/1) prepared by the e-beam without tilted angle. Magnetic (Fe) layer was used for an easy alignment of nanoplates towards remote controlled moving microjets. Nanoplates were under-etched in acetone followed by rinsing in isopropanol and released in the hydrogen peroxide fuel. Around 50 % of nanoplates were floating on the solution surface due to hydrophobic effect. Because of planar surface of Pt no bubbles were observed and thus the cargo was well suitable for transportation. Nanoplates float stochastically on top of solution of hydrogen peroxide or, due to contained magnetic layer, they could align the rotation degree according to the direction of external magnetic field.

Preparation of biological micro-cargo

The murine CAD cells were grown in DMEM/F-12 medium (Dulbecco's Modified Eagle Medium) supplemented with 10 % FCS (Fetal Calf serum) and 1% penicil lin/streptomycin (cells and procedure were provided by S. Schulze). The cells were incubated in a humidified atmosphere with 5% CO_2 and were passaged every 3–4 days by trypsination and centrifugation at 4400 rpm for 5 min. After determination of cell numbers with a hemocytometer, CAD cells were plated at 10^5 cells per plate. A small amount of CAD cells (10 μl of $\sim 10^5$ cells per ml) was suspended in 1.2 ml of the working solution containing the microjets and the chemical fuel to actuate them.

Supercritical point dryer

Rolled-up tubes have thin walls and are easy collapse when solutions dry. To avoid this supercritical point drying method was used. In preparation process, acetone was used at first to remove the photoresist layer. Wet sample then has been transported to SPD machine. Fluids suitable for supercritical drying included carbon dioxide (critical point 304.25 K at 7.39 M Pa or 31.1 degrees Celsius at 1072 psi). The acetone is then washed away with high pressure liquid carbon dioxide. The liquid carbon dioxide is then heated until its pressure goes beyond the critical point, at this point the pressure can be gradually released and leave a dried microtubes.

Software for the analysis

Video Software (*Virtual Dub, Image J*) was used for analysis of videos. *Virtual Dub* software has been used to cut, change rate and edit videos. With *ImageJ* a detailed investigation of bubbles frequencies and speed of microtubes was done. Additionally, the quality/colour contrast of videos was improved in *Image J*.

Microjets control via *Labview* interface

Labview interface allows a simple control over the motions of microjets via serial and NI-Visa runtime engine and *Labview* runtime engines. A program was written to control the different position of a magnet with a joystick. Figure A1 shows a screenshot of the front panel where all parameters including speed and rotation angle of the motor can be read and controlled. Stepping motor *PD2-110-42* was used and it was connected to computer via serial port. Such motor allowed setting of rotational angle precisely (1.8° accuracy). Motor needs ~25 V to operate that is why an additional power supply has been used for it (note: driver for USB serial port should be additionally installed).
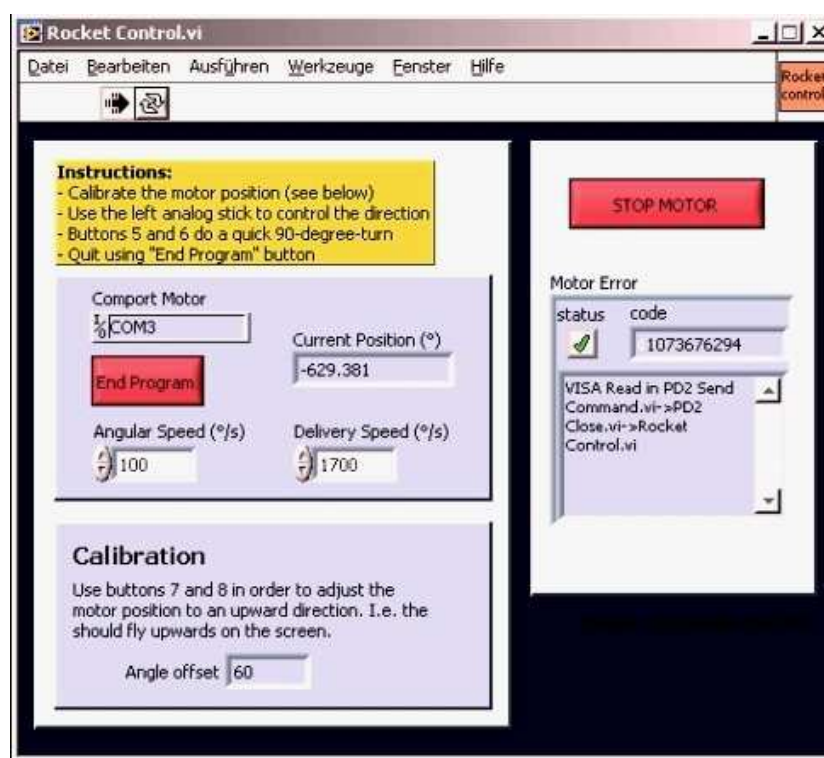
Figure A1: Snapshot of *Labview* interface for the control of microjets using magnetic field. Speed of stepping motor is set in the program for the rotational control of motor with a permanent magnet. Delivery speed shown here indicates a programmable button to rotate microjets at a higher speed of 1700 rps to deliver cargo [this code was written by J. R. Schröter].

Fabrication of PDMS microfluidics

PDMS was mixed with cross-linking agent and poured over glass master on a casting mold to get a negative bias-relief [provided by S. Harazim]. SU–8 photoresist master was fabricated by photolithography on a glass substrate. It followed by the baking on a hotplate for 30 min at 140° C degrees to harden PDMS. Then PDMS was cooled down to room temperature and peeled off a glass master. To activate surface PDMS and bare glass substrate were

inserted into oxygen RF plasma for 30 seconds. After plasma an immediate bonding of PDMS side with imprints on the glass was performed. To stabilize bond samples were left under contact with a mechanical load for 10 minutes. After that, the glass was sealed to the PDMS containing microfluidic channels.

PDMS procedure (Sylgard 184 Silicone Elastomer):
- Mix 10g of Sylgard 184 Silicone Elastomer (Base) and 1g (10% weight) of Sylgard 184 Silicone Elastomer (Curing Agent) in a beaker;
- Degas for 15 minutes in a desiccator (to remove the gas from the PDMS);
- Pour the PDMS in a casting mold with the structure on the bottom;
- Bake it for 30 minutes at 120°C (time depends on the thickness of PDMS). After baking and cooling down one can peel off the PDMS from substrate.

Fabrication of the SU-8 master stamp

The resist SU8-10 gets spin coated on a glass or silicon substrate for 30 s at 1500 rpm then baked first at 90° C for 10 min on the hot plate, plus 10 min cooling down in the air. The resist gets exposed in the MA56 mask-aligner for 20 s after the microchannel mask has been aligned. A second baking step at 90° C for 5 min in the oven with 10 min cooling down takes place to cross-link the exposed structures. Then the resist is developed in mr-DEV 600 for 90 s. The development reaction is stopped in isopropanol.

Biocatalytic catalase-based miroengines

Ti/Au rolled up microtubes were incubated into a 20 mM solution of 3-MPA for 45 min [Protocols are pvovided by Dr. S. Sanchez]. After washing with isopropanol for 5 min, the tubes were immersed in a 1 ml solution which contained the coupling agents EDC (0.05 M) and Sulfo-NHS (0.015 M) and catalase (2 mg ml^{-1}). This incubation was carried out overnight at 37°C and thereafter rinsed with PBS pH 5.5 and SDS 0.05 wt % for 15 min at each step. In a comparative experiment, the Ti/Au microtubes were incubated overnight at 37° C with a catalase solution (2 mg ml^{-1}) to physically adsorb the enzyme into the microtube.

Modification with thiol groups: An inner Au layer from the Ti/Au microtubes was functionalized with a Self Assembled Monolayer (SAM) of 3-mercaptopropionic acid (3-MPA). A solution of 20 mM of 3-MPA was prepared in Isopropanol, where the rolled-up tubes were immersed for 45 min [Protocol of Dr. S. Sanchez]. After rinsing the tubes with isopropanol for 5 min, they were placed in the eppendorf beaker (total volume 1 mL) containing: i) the coupling agents 1-Ethyl-3-[3-dimethylaminopropyl] carbodiimide hydrochloride (EDC) and N-hydroxylsulfosu-ccinimide (Sulfo-NHS) at 0.05 M and 0.015 M respectively, and ii) the enzyme catalase (2 mg mL-1). This incubation was carried out overnight at 37° C and thereafter rinsed with PBS pH 5.5 and SDS 0.05 wt % for 15 min at each step. *Physical adsorption of catalase in the Ti/Au microtubes:* A similar piece of *Si* substrate containing the Ti/Au microtubes was taken and incubated at 37° C with 1 mL of catalase solution (2 mg mL^{-1}) overnight and rinsed with PBS pH 5.5 and SDS 0.05 wt % for 15 min at each step. *Reagents:* all chemicals were provided by *Sigma Aldrich* (Germany). Contact angle measurements were carried out using a *CAM 101 goniometer* from *KSV Instruments Ltd (Helsinki, Finland).*

Heteroepitaxial semiconductor/catalyst nanotubes

The fabricated rolled-up nanotubes consisted of MBE grown [samples were provided by Dr. C. Deneke] heteroepitaxial bilayers InGaAs/GaAs/(Cr)/Pt where metals (Cr)/Pt were sputtered on top of semiconductor surface. The semiconductor bilayers were grown by MBE on a smoothed GaAs substrate following the protocol well described in Ref. [164]. On top of a

GaAs (001) substrate a 200 nm GaAs buffer was grown to smooth the surface, followed by the growth of 20 nm AlAs sacrificial layer. The last MBE deposition step included $In_{0.33}$ $Ga_{0.67}As$/GaAs bilayer with the thickness 3/3 nm. After MBE growth the samples were stored in a desicator with coated photoresist to pretect the oxidation of surface.

Magnetron sputtering of Cr/Pt and e-beam deposition of Fe layers: After MBE growth In-GaAs and InGaAs/GaAs wafers were cut and prepared for Cr and Pt sputtering. Magnetron sputtering was realized by MTD 450 DCA instruments machine. A total Cr/Pt layers consisted of 0.5–2 nm at typical sputtering rate 4 nm min^{-1} for Cr and 4.4 nm min^{-1} for Pt. For the remote magnetic control Fe/InGaAs/GaAs/Cr/Pt (2/3/3/1/1 nm) nanotubes were prepared. Tubes at first were rolled up without ferromagnetic layer, Fe was deposited on top of rolled up tubes by the e-beam. Subsequently, only half of tubes contained deposited Fe layer, it allowed keeping constant diameter of nanoscale tubes. Fe was sputtered at 1 A·s^{-1} at initial pressure 10^{-7} m bar.

Preparation of nanotubes for applications as nanotools

After deposition of metals the samples were immersed in HF solution for 30 seconds that under-etches selectively sacrificial AlAs layer and consequently the rolling-up of thin metallic films into nanotubes takes place. The used solution was composed of: 5 ml of a 10 % v/v HF solution with 1 ml of BC surfactant (2 ml 50 % HF diluted in 50 ml water). Final HF concentration was 8.3 % v/v. After mechanically creating trenches along the (In)GaAs <100> crystal direction hydrofluoric acid (HF) was used to under-etch the AlAs sacrificial layer and induce the nanomembrane to roll-up. This is due to the fact that the etching rate is faster in this direction and on the other hand it can be attributed to a minimum of the elastic module of the (In)GaAs. For the self-propelled nanotools experiment the mechanical stability of the InGaAs/GaAs/Pt nanotubes were enhanced by including a 1 nm thick Cr layer sandwitched between the InGaAs and Pt layers. The material composition of InGaAs/GaAs/Cr/Pt (3/3/1/1 nm) led to tubes with an average diameter of 600 nm.
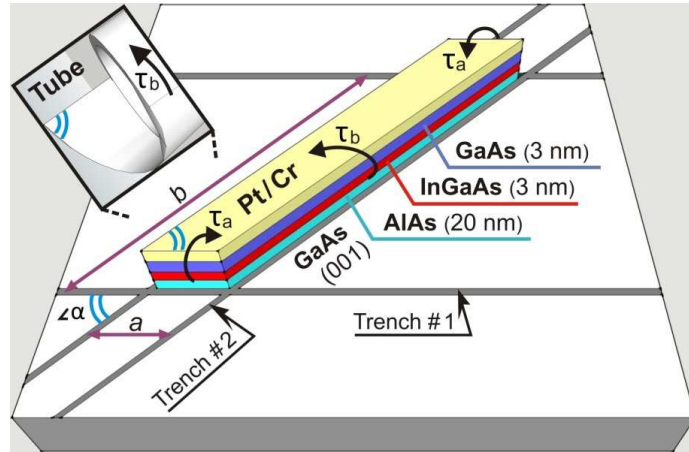

Figure A2. Schematic of individual parallelogram-like element consisting of hybrid catalytic/hetero-epitaxial $In_{0.33}Ga_{0.67}As$/GaAs/Cr/Pt thin film. Inset image shows one side tubular opening where a sharp tip is formed due to asymmetric rolling of layers.

Figure A2 shows schematic of a single parallelogram element consisting of hybrid catalytic/heteroepitaxial $In_{0.33}Ga_{0.67}As$/GaAs/Cr/Pt thin films. The fabricated elements have a parallelogram-like structure and are formed by the mechanical scratching of sample surface (using sand paper) at a certain shifted angle $\angle\alpha$. For the fabrication of tubular

nanotools scratching of the sample surface was done two times, indicated by trenches #1 and #2 in Fig. A2. Scratching opens access for the under-etching of sacrificial AlAs layer in 8.3 % v/v HF solution. The rolling process of heteroepitaxial films is highly influenced by the anisotropy of Young's modulus. Due to crystallographic orientation the layers have a tendency to roll along the InGaAs <001> direction, which is the direction parallel to trench #2, i.e. 45° angle between the trench #2 and edges of the sample. Since shallow etching technique was not used, solution under-etches sacrificial AlAs layer from all sides, and a competition between torques τ_a and τ_b is formed. Due to a difference in length of the discussed element, i.e. $b > a$, the torque τ_b is higher than τ_a. This difference defines the preferred direction of tube rolling, shown as inset of Fig. A2. In such case the asymmetry of rolling, which is defined by the layer rolling in InGaAs <001> direction, determines the formation of a tubular "sharp tip" with the angle defined by $\angle \alpha$. Subsequently, by fixing the trench #2 to 45° (angle between trench #2 and sample edges) and by changing the angle $\angle \alpha$ of trench #1 a controllable fabrication of tubular layers is achieved. As a result for the formation of sharper tips a smaller angle $\angle \alpha$ between trenches #1 and #2 must be used.

Nanotubes release from a substrate

After tubes rolling up nanojets samples were immersed into working solution containing hydrogen peroxide, cells and common soap (*Fit Gmbh*) followed by mechanical scratching of tubes from substrate using plastic tweezers. Common soap contained 5–15% anionic tenside (5–15%), amphoteric tenside (<5%), bronopol*, benzisothiazolinone, methylisothiazolinone. Soap concentration was optimized to 10 % v/v for the purpose to stabilize microbubbles.

HeLa cells culture

Before culturing *HeLa* cells on glass cover slips, the glass cover slips were sterilized by exposure to oxygen plasma for approximately 30 min (procedure provided by Dr. W. Xi and Prof. D. H. Gracias). To ensure the attachment of cells, the slips were modified by phosphonic acids according to the protocol previously reported. Briefly, the glass cover slips were immersed in 50 µM 11-phosphonoundecanoic acid in toluene for 12 hrs, then rinsed with toluene and dried at 90° C. The fibronectin was covalently attached to phosphonic acid functionalized glass cover slips by activation of the –COOH group using EDC and NHS. Phosphonic acid modified slips were dispersed in 1 ml of PBS containing 0.02 M EDC and 0.01 M NHS for 2 hours to activate the –COOH group. 20 µl fibronectin solution (1mg/ml) was then added to the –COOH-activated cover slip solution and left over night at 37° C. The activated –COOH group bound with the –NH$_3$ group of fibronectin, resulting the formation of covalent CO-NH amide bond. HeLa cells were dissociated by treating with trypsin (0.25 %, 5min, 37° C), then diluted in DMEM/10 % FBS supplemented with 0.5 mM L-glutamine and 1 % Penicillim/Streptomycin, and plated onto the cover slips at low density (10^4 cells/cm^2). The samples were flooded with freshly made medium and incubated for 24 hours to allow the cell spreading. After that the cell culture was briefly fixed in 2 % paraformaldehyde for 20 minutes and immersed into nanotube working solution (20 % peroxide and 10 % common soap) for the drilling experiment. In the transporting experiment, budding yeast cells (bakery yeast) are used. Budding yeast cells were culture in YPD medium (Casein, enzymatically digested 20 g l^{-1}, Yeast extract 10 g l^{-1}, Glucose 20 g l^{-1}, pH-value 6.5 ± 0.2, Carl Roth GmbH + Co. KG) overnight at 28° C. Yeast cells were then transferred into working solution for the delivery experiment. The concentration of the cells was controlled so that the substrate has a coverage of around 10^5 yeast cells/cm^2.

Preparation of *HeLa* cells (with embedded nanotubes) for SEM imaging

Prior to SEM imaging, cell culture is fixed in mixed primary fixative (3 % paraformaldehyde/0.1 M sodium cacodylate/0.05M $CaCl_2$/0.05M $MgCl_2$/2.5 % Sucrose and 1.5% glutaraldehyde at pH 7.4) at room temperature for 1 hour, then rinsed three times with 0.1 M sodium Cacodylate/2.5 % Sucrose solution. The cell culture is subsequently treated with post-fixative of 1% osmium tetraoxide in 0.1 M Cacodylate buffer at pH 7.4 on ice for 1 hour, and then rinsed thoroughly with water, and dehydrated with grade series of cold ethanol (70, 90, 100 %). The sample was then dried in critical point dryer and coated with 60 nm carbon for SEM imaging.

Publication List

14) W. Xi, <u>A. A. Solovev</u>, D. H. Gracias, A. N. Ananth, S. Sanchez, O. G. Schmidt. *Magnetic Microdrillers*, in preparation (2011).

13) <u>A. A. Solovev</u>, W. Xi, D. H. Gracias, S. Harazim, C. Deneke, S. Sanchez, O.G. Schmidt. *Self-Propelled Nanotools*, **ACS Nano**, DOI: 10.1021/nn204762w (2011).

12) <u>A. A. Solovev</u>, E. Smith, Carlos C. Bof ' Bufon, S. Sanchez, O. G. Schmidt. *Light-Controlled Propulsion of Catalytic Microengines,* **Angewandte Chemie International Edition,** 50 (46), 10875–10878 (2011).

11) S. Sanchez, <u>A. A. Solovev</u>, S. Harazim, Ch. Deneke, Y. F. Mei, O. G. Schmidt. *The Smallest Man-Made Jet Engine*, **Chemical Records**, 11 (6), 367 (2011).

10) <u>A. A. Solovev</u>, S. Sanchez, Y. F. Mei, O.G. Schmidt. *Tunable Catalytic Tubular Micro-pumps operating at Low Concentration of Hydrogen Peroxide,* **Physical Chemistry Chemical Physics**, 13, 10131 (2011).

9) U. Vogl, A. Saß, F. Vewinger, M. Weitz, <u>A. A. Solovev</u>, Y. F. Mei, O. G. Schmidt. *Light Confinement by a Cylindrical Metallic Waveguide in a Dense Buffer Gas Environment*. **Physics Review A,** 83, 053403 (2011).

8) Y. F. Mei, <u>A. A. Solovev</u>, S. Sanchez, O.G. Schmidt. *Rolled-up Nanotech on Polymers: From Basic Perception to Self-Propelled Catalytic Microengines,* **Chemical Society Reviews**, 40, 2109 (2011). **Cover Image** by Chemical Society Reviews. **Featured in:** derStandard.at, LiLipuz.de, Blick.ch

7) S. Sanchez, <u>A. A. Solovev</u>, S. Harazim and O.G. Schmidt. *Microbots swimming in the Flowing Streams of Microfluidic Channels,* **Journal of the American Chemical Society**, 133 (4), 701 (2011).

6) S. Sanchez, <u>A. A. Solovev</u>, S. Schulze and O. G. Schmidt. *Controlled Manipulation of Multiple Cells using Catalytic Microbots,* **Chemical Communications**, 47, 698 (2011). **Featured in:** RSC Chemistry World

5) S. Sanchez, <u>A. A. Solovev</u>, Y.F. Mei and O.G. Schmidt. *Dynamics of Biocatalytic Micro-Engines mediated by Variable Friction Control,* **Journal of the American Chemical Society**, 132, 13144 (2010). **Featured in:** Nanowerk Spotlight, ChemViews Magazine, RSC Chemistry World

4) <u>A. A. Solovev</u>, Y.F. Mei and O.G. Schmidt. *Catalytic Micro-Strider at the Air- Liquid Interface*, **Advanced Materials**, 22, 4340 (2010). **Featured in:** Materialsviews; Nanowerk Spotlight

3) <u>A. A. Solovev</u>, S. Sanchez, M. Pumera, Y.F. Mei and O. G. Schmidt. *Magnetic Control of Catalytic Microbots for the Delivery and Assembly of Microobjects*, **Advanced Functional Materials**, 20, 15, 2430 (2010). **Cover Image** by Advanced Functional Materials. **Featured in:** RSC Chemistry World, Nanowerk Spotlight

2) <u>A. A. Solovev</u>, Y.F. Mei, E. B. Ureña, G. Huang, and O. G. Schmidt. Catalytic *Microtubular Jet Engines Self-propelled by Accumulated Gas Bubbles,* **Small**, 5, 1688 (2009). **Cover Image** by Small

1) Y. F. Mei, G. S. Huang, <u>A. A. Solovev</u>, E. B. Ureña, I. Mönch, F. Ding, T. Reindl, R. K. Y. Fu, P. K. Chu, and O. G. Schmidt. *Versatile Approach for Integrative and Functionalized Tubes by Strain Engineering of Nanomembranes on Polymers*. **Advanced Materials,** 20, 4085–

4090, (2008). **Cover Image** by Advanced Materials. **Featured in:** Frankfurter Allgemeiner Zeitung, IFW Highlight, Pro-physik.de, PM Magazine, Zeit Wissen Magazine, Bild Zeitung, Magazines: Welt der Physik, Spektrum der Wissenschaft, TV: http://tv.orf.at

Total Number of Citations: **> 230**   (h-Index = **7**)

Publications № with Impact Factor above seven: **10**

Non-Peer Reviewed Publications

5) S. Sanchez, <u>A.A. Solovev</u>, E. J. Smith, C. C. Bof' Bufon, V. M. Fomin, A. N. Ananth, M. Viehrig, O. G. Schmidt. External Sources for controlling the propulsion of self-propelled micro-jet engines. **Annual Report**. IFW Dresden (2011)

4) S. Sanchez, <u>A. A. Solovev</u>, S. Schulze, S. M. Harazim, Y. F. Mei and O. G. Schmidt. *Catalytic and Biocatalytic Microbots*. **Annual Highlight**. IFW Dresden, 39–41 (2010)

3) <u>A. A. Solovev</u>, Y. F. Mei, and O.G. Schmidt. Nanorocket Epxeriments for High School. Dechema: Chemical & Biological Society, **Brochure**, Marburg (2010)

2) <u>A. A. Solovev</u>, S. Sanchez, Y. F. Mei and O. G. Schmidt. Wireless Control of Tubular Catalytic Microbots for the Transportation and Delivery of Microobjects. **Annual Report**. IFW Dresden (2009)

1) <u>A. A. Solovev</u>, Y. F. Mei, S. Harazim, C. Deneke, G. S. Huang, O. G. Schmidt. Self Propelled Microjets at Low Reynolds Number. **Annual Highlight**, 44–46, IFW Dresden (2008)

Selected Research Highlights:

Angew. Chem. Int. Ed., 50, 7220 (2011)
Chemie.de (September 9, 2011)
derStandard.at (March 8, 2011)
LiLipuz (March 9, 2011)
Blick.ch (March 9, 2011)
Pro-Physik.de (March 8, 2011)
Die Welt (March 8, 2011)
Scinexx (March 9, 2011)
Nanowerk (March 9, 2011)
Guinnessworldrecords.com (01.2011)
Chemistry World (Nov 19, 2010)
Nanowerk (Sep 30, 2010)
MaterialsViews (Nov 10, 2010)
RSC Chemistry World (July 29, 2010)
Nanowerk.com (Aug 3, 2010)
ChemViews Magazine (Aug 11, 2010)
Nanowerk.com (Aug 3, 2010)
Spektrum der Wissenschaft (Juli 2009)
Welt der Physik (Mai 16, 2009)
P.M. Magazine (February 17, 2009)
Frankfurter Allgemeine Zeitung (November 11, 2008)
Nanowerk (October 20, 2008)
Pro Physik (October 20, 2008)
Bild Zeitung (August 27, 2008)

Covers Art
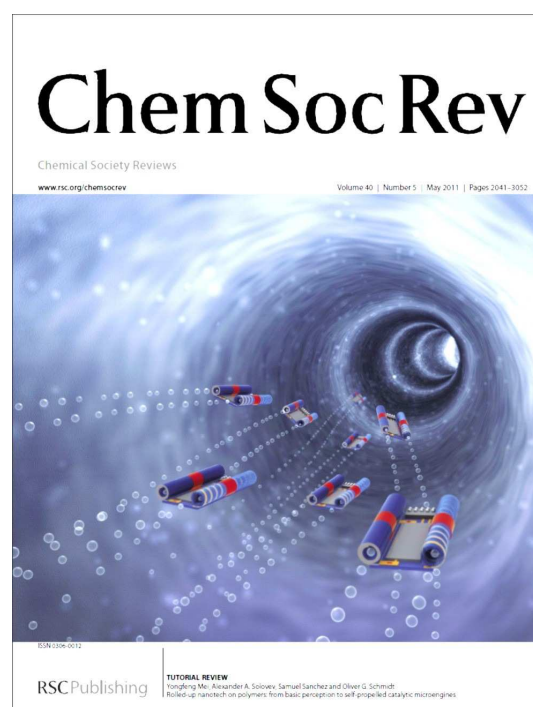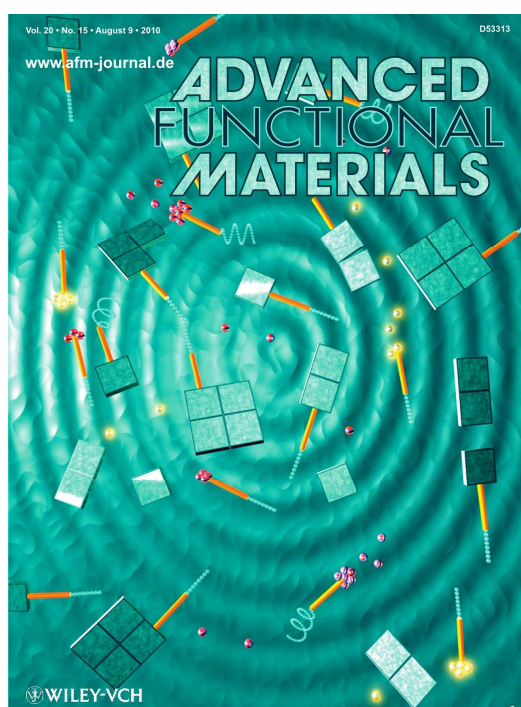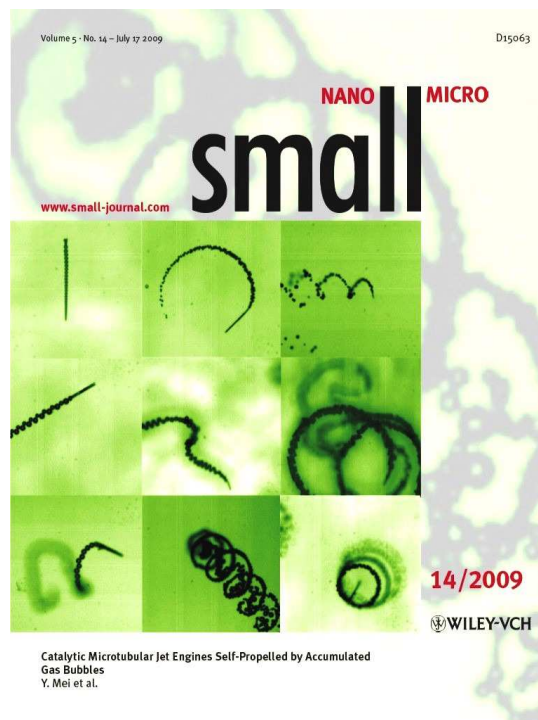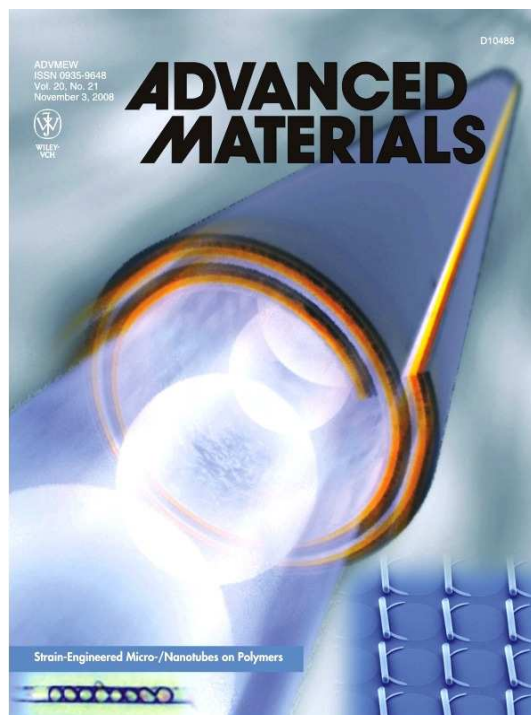
Acknowledgments

I want to thank very much my advisor **Professor Dr. Oliver G. Schmidt,** I want to express my heartfelt appreciation and gratitude for continues supervision, support, teaching and encouragement throughout my doctorate. It provided me with exceptional new skills and prepared me very well for the career of independent scientist. It helped me to organize my research and personal skills and learn how to become creative researcher and solve multiple scientific problems.

Dr. Samuel Sanchez and **Professor Dr. Yongfeng Mei**, my deepest gratitude for advices, directions and teaching me how to become a scientist. Many of our discussions shed light on problems or led to new ideas and developments in the lab. I enjoyed working with you, our discussions about science and life, sometimes outside of institute, helped me to develop creativity and deep insight into numerous problems, and particularly to organize my skills to write scientific publications. Thank you for useful discussions and helping me with preparation of this thesis.

Professor Dr. Heinrich Lang, thank you very much for finding time to read and evaluate this dissertation.

Professor Dr. David Gracias (Johns-Hopkins University), I appreciate very much your support and guidance, thank you for teaching me how to have a broad view and aim towards solution of 'high impact' reserach problems. During our collaboration we were able to finish important publication about "self-propelled nanotools".

Professor Dr. Vladimir Fomin, thank you for your interest in my research project and useful discussions which shed light on theoretical aspects of dynamic microjet engines.

Vladimir Bolanos, thank you for being my good friend, our discussion about scientific methodologies and life itself, sometimes outside of institute helped me to succeed and come back to lab work with a 'fresh and clear' mind.

Dr. Wang Xi, thank you for being a great collaborator, our discussions and experiments together led to realization of new ideas and publication.

Stefan Harazim, thank you for your technical support in fabrication of microfluidics and nanotubes, chemistry lab, during long night of science and continues help in translation of German.

Adithya Nagarakodige Ananth, thank you for helping me with fabrication, discussion of new ideas, support with experiments and any other questions.

Dr. Dominic Thurmer, thank you for constant technical support in the clean room and help in any technical or personal question.

Dr. Denys Makarov, thank you for helpful discussions, which helped me to understand better magnetization of thin films and for excellent support of magnetron sputtering to power my nanorockets.

Professor Dr. Guojiang Wang, thank you for interest in my work, great help in the lab, encouragements and many fruitful discussions.

Curriculum Vitae

Alexander A. Solovev

Physics Department, E-19a
Technical University of Munich
James-Franck-Str. 1
85748 Garching bei München
phone: ++ (49) 163 84 76 439
e-mail: alexander.solovev@ph.tum.de

Place of birth: *Maili-Sai, Kyrgyzstan*
Date of birth: *08.10.1981*
Languages: *English (fluent), German (intermediate), Russian (native)*

Current position: Wissenschaftlicher Mitarbeiter

Funded through BMBF Grant "Technologies for Sustainability and Climate Protection"

Education

PhD (at the same group) 07.2007 – 07.2011	Institute for Integrative Nanosciences, Leibniz institute of Solid State and Materials Research Dresden. Advisors: Dr. S. Sanchez, Prof. Dr. Y. F. Mei. Department: Prof. Dr. O. G. Schmidt
PhD 02.2007 – 06.2007	Max Planck Institute for Solid State Research Stuttgart. Advisors: Prof. Dr. Y. F. Mei, Prof. Dr. O. G. Schmidt. Department: Prof. Dr. K. von Klitzing (*Nobel Prize* in Physics 1985)
Master of Science 01.2006	Technical University of Munich, Walther Schottky Institute, Physics Department. Advisors: Prof. Dr. M. Tornow, Prof. Dr. G. Abstreiter
Exchange Student 2004	Princeton University, NJ, USA. Columbia Universtiy in the City of New York, USA. Advisors: Prof. Dr. J. Schwarz, Prof. Dr. G. Flynn
Diploma, Engineer 07.2003	Kyrgyz-Russian Slavic University, Physics and Engineering Departments. Advisors: Prof. Dr. O. N. Kanygina, Prof. Dr. J. I. Rudaev

Professional Career

Postdoc, Research Associate 08.2011 – now	Technical University of Munich, Physics Department, Non-Equilibrium Chemical Physics (former group of Prof. Dr. G. Ertl, *Nobel Prize* in Chemistry 2007)
PhD, Research Assistant 02.2007 – 07.2011	Institute for Integrative Nanosciences, Leibniz institute of Solid State and Materials Research Dresden. Max Planck Institute for Solid State Research Stuttgart
Research Assistant 05.2006 – 08.2006	Technical University of Munich, Walther Schottky Institute, Physics Department. Advisors: Prof. Dr. M. Tornow, Prof. Dr. G. Abstreiter

Awards & Honours

- Guinness World Record for the demonstration of "the Smallest Man-Made Jet Engine". Guinness Book Edition 2012, released in over 100 countries and in 25 languages (2011)
- Permanent Residency in Germany given for 'Hochqualifizierte' (2011)
- Invited Demonstration of best Nanotech Experiments chosen for Public. DECHEMA: Society of Chemistry & Biotechnology, Marburg, Germany (2010)
- "DSM Science and Technology Award", Honorable Mention, Zürich, Switzerland (2009)
- Exchange Student Grant to Princeton University, NJ, USA (2005)
- Exchange Student Grant to Columbia University in the City of New York, NY, USA (2004)
- I-st Place Award in Student's Olympiad in *Theoretical Mechanics* (Prize from Ministry of Science, Education and Culture) Kyrgyzstan (2001)
  III-rd Place Award in Student's Olympiad of Kyrgyzstan in *Resistance of Materials* (2001)
- III-rd Place Award in Student's Olympiad of Kyrgyzstan in *Theoretical Mechanics* (2000)

Teaching Experience

- Supervisor of Students Seminars "Self-Organization in Physical Science: Patterns, Chaos and Rhythms" TU München (2011-2012)
- Supervisor of Lab Experiments for Students (2009 - 2011, IFW Dresden)

Invited Talks

- Catalytic Nanojet Engines in Applications for Nanotechnology. Soft Matter Seminars. LMU München (11.2011)
- Self-Assembled Catalytic Microjet Engines. Vitzenau, Switzeland (06.2008)

Other Activities

- Demonstrations of microrockets experiments for: Long Nights of Science (IFW Dresden), World of Physics (in '*Kaufpark Dresden*'), educational films (*tv.orf.at*), popular newspapers ('*Bild Zeitung*') and magazines ('*Zeit Wissen*', '*PM*'), (2008–2011).

Selbstständigkeitserklärung

Hiermit erkläre ich an Eides statt, dass ich die am heutigen Tag eingereichte Dissertation zum Thema "Catalytic Tubular Micro-Jet Engines" unter der Betreuung von Herrn Prof. Dr. Oliver G. Schmidt selbständig erarbeitet, verfasst und Zitate kenntlich gemacht habe. Andere als die angegebenen Hilfsmittel wurden von mir nicht benutzt. Die Dissertation wurde in dieser oder ahnlicher Form an keiner anderen Stelle zum Zwecke eines Promotionsverfahrens eingereicht. Es wurde von mir bisher kein Promotionsverfahren an anderer Stelle beantragt.

Alexander Alexandrovich Solovev

München, den 26.03.2012